

**OPTICAL AND ELECTRONIC PROPERTIES
OF ATOMICALLY THIN LAYERED
MATERIALS: FIRST PRINCIPLES
CALCULATIONS**

**A Thesis Submitted to
the Graduate School of Engineering and Sciences of
İzmir Institute of Technology
in Partial Fulfillment of the Requirements for the Degree of**

DOCTOR OF PHILOSOPHY

in Physics

**by
Fadıl İYİKANAT**

**July 2019
İZMİR**

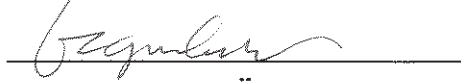
We approve the thesis of **Fadıl İYİKANAT**

Examining Committee Members:



Prof. Dr. R. Tuğrul SENER

Department of Physics, İzmir Institute of Technology



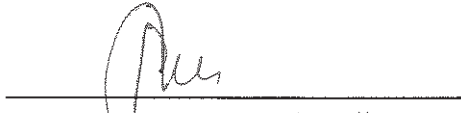
Assoc. Prof. Dr. Özgür ÇAKIR

Department of Physics, İzmir Institute of Technology



Asst. Prof. Dr. Emre SARI

Department of Photonics, İzmir Institute of Technology



Prof. Dr. Serpil ŞAKİROĞLU

Department of Physics, Dokuz Eylül University



Assoc. Prof. Dr. Engin DURGUN

Department of Materials Science and Nanotechnology, Bilkent University



Prof. Dr. R. Tuğrul SENER

Supervisor, Department of Physics
İzmir Institute of Technology

12 July 2019



Assoc. Prof. Dr. Hasan ŞAHİN

Co-Supervisor, Department of Photonics
İzmir Institute of Technology



Prof. Dr. Lütfi ÖZYÜZER

Head of the Department of
Physics



Prof. Dr. Aysun SOFUOĞLU

Dean of the Graduate School of
Engineering and Sciences

ACKNOWLEDGMENTS

It is my pleasure to express my gratitude to those who helped me along the way to complete of this thesis.

I wish to express my respect and sincere gratitude to my supervisor Prof. Dr. R. Tuğrul Senger and co-supervisor Assoc. Prof. Dr. Hasan Şahin for their supervision, care and support during this thesis and also for giving me the opportunity to work in a very interesting field of research. Without their encouragement, guidance and insight, I could not have finished this dissertation.

I would like to thank TUBITAK for financial support (114F397) during this thesis. The numerical calculations reported in this thesis were partially performed at TUBITAK ULAKBIM, High Performance and Grid Computing Center (TRUBA resources).

I would like to appreciate deeply to my colleagues Mehmet Yağmırcukardeş, Cihan Bacaksız, and H. Duygu Özyaydin for their all kind of supports and warm friendship. Thanks to each of my friends at İzmir Institute of Technology for providing a great atmosphere and a wonderful workplace.

Personally, my special thanks go to my family for their unconditional supports and their belief in me.

This thesis is dedicated to my beautiful wife Elif. There is no way to thank her for the love she has given me all these years.

ABSTRACT

OPTICAL AND ELECTRONIC PROPERTIES OF ATOMICALLY THIN LAYERED MATERIALS: FIRST PRINCIPLES CALCULATIONS

The extraordinary interest in two-dimensional (2D) materials is increasing day by day. Thanks to advances in the experimental techniques, monolayer form of another material is synthesized every day with features not seen in the bulk form. *Ab initio* methods provide useful tools for characterizing and functionalizing the various properties of these materials. The results obtained through first principles quantum-mechanical calculations can help to predict and understand the experimental data, such as the position and source of the spectroscopic peaks in the Raman or optical absorption spectra.

The aim of this thesis is to predict and functionalize the optical and electronic properties of atomically thin layered materials using density functional theory and approaches beyond. Within the scope of this thesis, possible technological applications of various 2D materials ranging from perovskite crystals to transition metal dichalcogenides are investigated by using several functionalization methods. In order to accurately predict the optical properties of these materials, it is very important to use approaches that take into account the many-body effects. Recent studies have shown that many-body perturbation theory in the form of GW approximation is highly reliable to calculate the quasiparticle properties of materials. By solving the Bethe Salpeter equation on top of GW calculation, the quasiparticle energies and excitonic properties, which have dominant effect in the optical properties of ultra-thin materials are examined in detail.

ÖZET

ATOM İNCELİĞİNDEKİ TABAKALI MALZEMELERİN OPTİK ve ELEKTRONİK ÖZELLİKLERİ: İLK PRENSİP HESAPLAMALARI

İki boyutlu (2B) malzemelere olan olağanüstü ilgi gün geçtikçe artmaktadır. Deneysel tekniklerdeki gelişmeler sayesinde, her gün yeni bir malzemenin tek tabaka formu yığın formunda görülmeyen yeni özellikler ile sentezlenmektedir. *İlk prensip* yöntemleri, bu malzemelerin çeşitli özelliklerini karakterize etmek ve işlevselleştirmek için kullanışlı araçlar sağlamaktadır. *İlk prensip* kuantum-mekanik hesaplamaları ile elde edilen sonuçlar Raman veya optik soğurma spektrumlarındaki pik pozisyonları ve bunların kaynağı gibi deneysel verilerin tahmin edilmesine ve anlaşılmasına yardımcı olabilir.

Bu tezin amacı atom inceliğindeki tabakalı malzemelerin optik ve elektronik özelliklerinin yoğunluk fonksiyoneli teorisi ve ötesi yaklaşımlar kullanılarak tahmin edilmesi ve işlevselleştirilmesidir. Bu tez kapsamında, perovskit kristallerden geçiş metali dikalkojenitlerine kadar çeşitli 2B malzemelerin olası teknolojik uygulamaları bir kaç farklı işlevlendirme yöntemi ile incelendi. Bu malzemelerin optik özelliklerinin hassas bir şekilde tahmin edilebilmesi için çok-parçacık etkilerini dikkate alan yaklaşımların kullanılması çok önemlidir. Son çalışmalar göstermiştir ki, GW yaklaşımı formundaki çok-parçacık pertürbasyon teorisi malzemelerin sözde-parçacık özelliklerini hesaplamada oldukça güvenilirdir. Oldukça ince malzemelerin optik özelliklerinde dominant etkilere sahip olan sözde-parçacık enerjileri ve eksitonik özellikler, GW hesabının üzerine Bethe Salpeter denklemi çözülerek detaylıca incelendi.

TABLE OF CONTENTS

LIST OF FIGURES	ix
LIST OF TABLES	xiv
CHAPTER 1. INTRODUCTION	1
CHAPTER 2. THEORETICAL BACKGROUND AND COMPUTATIONAL METHODOLOGY	3
2.1. Electronic Structure	3
2.1.1. Density Functional Theory	6
2.1.2. Hohenberg-Kohn Theorems	6
2.1.3. The Kohn-Sham Equations	7
2.1.4. Approximations to the Exchange-Correlation Potential	9
2.2. Light-Matter Interaction	11
2.2.1. Electromagnetic Fields in a Material	11
2.2.2. The Complex Refractive Index and Dielectric Constant	16
2.2.3. Interband Absorption.....	20
2.2.4. Quasiparticle Energies	23
2.2.5. Excitonic Effect and the Bethe-Salpeter Equation.....	24
2.3. Computational Methodology	25
CHAPTER 3. ELECTRONIC PROPERTIES OF ATOMICALLY THIN LAYERED MATERIALS	27
3.1. Vacancy Defect and Foreign Atom Adsorption	28
3.1.1. Vacancy Formation and Oxidation Characteristics of Single Layer TiS_3	28
3.1.1.1. Single Layer TiS_3	29
3.1.1.2. Defective Single Layer TiS_3	32
3.1.1.3. Oxidation of Pristine and Defective Single Layer TiS_3 ...	36
3.1.1.4. Conclusions	39
3.1.2. Hydrogenation of Single-layer TiSe_2	40
3.1.2.1. Pristine TiSe_2	41

3.1.2.2.	Interaction with a Single H atom.....	45
3.1.2.3.	Full Hydrogenation	47
3.1.2.4.	Conclusions	52
3.2.	Thinning of Two-Dimensional Materials	52
3.2.1.	Thinning CsPb ₂ Br ₅ Perovskite Down to Monolayers	52
3.2.1.1.	Bulk CsPb ₂ Br ₅	54
3.2.1.2.	Thinning CsPb ₂ Br ₅ down to Monolayers.....	57
3.2.1.3.	Effect of Cs Atoms via The Charging of Pb ₂ Br ₅ Skeleton	61
3.2.1.4.	Vacancy Defects in Single-Layer CsPb ₂ Br ₅	62
3.2.1.5.	Conclusions	65
3.2.2.	Structural and Electronic Properties of PtSe ₂ : from Mono- layer to Bulk	65
3.2.2.1.	Monolayer PtSe ₂	66
3.2.2.2.	Dimensional Crossover From Monolayer to Bulk	69
3.2.2.3.	Conclusions	74
3.3.	Effect of in-plane strain	75
3.3.1.	Tuning Electronic and Magnetic Properties of Monolayer α - RuCl ₃ by In-plane Strain	75
3.3.1.1.	Electronic and Magnetic Properties.....	76
3.3.1.2.	Vibrational Properties	80
3.3.1.3.	Strain Application	82
3.3.1.4.	Conclusions	84
3.3.2.	Stable Ultra-thin CdTe Crystal: A Robust Direct Gap Semi- conductor	85
3.3.2.1.	Structural and Electronic Properties	86
3.3.2.2.	Dynamical Stability.....	90
3.3.2.3.	Strain Response of Single-Layer CdTe	92
3.3.2.4.	Conclusions	96

CHAPTER 4.	OPTICAL PROPERTIES OF ATOMICALLY THIN LAYERED MATERIALS	98
4.1.	DFT-based Optical Calculations	98
4.1.1.	Layer-dependent Optical Properties of Orthorhombic CsPbI ₃ Perovskites	98
4.1.1.1.	Possible Structures of Ultra-thin Orthorhombic CsPbI ₃ ..	99

4.1.1.2.	Electronic and Optical Properties of Ultra-thin CsPbI ₃ ...	103
4.1.1.3.	Conclusions	105
4.2.	Quasiparticle and Excitonic Effects in Optical Properties.....	105
4.2.1.	Excitonic Properties in Bilayer Blue Phosphorene	106
4.2.1.1.	Computational Methodology	107
4.2.1.2.	Structural and Electronic Properties of Monolayer and Bilayer Blue Phosphorene	108
4.2.1.3.	Excitonic Properties of Monolayer and Bilayer Blue Phosphorene	111
4.2.1.4.	Conclusions	117
CHAPTER 5. CONCLUSIONS		119
REFERENCES		122

LIST OF FIGURES

<u>Figure</u>	<u>Page</u>
Figure 2.1. The reflection and transmission of light at an interface between air and a medium of refractive index \tilde{n}	14
Figure 3.1. (a) Top view of monolayer TiS_3 and its unit cell shown by a rectangle. For a better top view, S atoms in different layers are presented by different colors. (b) Tilted side view of $2 \times 2 \times 1$ supercell of monolayer TiS_3 . (c) Blue dashed lines and red lines illustrate PBE + vdW and PBE + vdW + HSE06 results for the electronic band diagram of monolayer TiS_3 , respectively. (d) Band decomposed charge densities of valance band (VB) and conductance band (CB) at Γ and B.	30
Figure 3.2. Cross-sectional plane view of the charge densities, with two surface, and one inner S atom placed at this plane. Valance charges on inner and outer S atoms are also shown. Color code of atoms is the same as in Figure3.1. Electron density increases from green to red.	32
Figure 3.3. Top view of relaxed monolayer TiS_3 with (a) S-vacancy, (b) Ti-vacancy, (c) Double S-vacancy, (d) TiS-vacancy. Black atoms illustrate removed atoms, dashed circles show initial position of the displaced atom. Color code of the other atoms is the same as in Figure 3.1. The direction of displaced atoms are depicted by blue arrows.	34
Figure 3.4. Density of states of (a) pristine TiS_3 , with (b) S-vacancy, (c) Ti-vacancy, (d) Double S-vacancy, and (e) TiS-vacancy.	35
Figure 3.5. Tilted side view of (a) O, (c) O_2 and (e) O_3 adsorbed on pristine TiS_3 . (b) O, (d) O_2 and (f) O_3 adsorbed on an S-vacant TiS_3	37
Figure 3.6. (a) Top view of CDW phase of single-layer TiSe_2 . Black lattice in the background illustrates the 1T phase of TiSe_2 . Light blue and green balls illustrate Ti and Se atoms, respectively. Dark blue and orange vectors show proportional magnitudes and directions of the relevant atomic displacements. Phonon band diagrams and partial phonon DOS of (b) 1T phase (Inset: Top view of atomic displacements of the corresponding mode) and (c) CDW phase of single-layer TiSe_2	42
Figure 3.7. (a) The energy-band structure of CDW phase of TiSe_2 . Light blue and red-dotted bands are for GGA and GGA+HSE, respectively. (b) GGA+HSE calculated partial density of states of CDW phase of TiSe_2 . .	44

Figure 3.8. (a) Top view of six inequivalent adsorption configurations for a H atom on CDW phase of TiSe ₂ . (b) Top and side views of fully relaxed geometric structure of single H atom adsorbed CDW phase of TiSe ₂ . (c) The electronic band structure and PDOS of single H atom adsorbed CDW phase of TiSe ₂ . Light blue and red-dotted bands are for GGA and GGA+HSE, respectively.	46
Figure 3.9. (a) Top and (b) side view geometries and (c) phonon band diagram and partial phonon DOS of fH-TiSe ₂ . The branches of the possible Raman-active modes are shown on the lower panel.	48
Figure 3.10. Constant-volume heat capacity of single-layer crystal structures of 1T and CDW phases of pristine TiSe ₂ and fH-TiSe ₂	50
Figure 3.11. (a) The electronic band structure of fH-TiSe ₂ . Light blue and red-dotted bands are for GGA and GGA+HSE calculated band dispersions, respectively. (Inset: GGA calculated band dispersion near the fermi level.) (b) GGA+HSE calculated PDOS of fH-TiSe ₂ . The valence band maximum is set to zero.	51
Figure 3.12. (a) Tilted side view of bulk CsPb ₂ Br ₅ . (b) Tilted side and top views of Pb-Br polyhedron layer. (c) Tilted side and top views of Pb-Br polyhedron. Green, brown, and gray balls illustrate Cs, Br, and Pb atoms, respectively.	55
Figure 3.13. (a) The energy-band dispersion and (b) partial density of states of bulk CsPb ₂ Br ₅ . (c) The band decomposed charge densities of the bulk CsPb ₂ Br ₅ at the labeled band edges. Isosurface value of charge density is $2 \times 10^{-5} e/\text{\AA}^3$	56
Figure 3.14. Possible single-layer structures of CsPb ₂ Br ₅ crystal. Top and side views of the structures, phonon spectrum, and SOC included electronic band diagrams of single-layer (a) Pb ₂ Br ₅ , (Inset: Tilted side view of atomic displacements of the corresponding mode.) (b) CsPb ₄ Br ₁₀ , (c) <i>ss</i> -CsPb ₂ Br ₅ , (d) <i>ds</i> -CsPb ₂ Br ₅ , and (e) Cs ₂ Pb ₂ Br ₅ . Isosurface value of band decomposed charge densities (inset of band structure of <i>ss</i> -CsPb ₂ Br ₅) is $2 \times 10^{-5} e/\text{\AA}^3$	59
Figure 3.15. Charging-dependent phonon dispersion of single layer skeleton structure of Pb ₂ Br ₅	62

Figure 3.16. Top view of the structures, band decomposed charge densities of the VBM and CBM, and electronic band structures of single-layer ds -CsPb ₂ Br ₅ with (a) Cs vacancy, (b) Br _{<i>i</i>} vacancy, (c) Br _{<i>s</i>} vacancy, and (d) Pb vacancy. Pink atoms illustrate removed atoms. Yellow, red, and dashed blue lines in band diagrams illustrate the Fermi level, majority, and minority spin bands, respectively. Band decomposed charge densities of in-gap states of V_{Br_i} and V_{Br_s} are shown in the insets of the corresponding band diagrams. Isosurface value of charge density is $6 \times 10^{-6} e/\text{\AA}^3$	63
Figure 3.17. (a) Top and side views of geometric structures of 1T-PtSe ₂ monolayer. Gray and green atoms show Pt and Se atoms, respectively. (b) The phonon band diagram and (c) normalized Raman intensity of 1T-PtSe ₂ monolayer. (d) The electronic band diagram and (e) partial density of states of the monolayer structure. The Fermi level is set to zero.	67
Figure 3.18. The SOC included electronic band diagrams of 1T-PtSe ₂ monolayer as a function of tensile biaxial strain. The Fermi level is set to zero. Side views show the valence band maximum (VBM) and conduction band minimum (CBM) on an enlarged scale.	70
Figure 3.19. Top and side views of crystal structure of bilayer 1T-PtSe ₂ ; (a) AA, (b) AB (c) A'A, and (d) A'B stacking orders. The ground-state energy differences are given under each stacking type labeled with ΔE	71
Figure 3.20. The electronic band dispersions of monolayer, bilayer, trilayer, bulk 1T-PtSe ₂ . The Fermi level is set to zero.	72
Figure 3.21. The phonon band dispersions of (a) bilayer, (b) trilayer, (c) four-layer and (d) bulk. The S and LB mode frequencies are indicated. (e) Layer dependent Raman intensity of E _{<i>g</i>} mode. (f) Frequency shifts of the E _{<i>g</i>} and A _{<i>g</i>} modes with respect to number of layers. 1L, 2L, 3L and 4L denote monolayer, bilayer, trilayer and four-layer, respectively.	73
Figure 3.22. (a) Top and side views of the geometric structure of monolayer α -RuCl ₃ . Blue and yellow atoms show Ru and Cl, respectively. Ru-Ru distances are shown by d_1 and d_2 . Top and side views of the spin density plot of (b) FM, (c) AFM, (d) ZZ-AFM, and (e) stripy configurations (keeping the same isosurface value of $0.01 e/\text{\AA}^3$ for each of the plots). Red and green isosurfaces represent majority and minority spin densities.	77

Figure 3.23. The variations of MAE values are projected on the sphere for (a) ZZ-AFM and (b) FM configurations.	79
Figure 3.24. (a) Calculated band dispersions within GGA and GGA+SOC, and partial density of states (PDOS) of ZZ-AFM state of single-layer α -RuCl ₃ . (b) Calculated band dispersion within GGA, and partial density of states (PDOS) of FM state of single-layer α -RuCl ₃ . Spin-up (\uparrow) and spin-down (\downarrow) bands are shown by green and black lines, respectively. The Fermi energy (E_F) level is set to the valence band maximum.	80
Figure 3.25. Phonon-band structure and corresponding Raman activities of monolayer α -RuCl ₃ for; (a) FM and (b) ZZ-AFM configurations. Vibrational motion of individual atoms in some prominent Raman active modes are also shown on the right panel.	81
Figure 3.26. The variations of the total energy differences and ground state electronic band dispersions of ZZ-AFM and FM phases as a function of in-plane strain along (a) zigzag (ϵ_{zig}) and (b) armchair (ϵ_{arm}) directions. Blue and red shaded regions delineate the FM and ZZ-AFM regions, respectively.	83
Figure 3.27. Side views (a) along \vec{a} lattice vector, (b) along \vec{b} lattice vector and (c) top view of single-layer CdTe. Black lines represent the rectangular unit cell. (d) The charge densities of the isolated Cd and Te atoms are subtracted from the charge density of single-layer CdTe. The yellow and blue densities stand for the negative and positive charges, respectively. Red and blue atoms are for Cd and Te, respectively.	87
Figure 3.28. (a) Electronic band structure and (b) atom- and orbital-decomposed electronic density of states of single-layer CdTe. Fermi level is set to zero. (c) and (d) 2D surface plots of the valence band and the conduction band edges in the reciprocal space, respectively. The energy values (eV) are color coded below the plots.	89
Figure 3.29. The phonon spectrum of monolayer CdTe is shown on the left. The branches of the possible Raman-active modes are indicated by the red dots and the corresponding normal modes are shown on the right.	91
Figure 3.30. Evolution of the band dispersion of single-layer CdTe as a function of in-plane strain along armchair (ϵ_{arm}) and zigzag (ϵ_{zig}) directions. Fermi level is set to zero.	93

Figure 3.31. Evolution of the band dispersion of single-layer CdTe as a function of compressive strain along out-of-plane (ε_v) direction. Fermi level is set to zero.	94
Figure 3.32. Evolution of band gaps of single-layer CdTe under in-plane and out-of-plane strain. Dots are calculated values and lines are fitted values.	95
Figure 4.1. (a) Bulk, (b) bilayer, and (c) monolayer structures of CsPbI ₃ crystal.	100
Figure 4.2. Phonon band diagram of (a) bulk CsPbI ₃ crystal in orthorhombic phase, (b) Cs ₃ Pb ₂ I ₇ and Cs ₂ Pb ₃ I ₈ bilayers, (c) Cs ₂ PbI ₅ , CsPbI ₄ , and Cs ₂ PbI ₄ monolayers.	102
Figure 4.3. Electronic band dispersions of (a) bulk, (b) bilayer, and (c) monolayer structures of orthorhombic CsPbI ₃ crystal. The layer dependent optical properties of CsPbI ₃ . (a) Imaginary part of dielectric function, (b) absorption coefficient, (c) reflectivity, and (d) transmissivity of bulk, bilayer, and monolayer CsPbI ₃	104
Figure 4.4. (a) Top and side views of optimized geometric structures and (b) the orbital-projected electronic band dispersions of monolayer blue phosphorene. Light and dark blue atoms show the upper and lower P atoms in the layer, respectively.	109
Figure 4.5. Top and side views of optimized geometric structures and the orbital projected electronic band dispersions of (a) AA _L , (b) AA _H , (c) AB _L , and (d) AB _H stacked bilayer blue phosphorene. Light and dark blue atoms show the upper and lower P atoms in each layer, respectively.	111
Figure 4.6. (a) Electronic band structures within G ₀ W ₀ , (b) imaginary part of dielectric function and oscillator strengths of monolayer blue phosphorene. The insets show the real space exciton wave functions.	113
Figure 4.7. Electronic band dispersions within G ₀ W ₀ (the left panels), imaginary part of dielectric functions, oscillator strengths, and top views of the real space exciton wave functions (the middle panels), the percentage of the excitonic wave function on each layer (the right panels) of (a) AA _L , (b) AA _H , (c) AB _L , and (d) AB _H stacked bilayer blue phosphorene. In all cases, the hole position is indicated by the black arrow.	116

LIST OF TABLES

<u>Table</u>	<u>Page</u>
Table 3.1. Lattice parameters, formation energies, magnetic moments, and electronic characteristics of 3×3 supercell of monolayer TiS_3 and its few defected forms.	33
Table 3.2. The lattice constants, a and b ; the distance from adsorbed H atom to the TiSe_2 surface, $d_{\text{Se-H}}$; binding energy, E_b ; HSE calculated electronic band gap, E_g ; of CDW phase, single-H adsorbed and fully-hydrogenated TiSe_2 (fH- TiSe_2).	47
Table 3.3. The calculated ground state properties for bulk (<i>b</i>) CsPb_2Br_5 and single-layer Pb_2Br_5 , $\text{CsPb}_4\text{Br}_{10}$, <i>ss</i> - CsPb_2Br_5 , <i>ds</i> - CsPb_2Br_5 , and $\text{Cs}_2\text{Pb}_2\text{Br}_5$: The lattice constants in the lateral and vertical directions, a and c , respectively; thickness of the Pb-Br polyhedron layer, h ; atomic distances between Pb and Br atoms, $d_{\text{Pb-Br}}^i$ and $d_{\text{Pb-Br}}^s$; atomic distance between Cs and surface Br atoms, $d_{\text{Cs-Br}}^s$; the cohesive energies, E_{coh} ; the energy band gap of the structure, Gap ; the work function, Φ	58
Table 3.4. The lattice constants, a ; formation energies, E_{form} ; magnetic moments, M ; electronic characteristics, and band gaps of four different defected forms of $2 \times 2 \times 1$ supercell of the single-layer CsPb_2Br_5	64
Table 3.5. The calculated parameters for the 1T- PtSe_2 structures are; the lattice constants, $a=b$; overall thickness as the uppermost-lowermost Se-Se distance in the unitcell, h ; the charge donation from Pt to Se atoms, $\Delta\rho$; the cohesive energy per atom, E_{Coh} ; Φ and μ are the values of work function and magnetization, respectively; E_{gap} , the energy band gap of the structure.	68
Table 3.6. Calculated conventional cell lattice parameters a and b , Ru-Ru distances d_1 and d_2 (they are shown in Figure 3.22 (a)), Bader charge transferred between Ru and Cl atoms ρ , absolute magnetic moment per Ru atom μ (Bohr magneton), magnetic anisotropy energy per Ru atom (MAE), and the energy band gap E_g	78
Table 3.7. The calculated ground state properties for bulk and single-layer (SL) CdTe : The lattice constants, a and b ; atomic distance between Cd and Te atoms, $d_{\text{Cd-Te}}$; charge transfer from Cd to Te atom, $\Delta\rho$; the cohesive energy per atom, E_c ; energy band gap, E_{gap} ; and ionization energy, I . E. .	88

Table 3.8.	Effective masses of electrons (m_e) and holes (m_h) of bulk and single-layer (SL) CdTe.	90
Table 4.1.	The calculated parameters for the unitcells of the bulk, bilayer and monolayer CsPbI ₃ ; the lattice constants, a , b and c ; layer thickness, h ; the cohesive energy per atom, E_{Coh} ; the band gap of structures with LDA and PBE0, E_{gap} and E_{gap}^{PBE0} , respectively ; the work function, Φ	101
Table 4.2.	Calculated parameters for the monolayer and four different stacking configurations of bilayer blue phosphorene; the lattice constant, a ; P-P distance, d ; buckling height, h_b ; interlayer distance, h_i ; the cohesive energy per atom, E_{Coh} ; energy band gap values within GGA and GGA+G ₀ W ₀ , E_g^{GGA} and $E_g^{G_0W_0}$, respectively.	110

CHAPTER 1

INTRODUCTION

Advances in experimental techniques have made nanotechnology a part of our lives. In order to make our mobile phones, computers and other electronic devices smaller, faster and more useful, the circuit elements are further reduced each year. But the transistors that make up the today's most advanced electronic devices are now on the atomic scale. Therefore, we have to use different methods to improve our existing nanoelectronic device architecture. It is clear that increasing the functionality of existing nanoelectronic devices is the most important way to advance nanotechnology.

The successful isolation of graphene single layers from graphite has aroused significant research interest in the field of condensed matter physics (Novoselov *et al.*, 2004). It has been shown that single layer graphene exhibits unique properties, such as high conductivity (Geim and Novoselov, 2010), high elasticity and mechanical strength (Lee *et al.*, 2008), and large surface area. Extraordinary interest in 2D materials triggered by graphene synthesis has led to the discovery of various ultra-thin materials, namely hexagonal boron nitride (Kim *et al.*, 2011), silicene (Vogt *et al.*, 2012), antimonene (Zhang *et al.*, 2015), transition metal dichalcogenides (TMDs) (Mak *et al.*, 2010; Coleman *et al.*, 2011; Sahin *et al.*, 2013), transition metal trichalcogenides (TMTs) (Ferrer *et al.*, 2013; Pant *et al.*, 2016), black phosphorene (Liu *et al.*, 2014), and MXenes (Gogotsi, 2015; Khazaei *et al.*, 2014). The synthesis of each new ultra-thin material provides a new environment in which nano-scale quantum effects can be directly tested and monitored.

Various engineering approaches have been used to improve and tailor the performance of 2D materials. It is known that the metallic structure of the graphene prevents the efficient use of this material in electronic devices. However, opening of the band gap of graphene has been achieved experimentally by functionalization of its surface with foreign atoms, and increased the application areas in various fields. For instance, fluorinated graphene has crucial properties such as thermal stability, very high mechanical strength and high electronic band gap (Nair *et al.*, 2010; Robinson *et al.*, 2010). It was shown that TMDs exhibit indirect to direct band gap transition (Mak *et al.*, 2010), and high exciton binding energies (Ugeda *et al.*, 2014), when the number of layers decreased to the monolayer limit. Strain-dependent variation of the electronic band gap and a significant strain-induced reduction in the photoluminescence intensity of the monolayer MoS₂

have been reported earlier (Conley *et al.*, 2013). Moreover, the inherent structure of 2D materials allows the layer by layer stacking of them in any order to create new materials with completely different properties from the properties of building blocks. Based on the graphene-MoS₂ heterostructures, phototransistors with highly sensitive photodetection and gate-tunable persistent photoconductivity were already fabricated (Roy *et al.*, 2013). It was found that heterostructures can host interlayer excitons where the electron and hole reside in distinct layers (Rivera *et al.*, 2015; Yu *et al.*, 2014). Due to the reduced overlap of the electron and hole wave functions, interlayer excitons typically have long lifetimes (Palummo *et al.*, 2015).

Experimental investigation of these novel nanoscale materials requires quite expensive devices and long experimental works. Moreover, it is very important to understand the experimentally observed features at the atomistic level for the development of nanotechnology applications. Computational condensed matter physics aims to reveal the fundamental laws of nature at the nanoscale. However, the excessive number of particles and complexity of interactions between these particles complicate a comprehensive description of real-world systems. Fortunately, density functional theory (DFT) and related techniques enabled the theoretical investigation of the ground state properties of realistic novel materials. However, the DFT is not adequate to calculate the excited state properties of materials. In order to calculate the electronic excitations observed in the photoemission experiment, beyond DFT approaches such as the GW approximation and Bethe Salpeter Equation (BSE) are required.

The rest of the thesis is structured as follows. Chapter 2 is devoted to the theoretical background of the DFT, GW approximation and BSE method. In Chapter 3, we focus on the structural and electronic properties of various new atomically thin systems and their response under a variety of functionalization methods. In Chapter 4, the optical properties of materials with various thicknesses ranging from bulk to single layer are investigated by DFT and beyond DFT approaches. Chapter 5 is devoted to summarize the results of our studies.

CHAPTER 2

THEORETICAL BACKGROUND AND COMPUTATIONAL METHODOLOGY

The main goal of the computational condensed matter physics is to describe and predict the structural, electronic, magnetic and optical properties of interacting many-body systems. Excess number of particles that make up the real systems and the complexity of the interaction between these particles make the comprehensive understanding of such a system extremely challenging and computationally expensive. Fortunately, the theoretical approaches that reduce the computational burden, improvements in theory and computing power have made it possible to predict the various features of materials in a way that is consistent with the experimental results. The most commonly used and most successful theory to determine the ground state properties of materials is the Density Functional Theory (DFT). The reasons of its popularity and success are high computational efficiency and its accuracy. Moreover, DFT is a *ab initio* theory, so DFT calculations do not require any empirical parameters. However, DFT is not suitable for describing electronic excitations probed by optical absorption experiments. In order to calculate electronic excitations of materials, beyond DFT approaches such as many-body perturbation theory (MBPT) should be used.

2.1. Electronic Structure

Since the laws of quantum mechanics are valid at the nanoscale instead of the laws of classical mechanics, the Schrödinger equation must be solved in order to determine the physical and chemical properties of the nanoscale materials;

$$\hat{H}\psi_i(\mathbf{r}, \mathbf{R}) = E_i\psi_i(\mathbf{r}, \mathbf{R}), \quad (2.1)$$

where E_i is the energy eigenvalue and $\psi_i(\mathbf{r}, \mathbf{R})$ denotes the wave function. The Hamiltonian operator (\hat{H}) of a many-body system consisting of electrons and nuclei is given in

the following formula;

$$\hat{H} = -\hbar^2 \sum_I \frac{\nabla_{\mathbf{I}}^2}{2M_I} - \hbar^2 \sum_i \frac{\nabla_{\mathbf{i}}^2}{2m_i} - \sum_{i,I} \frac{Z_I e^2}{|\mathbf{r}_i - \mathbf{R}_I|} + \frac{1}{2} \sum_{i \neq j} \frac{e^2}{|\mathbf{r}_i - \mathbf{r}_j|} + \frac{1}{2} \sum_{I \neq J} \frac{Z_I Z_J e^2}{|\mathbf{R}_I - \mathbf{R}_J|} \quad (2.2)$$

where Z_I denotes the atomic number of the nucleus. Upper and lower case subscripts show nuclei and electrons, respectively. The first and second terms in the Hamiltonian are the kinetic energy of the nuclei and electrons, respectively. The third, fourth and last terms are the potential energy of nucleus-nucleus, electron-electron, and nucleus-electron Coulomb interactions, respectively. Unfortunately the exact solution to this problem is almost impossible for real-world systems. Some approximations have been made to overcome this challenge.

The first approximation is the Born-Oppenheimer approximation. Since the nuclei are much heavier than the electrons, the electrons move much faster than the nuclei. Therefore, the last term changes to a constant and the first term becomes negligible compared to other terms in the Hamiltonian. The resulting Hamiltonian consists of the kinetic energy of the electrons (\hat{T}), the potential energy of the electrons in the (external) potential of the nuclei (\hat{V}_{ext}), and the potential energy due to electron-electron interactions (\hat{V}):

$$\hat{H} = \hat{T} + \hat{V}_{ext} + \hat{V}. \quad (2.3)$$

Many-body electronic Schrödinger equation is still a very difficult problem to handle and exact solution is only known for some simple cases. A lot of approximations have been improved for handle the solution. Firstly in 1920 Douglas Hartree developed an approach named after himself called the Hartree approximation (Hartree, 1928). In this approximation the potential corresponding to electron-electron interactions could be

$$V(\mathbf{r}) = \int d\mathbf{r}' \frac{e^2 n(\mathbf{r}')}{|\mathbf{r} - \mathbf{r}'|} \quad (2.4)$$

where n is number density of electrons

$$n(\mathbf{r}) = \sum_j |\psi_j(\mathbf{r})|^2. \quad (2.5)$$

Then substitution the above potential to the Schrödinger equation we obtain the Hartree equation

$$E_l \psi_l(\mathbf{r}) = [\mathbf{T}_{\text{elec}} + \mathbf{V}_{\text{ion}}(\mathbf{r}) + \mathbf{V}(\mathbf{r})] \psi_l(\mathbf{r}). \quad (2.6)$$

In fact, Hartree approximation is wrong. It does not recognize the Pauli principle. According to Pauli exclusion principle, two electrons, cannot occupy the state all of their quantum numbers are the same. The true many-body wave function must vanish whenever two electrons occupy the same position, but the Hartree wave function cannot have this property. If we want to hold Pauli exclusion principle total electron wave function should be in an antisymmetric form:

$$\Psi = \frac{1}{\sqrt{N!}} \begin{vmatrix} \psi_1(\mathbf{r}_1, \sigma_1) & \psi_1(\mathbf{r}_2, \sigma_2) & \dots & \psi_1(\mathbf{r}_N, \sigma_N) \\ \psi_2(\mathbf{r}_1, \sigma_1) & \psi_2(\mathbf{r}_2, \sigma_2) & \dots & \psi_2(\mathbf{r}_N, \sigma_N) \\ \psi_3(\mathbf{r}_1, \sigma_1) & \psi_3(\mathbf{r}_2, \sigma_2) & \dots & \psi_3(\mathbf{r}_N, \sigma_N) \\ \cdot & \cdot & \dots & \cdot \\ \cdot & \cdot & \dots & \cdot \\ \psi_N(\mathbf{r}_1, \sigma_1) & \psi_N(\mathbf{r}_2, \sigma_2) & \dots & \psi_N(\mathbf{r}_N, \sigma_N) \end{vmatrix}$$

which is known as a Slater determinant (Slater, 1929). Where $\psi_i(\mathbf{r}_j, \sigma_j)$ is the single-electron spin orbital, and it is the product of position $\phi_i(\mathbf{r}_i)$ and spin $\alpha_i(\sigma_i)$ components. This approximation is called as a Hartree-Fock (HF) (Fock, 1930).

The Slater determinant above is helpful in obtaining the exchange term. Applying exchange term to the Hartree equation leads to the Hartree-Fock equation:

$$E_l \psi_l(\mathbf{r}) = [\mathbf{T}_{\text{elec}} + \mathbf{V}_{\text{ion}}(\mathbf{r}) + \mathbf{V}(\mathbf{r})] \psi_l(\mathbf{r}) - \frac{1}{2} \sum_j \int \mathbf{d}^3 \mathbf{r}' \psi_j^*(\mathbf{r}') \psi_i(\mathbf{r}') \frac{1}{|\mathbf{r} - \mathbf{r}'|} \psi_j(\mathbf{r}) \quad (2.7)$$

The Hartree-Fock equations deal with exchange exactly; however, the equations neglect more detailed correlations due to many-body interactions. The effects of electronic correlations are not negligible. This is first failure of HF approximation. On the other hand, since wave-function methods in general limited to molecules with a small number of active electrons, this approximation is not useful for many-body structures.

In the 1920's Thomas-Fermi developed another approach to this electronic problem. They purposed that, the full electronic density was the fundamental variable of the many-body problem, and derived a differential equation for the density without resorting to one-electron orbitals. But Thomas-Fermi approximation did not include exchange and correlation effects. Both Thomas and Fermi neglected exchange and correlation among

the electrons; however, this was extended by Dirac in 1930 (Dirac, 1930), who formulated the local approximation for exchange still in use today. This leads to the energy functional for electrons in an external potential $V_{ext}(\mathbf{r})$

$$E_{TF}[n] = C_1 \int d^3r n(\mathbf{r})^{\frac{5}{3}} + \int d^3r V_{ext}(\mathbf{r})n(\mathbf{r}) + C_2 \int d^3r n(\mathbf{r})^{\frac{4}{3}} + \frac{1}{2} \int d^3r d^3r' \frac{n(\mathbf{r})n(\mathbf{r}')}{|\mathbf{r} - \mathbf{r}'|}, \quad (2.8)$$

in here the first term is the local approximation to the kinetic energy, the third term is the local exchange and the last term is the classical electrostatic Hartree energy.

However, the Thomas-Fermi approximation is too crude, missing essential physics and chemistry, such as shell structures of atoms and binding of molecules. Although their approximation is not accurate enough for present-day electronic structure calculations, the approach illustrates the way density functional theory works.

2.1.1. Density Functional Theory

Density functional theory (DFT) is one of the most widely used method for electronic structure calculations in condensed matter physics. The reasons of its popularity and success are high computational efficiency and its accuracy. The general idea of DFT is that any property of system which has many interacting particles can be viewed as a functional of the ground state electron density $n_0(\mathbf{r})$ (Kohn and Sham, 1965; Hohenberg and Kohn, 1964). Although DFT is a very powerful tool for determining the structural and electronic properties of materials, it underestimates the band gaps of semiconductors and some other electronic properties of highly correlated systems. DFT is based on the famous theorem by Hohenberg and Kohn (Hohenberg and Kohn, 1964).

2.1.2. Hohenberg-Kohn Theorems

DFT is based upon two theorems formulated by Hohenberg and Kohn.

- **Theorem 1:** There is a one-to-one correspondence between the ground-state density $n_0(\mathbf{r})$ of a many-electron system and the external potential $V_{ext}(\mathbf{r})$.

Thus since the density $n_0(\mathbf{r})$ determines the potential $V_{ext}(\mathbf{r})$, it will determine the ground state energy and all other electronic properties of the system. The problem is now only how to find this density. The second theorem is helpful in this matter.

- **Theorem 2:** The ground state energy can be obtained variationally: the density that minimises the total energy is the exact ground state density.

Therefore, the total energy of the systems is a functional of electron density and can be written as:

$$\begin{aligned}
 E_{HK}[n] &= T[n] + E_{int}[n] + \int d^3r V_{ext}(\mathbf{r})n(\mathbf{r}) + E_{II} \\
 &\equiv F_{HK}[n] + \int d^3r V_{ext}(\mathbf{r})n(\mathbf{r}) + E_{II},
 \end{aligned}
 \tag{2.9}$$

where E_{II} is the interaction energy of the nuclei and $F_{HK}[n]$ is the internal energy functional. It should be noted that Hohenberg-Kohn density functional, $F_{HK}[n]$, is universal for any many-electron system. So if we know $F_{HK}[n]$ then we can determine the electron density of the ground state by simply minimizing the energy functional.

2.1.3. The Kohn-Sham Equations

The expression of the kinetic energy in terms of the electronic density is not achieved yet. This problem solved by W.Kohn and L.Sham. In 1965, Kohn and Sham (Kohn and Sham, 1965) proposed that, the exact ground-state density can be represented by the ground-state density of an auxiliary system of non-interacting particles. In this auxiliary system all the interactions between electrons are classified into an exchange-correlation term. Using with the Hartree atomic units $\hbar = m_e = e = \frac{4\pi}{\epsilon_0} = 1$ the auxiliary hamiltonian of the auxiliary independent-particle system is

$$H_{aux}^\sigma = -\frac{1}{2}\nabla^2 + V^\sigma(\mathbf{r}),
 \tag{2.10}$$

here $V^\sigma(\mathbf{r})$ is a potential acting on an electron with spin σ at point \mathbf{r} . And the density of the auxiliary system is given by

$$n(\mathbf{r}) = \sum_{\sigma} n(\mathbf{r}, \sigma) = \sum_{\sigma} \sum_{i=1}^{N^\sigma} |\psi_i^\sigma(\mathbf{r})|^2,
 \tag{2.11}$$

where ψ_i^σ is the i -th single particle orbital with spin component σ . The independent-particle kinetic energy T_s is given by

$$T_s = -\frac{1}{2} \sum_{\sigma} \sum_{i=1}^{N^{\sigma}} \langle \psi_i^{\sigma} | \nabla^2 | \psi_i^{\sigma} \rangle = \frac{1}{2} \sum_{\sigma} \sum_{i=1}^{N^{\sigma}} \int d^3r |\nabla \psi_i^{\sigma}(\mathbf{r})|^2, \quad (2.12)$$

and we can define the classical Coulomb interaction term as

$$E_{Hartree}[n] = \frac{1}{2} \int d^3r d^3r' \frac{n(\mathbf{r})n(\mathbf{r}')}{|\mathbf{r} - \mathbf{r}'|}. \quad (2.13)$$

Finally, we can write the total energy functional as follows,

$$E_{KS} = T_s[n] + \int d\mathbf{r} V_{ext}(\mathbf{r})n(\mathbf{r}) + E_{Hartree}[n] + E_{II} + E_{xc}[n], \quad (2.14)$$

$E_{xc}[n]$ contains all many-body effects of exchange and correlation. To derive the Kohn-Sham equations, we must minimise the energy with respect to the charge density $n(\mathbf{r}, \sigma)$. Because of the independent-particle kinetic energy, T_s , is explicitly expressed as a functional of the orbitals, one should calculate the gradient of the energy with respect to the orbitals

$$\frac{\delta E_{KS}}{\delta \psi_i^{\sigma*}(\mathbf{r})} = \frac{\delta T_s}{\delta \psi_i^{\sigma*}(\mathbf{r})} + \left[\frac{\delta E_{ext}}{\delta n(\mathbf{r}, \sigma)} + \frac{\delta E_{Hartree}}{\delta n(\mathbf{r}, \sigma)} + \frac{\delta E_{xc}}{\delta n(\mathbf{r}, \sigma)} \right] \frac{\delta n(\mathbf{r}, \sigma)}{\delta \psi_i^{\sigma*}(\mathbf{r})} = 0, \quad (2.15)$$

then orthonormalization condition requires

$$\langle \psi_i^{\sigma} | \psi_j^{\sigma'} \rangle = \delta_{i,j} \delta_{\sigma,\sigma'}. \quad (2.16)$$

Using expressions 2.11 and 2.12 for $n^{\sigma}(\mathbf{r})$ and T_s , which give

$$\frac{\delta T_s}{\delta \psi_i^{\sigma*}(\mathbf{r})} = -\frac{1}{2} \nabla^2 \psi_i^{\sigma}(\mathbf{r}) \quad (2.17)$$

$$\frac{\delta n^\sigma(\mathbf{r})}{\delta \psi_i^{\sigma*}(\mathbf{r})} = \psi_i^\sigma(\mathbf{r}), \quad (2.18)$$

and the Lagrange multiplier method for handling the constraints, this leads to the Kohn-Sham Schrödinger-like equations:

$$(H_{KS}^\sigma - \epsilon_i^\sigma)\psi_i^\sigma(\mathbf{r}) = 0, \quad (2.19)$$

where ϵ_i^σ are Kohn-Sham eigenenergies. And H_{KS}^σ is the effective hamiltonian

$$H_{KS}^\sigma(\mathbf{r}) = -\frac{1}{2}\nabla^2 + V_{KS}^\sigma(\mathbf{r}), \quad (2.20)$$

where $V_{KS}^\sigma(\mathbf{r})$ is Kohn-Sham potential and it is defined by

$$V_{KS}^\sigma(\mathbf{r}) = V_{ext}(\mathbf{r}) + \frac{\delta E_{Hartree}}{\delta n(\mathbf{r}, \sigma)} + \frac{\delta E_{xc}}{\delta n(\mathbf{r}, \sigma)} \quad (2.21)$$

$$= V_{ext}(\mathbf{r}) + V_{Hartree}(\mathbf{r}) + V_{xc}^\sigma(\mathbf{r}). \quad (2.22)$$

Equations 2.19-2.22 are called the Kohn-Sham Equations. The solution of the Kohn-Sham equations can be achieved by applying the iterative procedure. Some starting densities $n_0^\uparrow(\mathbf{r})$ and $n_0^\downarrow(\mathbf{r})$ are guessed, and a hamiltonian $H_{KS1}^\sigma(\mathbf{r})$ is constructed with them. The eigenvalue problem is solved, then the densities $n_1^\uparrow(\mathbf{r})$ and $n_1^\downarrow(\mathbf{r})$ are obtained with it. Most probably $n_1^\uparrow(\mathbf{r})$ and $n_1^\downarrow(\mathbf{r})$ will differ from $n_0^\uparrow(\mathbf{r})$ and $n_0^\downarrow(\mathbf{r})$. Then, $n_1^\uparrow(\mathbf{r})$ and $n_1^\downarrow(\mathbf{r})$ are used to construct $H_{KS2}^\sigma(\mathbf{r})$, which will yield a $n_2^\uparrow(\mathbf{r})$ and $n_2^\downarrow(\mathbf{r})$, etc. This procedure repeat until $n^\uparrow(\mathbf{r})$ and $n^\downarrow(\mathbf{r})$ are converged. Then using with converged values energy, Hellmann-Feynman forces (Feynman, 1939; Hellmann, 1937), stresses (Nielsen and Martin, 1985a,b) and eigenvalues can be calculated.

After Hellmann-Feynmann forces and stresses are calculated the system can be relaxed geometrically (Payne *et al.*, 1992) and find local minimum around given initial coordinates.

The Kohn-Sham wave functions must be represented as a linear combination of a set of functions, e.g. basis set. Different basis sets maybe more or less convenient for computational efficiency. There are three basic basis sets to be used in Kohn-Sham equations: linearized augmented plane waves (LAPWs), linear combinations of atomic orbitals (LCAO), and plane waves. Each method has its advantages and pitfalls.

2.1.4. Approximations to the Exchange-Correlation Potential

Up to now, except the preceding Born-Oppenheimer approximation, no other approximations were made. But exchange-correlation term has not explained yet. This term includes all the remaining complicated electronic contributions. The exchange-correlation term is very complex and can not handle simply. However, there are several approximations to the exchange correlation, namely local density approximation (LDA), generalised gradient approximation (GGA), hybrid functionals, LDA+U and exact exchange functionals.

Local Spin Density Approximation (LSDA) The most widely used approximation to handle exchange-correlation energy is the local spin density approximation (LSDA). This approximation first formulated by Kohn and Sham (Kohn and Sham, 1965) in 1965. LSDA approximation is to postulate that the density at each point is the same as that of the homogeneous electron gas. In this approximation the exchange-correlation functional is given by

$$E_{xc}^{LSDA}[n^\uparrow, n^\downarrow] = \int d^3r n(\mathbf{r}) \epsilon_{xc}(n^\uparrow(\mathbf{r}), n^\downarrow(\mathbf{r})), \quad (2.23)$$

where $\epsilon_{xc}(n^\uparrow(\mathbf{r}), n^\downarrow(\mathbf{r}))$ is the exchange-correlation energy per particle of a homogeneous electron gas. $\epsilon_{xc}(n^\uparrow(\mathbf{r}), n^\downarrow(\mathbf{r}))$ can be written as the sum of exchange and correlation contributions

$$\epsilon_{xc}(n^\uparrow(\mathbf{r}), n^\downarrow(\mathbf{r})) = \epsilon_x(n^\uparrow(\mathbf{r}), n^\downarrow(\mathbf{r})) + \epsilon_c(n^\uparrow(\mathbf{r}), n^\downarrow(\mathbf{r})), \quad (2.24)$$

where the exchange part, $\epsilon_x(n^\uparrow(\mathbf{r}), n^\downarrow(\mathbf{r}))$, can be expressed explicitly

$$\epsilon_x(n^\uparrow(\mathbf{r}), n^\downarrow(\mathbf{r})) = -\frac{1}{2^{\frac{2}{3}}} \frac{3}{8} e^2 \left(\frac{3}{\pi} n^\uparrow(\mathbf{r}) \right)^{\frac{1}{3}} - \frac{1}{2^{\frac{2}{3}}} \frac{3}{8} e^2 \left(\frac{3}{\pi} n^\downarrow(\mathbf{r}) \right)^{\frac{1}{3}}. \quad (2.25)$$

For the correlation part $\epsilon_c(n^\uparrow(\mathbf{r}), n^\downarrow(\mathbf{r}))$, there is no such explicit expression. But there are highly accurate Quantum Monte Carlo calculations for the homogeneous electron gas (Ceperley and Alder, 1980b). The LSDA is very successful approximation for many systems of interest, it gives a very good results especially for transition metals due to the fact that the electron density varies smoothly. But LSDA's results become worse with increasing inhomogeneity.

Generalized Gradient Approximation (GGA) The Generalized Gradient Approximation (GGA) uses not only the density $n(\mathbf{r})$ at a particular point, but also its gradient $\nabla n(\mathbf{r})$, in order to account for the non-homogeneity of the true electron density. In GGA the exchange-correlation energy can be written as follows,

$$E_{xc}^{GGA}[n^\uparrow, n^\downarrow] = \int d^3r n(\mathbf{r}) \epsilon_{xc}(n^\uparrow(\mathbf{r}), n^\downarrow(\mathbf{r}), \nabla n^\uparrow(\mathbf{r}), \nabla n^\downarrow(\mathbf{r})). \quad (2.26)$$

Widely used GGA's can now provide the accuracy required for density functional theory to be used in various type of analysis. Generally GGA approximation improves atomic energies, binding energies, bond lengths and bond angles when compared the ones obtained by LDA.

2.2. Light-Matter Interaction

Experimentally, the interaction of light and material is determined by absorption, reflectance and transmittance measurements. However, to predict these measurements theoretically, it is necessary to understand the interaction between the electromagnetic wave and the medium. In order to reveal this interaction, the response of the medium to the electric and magnetic fields should be examined in detail. Mark Fox's book is followed throughout this section (Fox, 2002).

2.2.1. Electromagnetic Fields in a Material

The response of a dielectric medium to an electric field is defined by the electric field strength (\vec{E}), the polarization (\vec{P}) and the electric displacement (\vec{D}) vectors. Application of a field leads to microscopic dipoles in a material aligned parallel to the direction of the external field. Since the net dipole moment per unit volume is defined as polarization, the applied field produces a polarization in the dielectric. Assuming that the material is isotropic and the relationship between \vec{P} and \vec{E} is linear, we can write the following formula

$$\vec{P} = \epsilon_0 \chi \vec{E}, \quad (2.27)$$

where ϵ_0 and χ denote the electric permittivity of free space and the electric susceptibility of the medium, respectively.

The electric displacement, \vec{D} , is related to \vec{E} and \vec{P} through:

$$\vec{D} = \epsilon_0 \vec{E} + \vec{P}. \quad (2.28)$$

By defining the relative dielectric constant of the medium as, $\epsilon_r = 1 + \chi$, the final form of the electric displacement is obtained as follows:

$$\vec{D} = \epsilon_0 \epsilon_r \vec{E}. \quad (2.29)$$

The response of a material to an external magnetic field is characterized by the magnetization of the material (\vec{M}), the magnetic field strength (\vec{H}), and the magnetic flux density (\vec{B}). Assuming that the magnetization of the material is proportional to the magnetic field strength, the magnetization of the material can be defined as follows:

$$\vec{M} = \chi_M \vec{H}, \quad (2.30)$$

where χ_M is the magnetic susceptibility of the material. The relationship between \vec{B} , \vec{M} , and \vec{H} is as follows:

$$\vec{B} = \mu_0 (\vec{H} + \vec{M}), \quad (2.31)$$

where μ_0 is the magnetic permeability of the vacuum. By defining the relative magnetic permeability of the material as, $\mu_r = 1 + \chi_M$, the final form of the magnetic flux density is obtained as follows:

$$\vec{B} = \mu_0 \mu_r \vec{H}. \quad (2.32)$$

The response of a material to the electric and magnetic fields is summarized in a compact manner in Maxwell's equations of electromagnetism:

$$\nabla \cdot \vec{D} = \rho \quad (2.33)$$

$$\nabla \cdot \vec{B} = 0 \quad (2.34)$$

$$\nabla \times \vec{E} = -\frac{\partial \vec{B}}{\partial t} \quad (2.35)$$

$$\nabla \times \vec{H} = \vec{j} + \frac{\partial \vec{D}}{\partial t} \quad (2.36)$$

where ρ and \vec{j} denote the free charge density and the current density, respectively. The first and second equations describe the Gauss's law of electrostatics and magnetostatics, respectively, with the assumption that free magnetic monopoles do not exist. The third equation combines the Faraday and Lenz laws of electromagnetic induction and the last equation is the Ampere's law. When the last two equations are examined in a medium with no free charge ($\rho = 0$) or current ($\vec{j} = 0$), they take the following form:

$$\nabla \times \vec{E} = -\mu_0\mu_r \frac{\partial \vec{H}}{\partial t} \quad (2.37)$$

$$\nabla \times \vec{H} = \epsilon_0\epsilon_r \frac{\partial \vec{E}}{\partial t}. \quad (2.38)$$

By taking the curl of $\nabla \times \vec{E}$ with substituting the $\nabla \times \vec{H}$, the following equation is obtained:

$$\nabla \times (\nabla \times \vec{E}) = -\mu_0\mu_r\epsilon_0\epsilon_r \frac{\partial^2 \vec{E}}{\partial t^2}. \quad (2.39)$$

Using the vector identity, $\nabla \times (\nabla \times \vec{E}) = \nabla(\nabla \cdot \vec{E}) - \nabla^2 \vec{E}$, the final result is obtained:

$$\nabla^2 \vec{E} = \mu_0\mu_r\epsilon_0\epsilon_r \frac{\partial^2 \vec{E}}{\partial t^2}. \quad (2.40)$$

It is clear that this equation is the wave equation with $\frac{1}{\sqrt{\mu_0\mu_r\epsilon_0\epsilon_r}}$ is the velocity (v) of the wave. The solutions of this equation are in the form of

$$\vec{E}(z, t) = \vec{E}_0 e^{i(kz - \omega t)}, \quad (2.41)$$

where \vec{E}_0 and z denote the amplitude and the direction of propagation of wave, respectively. k is the wave vector and ω is the angular velocity.

The refractive index (n) of a medium is defined as the ratio of light velocity in the free space ($c = \frac{1}{\sqrt{\mu_0\epsilon_0}}$) to velocity in the medium:

$$n = \frac{c}{v} = \sqrt{\epsilon_r\mu_r}. \quad (2.42)$$

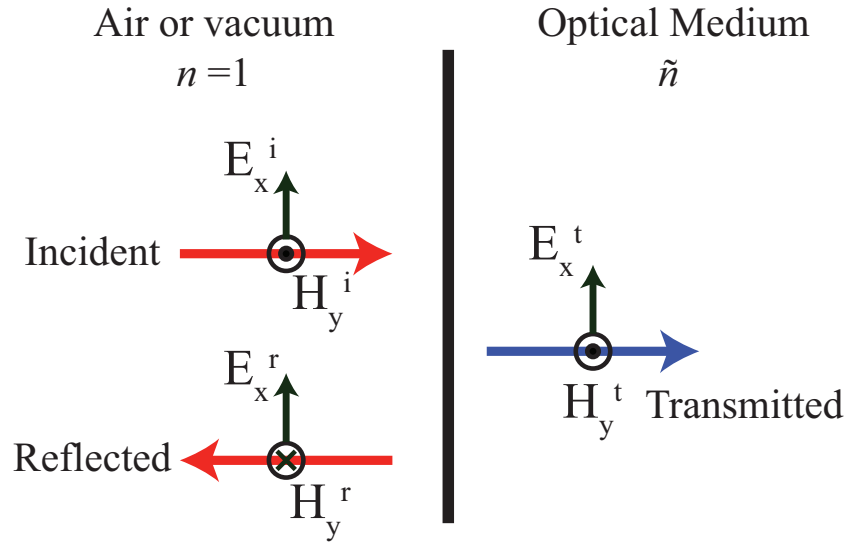


Figure 2.1. The reflection and transmission of light at an interface between air and a medium of refractive index \tilde{n} .

Therefore, at optical frequencies ($\mu_r = 1$) the refractive index is $n = \sqrt{\epsilon_r}$. The magnitude of the k is defined as $k = \frac{2\pi}{\lambda} = \frac{\omega}{v} = \frac{n\omega}{c}$, where λ is the wavelength of the wave inside the medium.

The direction of the electric field in the electromagnetic wave is defined as polarization. There are several types of polarization such as linear, circular and elliptical. Maxwell's equations allow us to describe the transmission and reflection of beam at an interface between two different media. As an example, consider a linearly polarized wave propagating along the z axis with the polarization direction along the x axis as shown in the Figure 2.1. Since Maxwell's equations require the electric and magnetic fields to be perpendicular to each other, E , H and k form the right-handed system seen in the Figure 2.1. The beam is incident on a medium with refractive index \tilde{n} . The tilde indicates the refractive index is considered to be complex. In many cases it is necessary to consider the refractive index as a complex number, as will be explained in detail in the next section. The electric and magnetic fields vary sinusoidally in space and the components of the

complex fields are of the form:

$$\vec{E}_x(z, t) = \vec{E}_{x0} e^{i(kz - \omega t)} \quad (2.43)$$

$$\vec{E}_y(z, t) = 0 \quad (2.44)$$

$$\vec{H}_x(z, t) = 0 \quad (2.45)$$

$$\vec{H}_y(z, t) = \vec{H}_{y0} e^{i(kz - \omega t)}. \quad (2.46)$$

By substituting these complex fields in the Maxwell's equations, the following equation is obtained:

$$\vec{H}_{y0} = \frac{\vec{E}_{x0}}{Z}, \quad (2.47)$$

where

$$Z = \frac{k}{\mu_0 \mu_r \omega} = \sqrt{\frac{\mu_0 \mu_r}{\epsilon_0 \epsilon_r}} = \frac{1}{c \epsilon_0 \tilde{n}}. \quad (2.48)$$

The boundary conditions at the interface between two media require that the tangential components of the electric and magnetic fields are continuous. Therefore, \vec{E}_x and \vec{H}_y must be conserved across the boundary:

$$\vec{E}_x^i + \vec{E}_x^r = \vec{E}_x^t, \quad (2.49)$$

$$\vec{H}_y^i - \vec{H}_y^r = \vec{H}_y^t, \quad (2.50)$$

where i , r and t denote the incident, reflected, and transmitted beams, respectively. Using the relationship between the electric and magnetic fields, the second equation can be written as follows:

$$\vec{E}_x^i - \vec{E}_x^r = \tilde{n} \vec{E}_x^t, \quad (2.51)$$

where the beam is incident from air $\tilde{n} = 1$ and at the optical frequencies ($\mu_r = 1$). The equations obtained from the conservation of electric and magnetic fields can be solved together and the following relationship can be revealed:

$$\frac{\vec{E}_x^r}{\vec{E}_x^i} = \frac{\tilde{n} - 1}{\tilde{n} + 1}. \quad (2.52)$$

In order to obtain the reflectivity (R), the above formula can be written as follows:

$$R = \left| \frac{\vec{E}_x^r}{\vec{E}_x^i} \right|^2 = \left| \frac{\tilde{n} - 1}{\tilde{n} + 1} \right|^2. \quad (2.53)$$

In addition, the reflection on the interface of two materials with refractive indices \tilde{n}_1 and \tilde{n}_2 can be expressed as follows:

$$R = \left| \frac{\tilde{n}_2 - \tilde{n}_1}{\tilde{n}_2 + \tilde{n}_1} \right|^2. \quad (2.54)$$

2.2.2. The Complex Refractive Index and Dielectric Constant

In this section, the importance of complex refraction index (\tilde{n}) in determining optical properties of materials will be examined in detail. The complex refraction index is given by the following equation:

$$\tilde{n} = n + i\kappa \quad (2.55)$$

where n is the normal refractive index ($\frac{c}{v}$) and κ is the extinction coefficient. In the previous section, it is shown that the electric field of the wave propagating along the z direction is given as follows:

$$\vec{E}(z, t) = \vec{E}_0 e^{i(kz - \omega t)}. \quad (2.56)$$

Since the wave vector in an absorbing medium having a complex refractive index is expressed as $\vec{k} = \tilde{n} \frac{\omega}{c} = (n + ik) \frac{\omega}{c}$, the final form of the electric field is given as follows:

$$\vec{E}(z, t) = \vec{E}_0 e^{-\frac{\kappa \omega z}{c}} e^{i\left(\frac{n \omega z}{c} - \omega t\right)}. \quad (2.57)$$

Therefore, the presence of extinction coefficient leads to an exponential decay of the wave in the medium. Since the optical intensity of a light wave is proportional to the square of the electric field, the intensity decrease exponentially in the medium with a decay constant equal to $2 \times (\kappa w/c)$. The Beer's law states that the intensity of light propagating in the z direction in a medium decreases exponentially with an α constant:

$$I(z) = I_0 e^{-\alpha z}, \quad (2.58)$$

where $I(z)$ and α denote the intensity at position z and absorption coefficient, respectively. Therefore, the absorption coefficient, α , is directly proportional to the extinction coefficient, κ :

$$\alpha = \frac{2\kappa w}{c} = \frac{4\pi\kappa}{\lambda}. \quad (2.59)$$

In the previous section, it is revealed that the refractive index of a medium at the optical frequencies ($\mu_r = 1$) is $n = \sqrt{\epsilon_r}$. Hence, if the refractive index is complex, then ϵ_r must also be complex. The complex refractive index ($\tilde{\epsilon}_r$) can be defined as:

$$\tilde{\epsilon}_r = \epsilon_1 + i\epsilon_2. \quad (2.60)$$

By using the relation of $\tilde{n}^2 = \tilde{\epsilon}_r$, the following equations between the real and the imaginary parts of \tilde{n} and $\tilde{\epsilon}_r$ can be obtained.

$$\epsilon_1 = n^2 - \kappa^2, \quad (2.61)$$

$$\epsilon_2 = 2n\kappa, \quad (2.62)$$

$$n = \frac{1}{\sqrt{2}}(\epsilon_1 + (\epsilon_1^2 + \epsilon_2^2)^{1/2})^{1/2}, \quad (2.63)$$

$$\kappa = \frac{1}{\sqrt{2}}(-\epsilon_1 + (\epsilon_1^2 + \epsilon_2^2)^{1/2})^{1/2}. \quad (2.64)$$

In the weakly absorbing mediums, the κ value becomes very small and the last two equations take the following forms:

$$n = \sqrt{\epsilon_1}, \quad (2.65)$$

$$\kappa = \frac{\epsilon_2}{2n}. \quad (2.66)$$

In addition, the reflectivity given at the end of the previous section can be expressed as follows depending on n and κ :

$$R = \left| \frac{\tilde{n} - 1}{\tilde{n} + 1} \right|^2 = \frac{(n - 1)^2 + \kappa^2}{(n + 1)^2 + \kappa^2}, \quad (2.67)$$

and the transmissivity in the strongly absorbing medium can be expressed as

$$T = (1 - R)^2 e^{-\alpha l} \quad (2.68)$$

where l is the thickness of the material.

Thus, these equations reveal that \tilde{n} and $\tilde{\epsilon}_r$ are not independent variables and all the measurable optical properties can be obtained from n and κ . This section focuses on obtaining frequency-dependent dielectric constants using the classical dipole oscillator model. In this model, it is assumed that an electron binds to nucleus by a spring and they form an electric dipole with a magnitude proportional to the distance from each other. The electric field of the incoming light wave induces driving forces on the electrons of the atomic dipole and causes them to make forced oscillations. Since the nucleus mass is much greater than the electron mass, the motion of the nucleus can be ignored. Hence, the resonant frequency (w_0) of the atomic dipole is determined by electron mass (m_0) and the magnitude of the restoring force (K_s),

$$w_0 = \sqrt{\frac{K_s}{m_0}}. \quad (2.69)$$

The displacement, x , of the electron is governed by the following differential equation:

$$m_0 \frac{d^2 x}{dt^2} + m_0 \gamma \frac{dx}{dt} + m_0 w_0^2 x = -eE, \quad (2.70)$$

where e is the magnitude of the electric charge, γ is the damping rate, and E is the electric field of the incoming light. Suppose this system interacts with a light wave with

the electric field given below

$$E(t) = E_0 \cos(\omega t + \Phi) = E_0 \operatorname{Re}(e^{-i(\omega t + \Phi)}), \quad (2.71)$$

where E_0 , ω , and Φ are the amplitude, angular frequency, and the phase of the light. The solution of the differential equation is given in the following form

$$x(t) = X_0 \operatorname{Re}(e^{-i(\omega t + \Phi')}), \quad (2.72)$$

where X_0 and Φ' denote amplitude and phase of the oscillations, respectively. By incorporating phase factors into amplitudes, we obtain the final forms of $x(t) = X_0 e^{-i\omega t}$ and $E(t) = E_0 e^{-i\omega t}$. By substituting the final forms of $x(t)$ and $E(t)$ into the differential equation of motion, the amplitude of X_0 can be obtained as follows

$$X_0 = \frac{-eE_0/m_0}{\omega_0^2 - \omega^2 - i\gamma\omega}. \quad (2.73)$$

Since the displacement of an electron from its equilibrium position generates a dipole moment, $p(t) = -ex(t)$, the resonant polarization (P_{res}) of a system containing N atoms per volume is given by:

$$P_{res} = Np = -Nex = \frac{Ne^2}{m_0} \frac{1}{\omega_0^2 - \omega^2 - i\gamma\omega} E. \quad (2.74)$$

In general, a medium may have multiple resonant frequencies, thus the total polarization can be given as:

$$P = \frac{Ne^2}{m_0} \sum_j \frac{1}{\omega_j^2 - \omega^2 - i\gamma_j\omega} E, \quad (2.75)$$

where ω_j and γ_j denote the angular frequency and damping coefficient of a particular resonance line, respectively. In the previous section, the relationship between D , E and P is given as follows

$$\vec{D} = \epsilon_0 \vec{E} + \vec{P}. \quad (2.76)$$

In addition, the relative dielectric constant is defined through the following equation:

$$\vec{D} = \epsilon_0 \epsilon_r \vec{E}. \quad (2.77)$$

The last two equations are combined and \vec{P} is substituted in the combined equation to obtain the final form of the relative dielectric constant as follows:

$$\epsilon_r(\omega) = \epsilon_1 + i\epsilon_2 = 1 + \frac{Ne^2}{\epsilon_0 m_0} \sum_j \frac{1}{\omega_j^2 - \omega^2 - i\gamma_j \omega}. \quad (2.78)$$

Hence, the real and imaginary parts of relative dielectric constant can be given as:

$$\epsilon_1(\omega) = 1 + \frac{Ne^2}{\epsilon_0 m_0} \sum_j \frac{\omega_j^2 - \omega^2}{(\omega_j^2 - \omega^2)^2 + (\gamma_j \omega)^2}, \quad (2.79)$$

$$\epsilon_2(\omega) = \frac{Ne^2}{\epsilon_0 m_0} \sum_j \frac{\gamma_j \omega}{(\omega_j^2 - \omega^2)^2 + (\gamma_j \omega)^2}. \quad (2.80)$$

The absorption lines obtained using the classical dipole oscillator model have the same strength. However, experimental results reveal that the absorption strength changes considerably between different atomic transitions. The inconsistency between the results of classical model and the experiments arises from the fact that classical model does not take into account changes in the quantum mechanical transition probability. The results of the classic model can be corrected by assigning a phenomenological oscillator strength, f_j , to each transition:

$$\epsilon_r(\omega) = 1 + \frac{Ne^2}{\epsilon_0 m_0} \sum_j \frac{f_j}{\omega_j^2 - \omega^2 - i\gamma_j \omega}. \quad (2.81)$$

2.2.3. Interband Absorption

In the previous section, it is stated that the classical oscillator model is insufficient to determine the frequency dependence of refractive index and absorption coefficient and quantum mechanics should be used to calculate the transition energies and the oscillator strengths. This section investigates the interband absorption process that occurs when an electron is excited to an empty state through absorbing a photon by a material. The main

purpose of this section is to reveal the relationship between the absorption spectrum and the band structure of a material using quantum mechanical approaches. Depending on the electronic band structure of a material, direct or indirect transitions can be observed in the optical spectrum. Since the investigation of indirect transition is very complicated and out of our main purpose, only direct transitions will be considered in this section.

The calculation of the absorption coefficient, α , by quantum mechanics can be achieved by obtaining the interband transition rates ($W_{i \rightarrow f}$). Fermi's golden rule provides a simple expression for the transition rates between the initial (ψ_i) and final (ψ_f) states of a quantum system exposed to a perturbation:

$$W_{i \rightarrow f} = \frac{2\pi}{\hbar} |M|^2 g(\hbar\omega), \quad (2.82)$$

where M is the matrix element and describes the effect of perturbation on the electrons by photon. $g(\hbar\omega)$ denotes the joint density of states.

Electric field of a photon leads to a variation in the energy of a charged particle. The perturbation hamiltonian that describe the electric-dipole interaction between the electron and light can be given as follows:

$$H' = -\vec{p}_e \cdot \vec{E}_{photon}, \quad (2.83)$$

where \vec{p}_e is equal to $-e\vec{r}$. The electric field of the light can be described as plane waves of the following form:

$$\vec{E}_{photon}(\vec{r}) = \vec{E}_0 e^{i\vec{k} \cdot \vec{r}}. \quad (2.84)$$

Since the electron states in a crystal are described by Bloch functions, the initial and final state wave functions can be written as a product of a plane wave and an envelope function with the periodicity of the crystal lattice:

$$\psi_i(\vec{r}) = \frac{1}{\sqrt{V}} u_i e^{i\vec{k}_i \cdot \vec{r}}, \quad (2.85)$$

$$\psi_f(\vec{r}) = \frac{1}{\sqrt{V}} u_f e^{i\vec{k}_f \cdot \vec{r}}, \quad (2.86)$$

where V is the normalization volume, k_i and k_f denote the wave vectors of the initial and final states respectively, and u_i and u_f are the appropriate envelope functions for the

initial and final bands, respectively. Effect of the external perturbation of the light wave on the electrons can be given with the following matrix element:

$$M = \langle f | H' | i \rangle = \int \psi_f^*(\vec{r}) H'(\vec{r}) \psi_i(\vec{r}) d^3\vec{r}, \quad (2.87)$$

$$M = \frac{e}{V} \int u_f^*(\vec{r}) e^{-i\vec{k}_f \cdot \vec{r}} (\vec{E}_0 \cdot \vec{r}) e^{i\vec{k} \cdot \vec{r}} u_i(\vec{r}) e^{i\vec{k}_i \cdot \vec{r}} d^3\vec{r}. \quad (2.88)$$

The conservation of momentum requires that $\hbar\vec{k}_f - \hbar\vec{k}_i = \hbar\vec{k}$. Therefore, the final form of M can be given as the following formula:

$$M = \frac{e}{V} \int u_f^*(\vec{r}) (\vec{E}_0 \cdot \vec{r}) u_i(\vec{r}) d^3\vec{r}. \quad (2.89)$$

This matrix element shows the electric-dipole moment of the transition and it is directly related to polarization of the light wave and the envelope functions of the crystal.

Another factor determining transition rates in the interband absorption formalism is the joint density of states ($g(\hbar\omega)$). The joint density of states determines amount of allowed optical transitions between the occupied valence band states and the unoccupied conduction band states separated by photon energy $\hbar\omega$. The density of states per unit energy range can be given as $g(E)dE = 2g(k)dk$, where $g(k)$ denotes density of states in k -space and extra factor of 2 stems from two electron spin states of each k state. Therefore, $g(E)$ can be described as

$$g(E) = \frac{2g(k)}{dE/dk}, \quad (2.90)$$

where dE/dk is the derivative of the $E - k$ dispersion curve. The number of k states per unit volume of k space can be given as

$$g(k)dk = \frac{1}{(2\pi)^3} 4\pi k^2 dk = \frac{k^2}{2\pi^2} dk. \quad (2.91)$$

The final form of interband transition rates and hence the absorption coefficient can be expressed as follows:

$$\alpha \propto W_{i \rightarrow f} \propto \frac{2e^2}{\pi\hbar V^2} \left| \int u_f^*(\vec{r}) (\vec{E}_0 \cdot \vec{r}) u_i(\vec{r}) d^3\vec{r} \right|^2 \frac{k^2}{dE/dk}. \quad (2.92)$$

Therefore, the absorption coefficient can be determined by obtaining the envelop functions and calculating the derivative of the $E - k$ dispersion curve. In the previous section, it is revealed that the absorption coefficient is related to the imaginary part of the dielectric function for a materials with very small extinction coefficient.

In addition to interband absorption, quasiparticle energies and exciton formations should be considered to accurately calculate the optical spectrum.

2.2.4. Quasiparticle Energies

Although the DFT calculates very accurately the ground state properties of materials, the excited state properties of materials cannot be calculated with bare DFT. In order to calculate the electronic excitations such as, single-electron addition and removal energies in the photoemission experiment, beyond DFT approaches should be used. One of the most common ways of calculating excited state properties of materials is to use the GW approach based on many-body perturbation theory (MBPT).

An electron in a solid repels other electrons and surrounded by a positively charged polarization cloud. The structure consisting of an electron and a positively charged polarization cloud surrounding it is called a quasiparticle. Therefore, particles in a solid interact with screened Coulomb potential. In order to calculate the excited state properties of materials, the quasiparticle energies should be calculated. The quasiparticle energies (E_i) can be calculated by solving the following equation,

$$\left(\frac{1}{2} \nabla^2 + V_{Hartree}(\vec{r}) + V_{ext}(\vec{r}) \right) \psi_i(\vec{r}, w) + \int d\vec{r}' \Sigma(\vec{r}, \vec{r}', w) \psi_i(\vec{r}', w) = E_i(w) \psi_i(\vec{r}, w), \quad (2.93)$$

where ψ_i and $\Sigma(\vec{r}, \vec{r}', w)$ are the quasiparticle eigenstates and self energy operator, respectively. The $\Sigma(\vec{r}, \vec{r}', w)$ is non-local, energy dependent and a non Hermitian operator. $\Sigma(\vec{r}, \vec{r}', w)$ can be represented as

$$\Sigma(\vec{r}, \vec{r}', w) = \frac{i}{4\pi} \int e^{iw\delta} G(\vec{r}, \vec{r}', w + w') W(\vec{r}, \vec{r}', w') dw' \quad (2.94)$$

where G is the single-particle Green's function,

$$G(\vec{r}, \vec{r}', w) = \sum_n \frac{\psi_i(\vec{r}, w) \psi_i^*(\vec{r}', w)}{w - E_n + i\eta \text{sgn}(E_n - \mu)} \quad (2.95)$$

and W is the screened Coulomb interaction,

$$W(\vec{r}, \vec{r}', w) = \frac{e^2}{4\pi\epsilon_0} \int d\vec{r}'' \frac{\epsilon^{-1}(\vec{r}, \vec{r}'', w)}{|\vec{r} - \vec{r}''|}. \quad (2.96)$$

The quasiparticle energies can be calculated by writing diagonal elements

$$E_i = \mathbf{Re} [\langle \psi_i | T + V_{ext} + V_{Hartree} + \Sigma(E_i) | \psi_i \rangle]. \quad (2.97)$$

This can be solved iteratively by using Newton-Raphson method starting from the Kohn-Sham eigenvalues

$$E_i \leftarrow E_i + Z_i \mathbf{Re} [\langle \psi_i | T + V_{ext} + V_{Hartree} + \Sigma(E_i) | \psi_i \rangle - E_i], \quad (2.98)$$

where Z_i is normalization factor ranging from 0 to 1,

$$Z_i = \left(1 - \mathbf{Re} \left[\left\langle \psi_i \left| \frac{\partial}{\partial w} \Sigma(w) \right| \psi_i \right\rangle \right] \right). \quad (2.99)$$

2.2.5. Excitonic Effect and the Bethe-Salpeter Equation

Experimental studies have shown that the optical gap of materials lower than the quasiparticle band gap. Excitonic effects can dominate the optical response of ultra-thin materials. In order to take into account excitonic effects two-particle Green function of electron-hole pairs should be used.

We can write an excited state as

$$S = \sum_{\mathbf{k}} \sum_v^{hole} \sum_c^{elec} A_{v\mathbf{c}\mathbf{k}}^S \hat{a}_{v\mathbf{k}}^\dagger \hat{b}_{c\mathbf{k}+\mathbf{Q}}^\dagger |0\rangle \quad (2.100)$$

where $A_{v\mathbf{c}\mathbf{k}}^S$ is the electron-hole amplitude. We can calculate eigenstates and eigenvalues by solving the Bethe-Salpeter equation (BSE)

$$(E_{c,\mathbf{k}+\mathbf{Q}} - E_{v,\mathbf{k}}) A_{v\mathbf{c}\mathbf{k}}^S + \sum_{v'\mathbf{c}'\mathbf{k}'} \langle v\mathbf{c}\mathbf{k} | K^{eh} | v'\mathbf{c}'\mathbf{k}' \rangle A_{v'\mathbf{c}'\mathbf{k}'}^S = \Omega_S A_{v\mathbf{c}\mathbf{k}}^S \quad (2.101)$$

where Ω_S and K^{eh} are the excitation energy and electron-hole interaction kernel, respectively. The frequency dependent dielectric function can be obtained by solving the Bethe Salpeter equation;

$$\epsilon_2(w) = \frac{16\pi e^2}{w^2} \sum_S \left| \frac{\vec{P}}{|\vec{P}|} \cdot \langle 0 | \frac{i}{\hbar} [H, \vec{r}^\dagger] | S \rangle \right|^2 \delta(w - \Omega_S) \quad (2.102)$$

\vec{P} is the polarization of the absorbed photon.

2.3. Computational Methodology

Unless otherwise specified, all the calculations in this thesis were performed using the projector augmented wave (PAW) (Kresse and Joubert, 1999; Blöchl, 1994) potentials as implemented in the Vienna *ab initio* simulation package (VASP)(Kresse and Hafner, 1993; Kresse and Furthmüller, 1996). In order to describe the exchange and correlation potential, Perdew-Burke-Ernzerhof (PBE) version of generalized gradient approximation (GGA)(Perdew *et al.*, 1996) was used with the inclusion of spin-orbit coupling (SOC) unless otherwise stated. To obtain the partial charge on the atoms, the Bader technique was used (Henkelman *et al.*, 2006). The total energy difference between the sequential steps in the iterations was taken as 10^{-5} eV as a convergence criterion. The total force in the unit cell was reduced to a value of less than 10^{-4} eV/Å. Brillouin Zone integration was performed using sufficiently dense Γ -centered k -point samplings to accurately determine the charge densities of each system. Phonon calculations were performed by making use

of the small displacement method as implemented in the PHON software package (Alfè, 2009).

CHAPTER 3

ELECTRONIC PROPERTIES OF ATOMICALLY THIN LAYERED MATERIALS

Due to their structural diversity and tunable electronic structure, 2D materials are quite attractive materials for variety of applications such as spintronic, supercapacitors, electronics, optoelectronics, solar cells and chemical sensors. Their extraordinary properties make the two-dimensional materials very important for fundamental and applied researches. For instance, graphene exhibits ultrahigh room-temperature carrier mobility (Novoselov *et al.*, 2004), quantum Hall effect and Berry's phase (Zhang *et al.*, 2005), excellent electrical conductivity (Novoselov *et al.*, 2004). It has been shown that the large TMD family shows diverse electronic properties like metallic, semi-metallic, semiconductor and even superconductors with various structural phases such as 1H, 1T and 1T' (Ataca *et al.*, 2012). MoS₂ was shown to have high room temperature mobility (Radisavljevic *et al.*, 2011), indirect to direct band gap transition (Mak *et al.*, 2010), and layer-dependent tunable band gap (Zhu *et al.*, 2016).

Modification of the electronic properties of these materials is achievable through various methods. 2D materials consist of weakly stacked layers that allow them to be exfoliated up to atomically thin layers. In recent years, it has been revealed that important changes can be made in the fundamental properties of the 2D materials depending on the thickness and they can acquire various new features. It was revealed that an indirect to direct band gap transition from bulk to monolayer limit in TMDs leads to great enhancement of photoluminescence (Mak *et al.*, 2010; Tonndorf *et al.*, 2013). A significant increase in the band gap of black Phosphorene (black P) was reported when it is thinned down to a single layer (Das *et al.*, 2014; Woomer *et al.*, 2015). Recently, thickness dependence of magnetism in ultra-thin CrI₃ was reported (Huang *et al.*, 2017). While monolayer structure has ferromagnetism, bilayer exhibits antiferromagnetism and three-layer and bulk structures show ferromagnetism again.

Another commonly used method for the functionalization of ultra-thin materials is to dope the material with impurity atoms/molecules or to create a defect in the material. During the synthesis of ultra-thin materials several kind of defects such as point impurities, dislocations and vacancies are inevitable. These defects are the major scat-

tering centers and traps of charge carriers which could limit or improve the performance of materials. Previous studies showed that electronic properties of monolayer MoS₂ can be easily tuned by intrinsic defects (Zhou *et al.*, 2013; Ghorbani-Asl *et al.*, 2013). The intrinsic magnetism has been observed in monolayer TMDs due to the localized defect states (Zhang *et al.*, 2013). The bonding characteristics of individual Si impurities in graphene materials were detected experimentally and results are confirmed by DFT calculations (Zhou *et al.*, 2012). Moreover, it was revealed that photoluminescence intensity of monolayer TMDs can be enhanced by point defects and these defects lead to a new photoemission peak (Refaely-Abramson *et al.*, 2018).

In addition, external strain or pressure can have a profound effect on the electronic and optical properties of 2D materials. Bissett *et al.* demonstrated that the chemical reactivity of graphene can be significantly increased by stretching of the supporting flexible substrate (Bissett *et al.*, 2013). It was reported that the monolayer MoS₂ is flexible, strong and has a Young modulus comparable to steel (Bertolazzi *et al.*, 2011). He *et al.* showed that the electronic band gap of atomically thin MoS₂ can be controlled by applying uniaxial tensile strain (He *et al.*, 2013). Previous studies revealed that monolayer black-phosphorus and monolayer black-arsenic can sustain very high tensile strains thanks to their puckered structures (Kandemir *et al.*, 2019; Wei and Peng, 2014).

3.1. Vacancy Defect and Foreign Atom Adsorption

Previously, it was shown that vacancy defects and foreign atom impurities can easily occur in 2D materials and can lead to significant changes in the electronic and magnetic properties of the material (Zhou *et al.*, 2013; Ghorbani-Asl *et al.*, 2013; Zhang *et al.*, 2013). In this section, firstly, the electronic properties of pristine and defective structures of monolayer TiS₃ and then the effect of hydrogenation on the structural and electronic properties of monolayer TiSe₂ are examined in detail.

3.1.1. Vacancy Formation and Oxidation Characteristics of Single Layer TiS₃

In addition to TMDs (MoX₂ X= S, Se, Te) having graphene-like crystal structure, recent efforts have also led to the synthesis of novel ultra-thin layered materials with

entirely different crystal structures. Titanium trisulphide (TiS_3) is one of the most recent examples of such layered transition metal chalcogenides.

The atomic structure belongs to the space group $P2_1/m$ and TiS_3 crystallizes in bundles of molecular chains that are formed by trigonal prisms, where the metal atoms occupy the centers of the prisms (Brattas and Kjekshus, 1972; Furuseth *et al.*, 1975). Finkman *et al.* (Finkman and Fisher, 1984) have shown that TiS_3 crystals are semiconducting with extrinsic n-type conductivity that have room temperature mobility of $30 \text{ cm}^2/(\text{V sec})$. Recently, strong nonlinearity of the current–voltage characteristics has been reported by Gorlova *et al.* (Gorlova *et al.*, 2012, 2010). In contrast to many other layered TMDs which exhibit an indirect to direct band gap transition at the monolayer limit, TiS_3 exhibits a direct band gap even for a width of hundreds of layers. Direct optical transitions with a band gap of 1.10 eV have been detected in thin films of TiS_3 (Ferrer *et al.*, 2013). Moreover, these thin films show photocurrent response to white light illumination (Ferrer *et al.*, 2012).

Using high-resolution TEM for defective crystals, a metal-to-insulator transition with charge localization below $T_{MI} \approx 325 \text{ K}$ has been proposed by Guilmeau *et al.* (Guilmeau *et al.*, 2014). Their studies revealed that TiS_3 has low thermal conductivity and a large absolute value of the Seebeck coefficient at high temperatures. Furthermore, in a recent study by Island *et al.* (Island *et al.*, 2014) field effect transistors (NR-FET) have been fabricated at room temperature by isolating few-layer TiS_3 nanoribbons. The electron mobility of few-layer TiS_3 was found to be $2.6 \text{ cm}^2/(\text{V sec})$, and exhibits n-type semiconductor behavior with ultrahigh photoresponse and fast switching times.

Although experimental and theoretical studies have been performed on bulk TiS_3 , to our knowledge, up to now there are no studies on the characteristic properties of single-layer TiS_3 . In this study, motivated by the recent experimental results of Island *et al.* (Island *et al.*, 2015), we investigate: (i) structural and electronic properties of single layer TiS_3 , (ii) formation of vacancies in the pristine material and their influence on electronic properties, and (iii) environmental stability of its surface against oxidation.

3.1.1.1. Single Layer TiS_3

The unit cell of monolayer TiS_3 is a rectangular prism and is composed of 2 Ti atoms and 6 S atoms. The coordination of these atoms are illustrated by the top and tilted-side views in Figures 3.1(a) and 3.1(b), respectively. The monolayer TiS_3 is composed of chain-like structures consisting of trigonal prisms with the metal atom occupying the

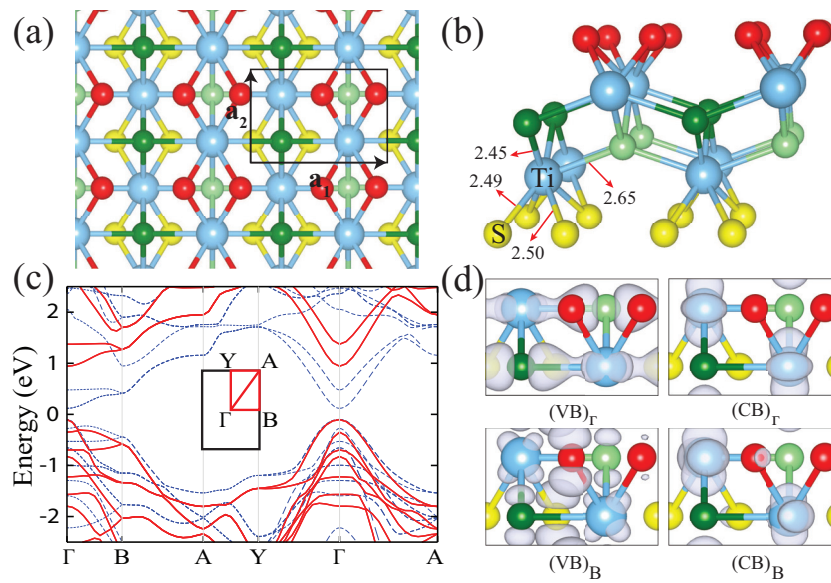


Figure 3.1. (a) Top view of monolayer TiS_3 and its unit cell shown by a rectangle. For a better top view, S atoms in different layers are presented by different colors. (b) Tilted side view of $2 \times 2 \times 1$ supercell of monolayer TiS_3 . (c) Blue dashed lines and red lines illustrate PBE + vdW and PBE + vdW + HSE06 results for the electronic band diagram of monolayer TiS_3 , respectively. (d) Band decomposed charge densities of valance band (VB) and conductance band (CB) at Γ and B.

centers of these prisms. In this phase, chains are parallel to the a_2 and they form layers in the a_1a_2 plane, which are coupled with each other by the van der Waals interaction to form the bulk layered structure of TiS_3 . Our calculations show that monolayer TiS_3 has lattice vectors $a_1 = 4.99 \text{ \AA}$ and $a_2 = 3.39 \text{ \AA}$. These lattice parameters are comparable to the experimental bulk results $a_1 = 4.958 \text{ \AA}$, $a_2 = 3.4006 \text{ \AA}$, $a_3 = 8.778 \text{ \AA}$, and $\beta = 97.32$. Brattas, Furuseth As shown in Figure 3.1(b) the bond distances of Ti atom and two different surface S atoms (red or yellow S atoms) are 2.49 \AA and 2.50 \AA , respectively. At the same time, these two surface S atoms are two of the three base S atoms of the trigonal prisms. The bond distance of Ti atom and third base S atom (dark or light green S atoms) of the trigonal prism is 2.45 \AA . The atom-atom distance of Ti atom and S atom (light or dark green S atoms) of neighboring prism is 2.65 \AA .

Charge density analysis is an efficient way to discuss the character of the inter-atomic interactions and bonding. In Figure 3.2, we present a cross section of the 3D total charge density. Bader charge analysis shows that in parallel to their electronegativity values a significant amount of charge is transferred from Ti to the S atoms. While two S atoms at the surface (shown by red balls) share 0.7 electrons donated by the underlying Ti atom, 0.8 electron transfer occurs from Ti to S atom in the middle of the crystal (shown by light green balls). Thus, Ti-S bonds between surface and inner S atoms have an entirely different character. As is also delineated in Figure 3.2 the bond between Ti and inner S atoms is constructed through 0.8 electron transfer and therefore it has an ionic character. However, the bonds between Ti and surface S atoms are constructed through relatively less electron transfer and hence it has mostly covalent character. It is also seen from Figure 3.2 that each surface atom interacts with neighboring S atoms while there is no contact between the inner S atoms. Therefore one expects anisotropic electronic and transport properties due to the varying character of the surface states along a_1 and a_2 directions. It is also worth mentioning that the negatively charged surface of monolayer TiS_3 may find interesting applications such as nanoscale lubricants and charged coatings.

Calculated band diagrams of pristine TiS_3 using PBE + vdW and PBE + vdW + HSE06 methods are shown in Figure 3.1(c). It is known that often the values, obtained with the PBE functional underestimates the energy band gaps of semiconductors. The band gap of TiS_3 is calculated to be 0.23 eV by using the PBE+vdW approximation. However, including the HSE06 correction one gets a 1.05 eV direct band gap at the Γ point, which is in good agreement with the experimental value of 1.10 eV, for few-layer TiS_3 (Ferrer *et al.*, 2013, 2012). For further analysis of the band structure of TiS_3 , charge densities of the valence band maximum (VB) and the conduction band minimum (CB)

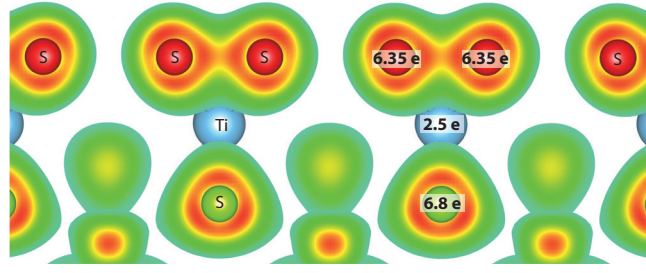


Figure 3.2. Cross-sectional plane view of the charge densities, with two surface, and one inner S atom placed at this plane. Valance charges on inner and outer S atoms are also shown. Color code of atoms is the same as in Figure3.1. Electron density increases from green to red.

at the Γ and the B high-symmetry points are shown in Figure 3.1(d). It is seen that the VB is composed of $2p_x$ orbitals of S and $3d_{xz}$ orbitals of Ti and they form a strong bond, whereas the main contribution to the CB edge comes from $3d_{y^2-z^2}$ orbitals of Ti atom at the Γ point. At the B point, p_y orbitals of S atoms dominant while $3d_{xy}$ orbitals of Ti atom contribute slightly to the VB. In particular, p orbitals of surface S atoms are larger than p orbitals of the inner S atoms. Thus, the main contribution to the VB is dominated by p_y orbitals of the surface S atoms. Like at the Γ point, while the S atoms do not contribute significantly, all the contribution comes from the $3d_{y^2-z^2}$ orbitals of the Ti atom to the CB. In the trigonal prisms every Ti atom shares 4 valence electrons with 3 base S atoms and 1 neighboring chain S atom. Due to the lack of any unsaturated orbitals, monolayer TiS_3 has a nonmagnetic ground state.

3.1.1.2. Defective Single Layer TiS_3

In this section, the effect of various vacancy defects on the structural, electronic and magnetic properties of monolayer TiS_3 is investigated.

S-vacancy

The first defective structure we consider is a single S vacancy in TiS_3 monolayer. To compare the geometric structure of monolayer TiS_3 in the presence and absence of a vacancy, a 3×3 supercell is considered and the lattice vectors for the defect-free TiS_3

Table 3.1. Lattice parameters, formation energies, magnetic moments, and electronic characteristics of 3×3 supercell of monolayer TiS_3 and its few defected forms.

	a_1 / a_2 (\AA)	E_F (eV)	m (μB)	Electronic Characteristic
Pristine TiS_3	14.98 / 10.18	-	0.0	Semiconductor
S Vacancy	14.90 / 10.17	3.58	0.0	Semiconductor
Ti Vacancy	15.05 / 10.14	12.00	0.5	Metal
Double S Vacancy	14.96 / 10.18	8.48	0.8	Metal
Ti, S Vacancy	14.90 / 10.13	16.15	0.3	Metal

computational supercell are found as $a_1 = 14.98 \text{ \AA}$ and $a_2 = 10.18 \text{ \AA}$. Fully relaxed geometric structure when a single S atom is removed from the surface of monolayer TiS_3 is shown in Figure 3.3(a). When S vacancy is introduced the lattice vectors of 3×3 supercell change and become $a_1 = 14.90 \text{ \AA}$ and $a_2 = 10.17 \text{ \AA}$. Thus, the presence of the S vacancy leads to a minute shrinkage of the lattice vectors of TiS_3 . As can be seen from Figure 3.3(a), the nearest surface S atom to the vacancy follows the direction of the arrow, localizes on top of the inner S atom (light green) and forms reconstructed bonds with the nearest Ti atoms with a bond length of 2.32 \AA . Bader charge analysis tells us that, the total charge of this atom is increased by 0.4 electrons when removing the nearest neighbor S atom. The charges of other atoms do not change significantly with the removal of the surface S atom. Our calculated results show that the formation energy of an S-vacancy is 3.58 eV.

In Figures 3.4(a) and 3.4(b), GGA calculated density of states (DOS) for pristine and S-atom-removed TiS_3 are shown, respectively. As can be seen from the figures, removing one S atom from the surface of TiS_3 does not make any notable effect on the electronic structure of TiS_3 . The monolayer conserves its semiconductor character. Due to the reconstruction of the S atom and its binding with 2 Ti atoms, there are no unsaturated bonds. Thus, the nonmagnetic character of the TiS_3 is preserved during the formation of an S-vacancy.

Ti-vacancy

Relaxed geometric structure when a single Ti atom is extracted from TiS_3 is illustrated in Figure 3.3(b). A significant surface reconstruction is observed after geometric relaxation. This figure shows that, when one Ti atom is taken out, the displacement of

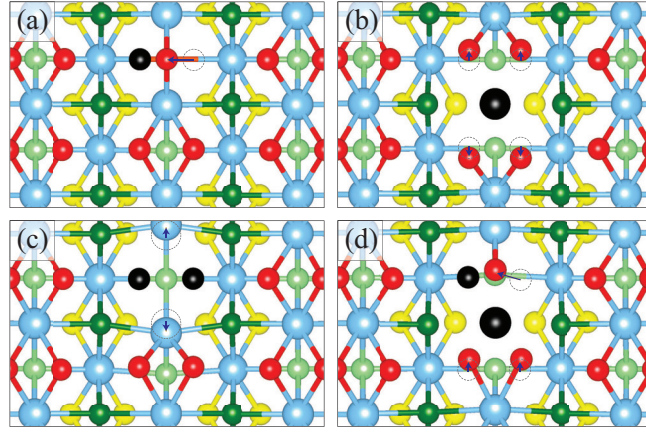


Figure 3.3. Top view of relaxed monolayer TiS_3 with (a) S-vacancy, (b) Ti-vacancy, (c) Double S-vacancy, (d) TiS-vacancy. Black atoms illustrate removed atoms, dashed circles show initial position of the displaced atom. Color code of the other atoms is the same as in Figure 3.1. The direction of displaced atoms are depicted by blue arrows.

the inner S atoms that were attached to it, is not significant, nevertheless they lose 0.1 electrons. However, the four surface S atoms are released, they move towards the other Ti atoms and they lose approximately 0.2 electrons. This gives rise to an expansion in the lattice parameter a_1 , which after relaxation becomes $a_1 = 15.05 \text{ \AA}$ and $a_2 = 10.14 \text{ \AA}$. Hence, removal of Ti atom leads to an increase in a_1 , whereas a decrease in a_2 . The formation energy of Ti-vacancy is 12.00 eV. Defects with high formation energies are unlikely to form, and therefore an S-vacancy will have a much higher probability to form as compared to a Ti-vacancy.

Unlike S vacancy, Ti vacancy has a major effect on the electronic structure of TiS_3 , it loses its semiconductor character and becomes metallic. As seen from Figure 3.4(c), at the Fermi level, there is a slight spin polarization and the contribution from the S atom is more than that of the Ti atom. As given in Table 3.1, TiS_3 monolayer with a Ti-vacancy exhibits a magnetic ground state and the calculated magnetic moment is $0.5 \mu_B/\text{supercell}$.

Double S-vacancy

Possible two-atom-vacancy structures of TiS_3 are also investigated. First, the structure of double S atoms removed from the surface of TiS_3 is studied. Figure 3.3(c) presents its fully relaxed configuration. Compared to the one S vacancy situation, the lattice is more deformed. The double vacancy of surface S atoms leads to a reconstruction of

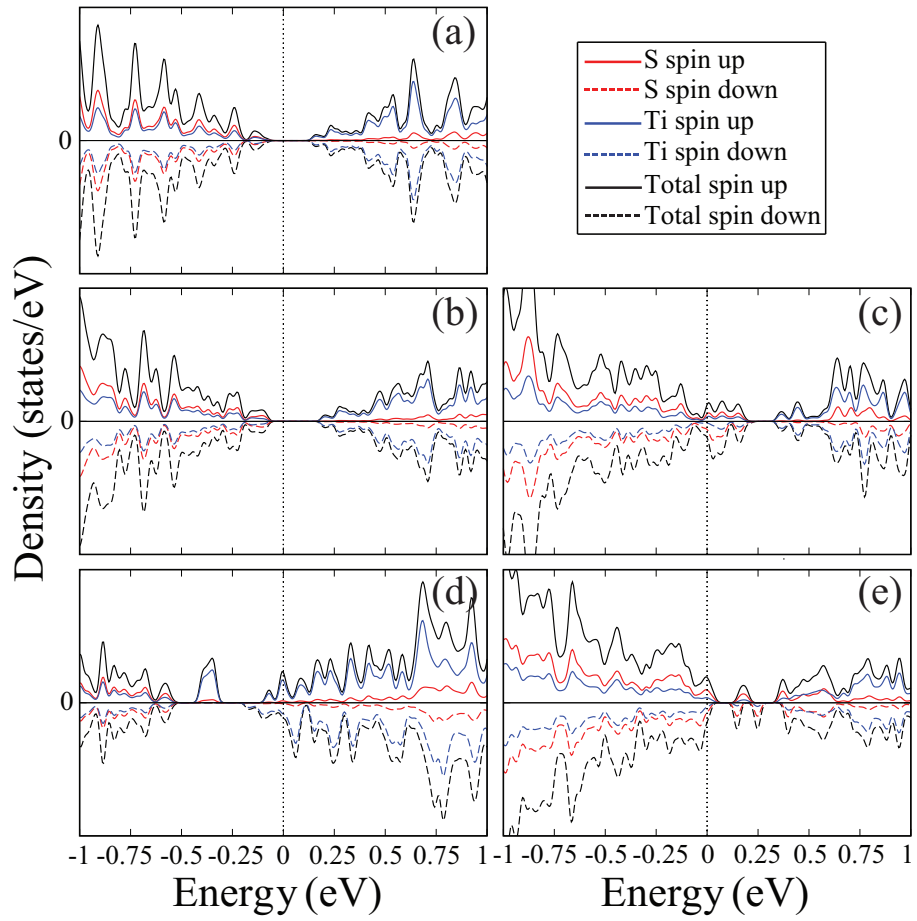


Figure 3.4. Density of states of (a) pristine TiS_3 , with (b) S-vacancy, (c) Ti-vacancy, (d) Double S-vacancy, and (e) TiS -vacancy.

the bonds between the S atoms of neighboring prisms (dark green one) and the Ti atoms closest to the vacancies. These Ti atoms become more strongly bonded to the surface S atoms. However, compared to the defect-free structure, when two S atoms are removed the lattice parameters are slightly changed. Bader charge analysis shows that, removing two surface S atoms does not affect the charges of the remaining Ti atoms. However, 0.7 excess electrons of the removed two S atoms are shared by neighbor S atoms. The formation energy of double S-vacancy is 8.48 eV. Thus, removing two S atoms from the TiS_3 surface is more probable than removing one Ti atom.

The calculated density of states of monolayer TiS_3 with double S-vacancy is presented in Figure 3.4(d). When the second S atom is taken out from the surface, TiS_3 exhibits metallic character. As seen from Figure 3.4(d) the main contribution comes from the Ti atoms and TiS_3 with double S-vacancy has an asymmetric DOS at the Fermi level. This asymmetric DOS at the Fermi level leads to a magnetic ground state with the magnetic moment value of $0.8 \mu_B/\text{supercell}$.

TiS-vacancy

Lastly, we considered the defected structure of TiS_3 with a TiS-vacancy. Figure 3.3(d) shows that in the presence of TiS-vacancy, the position of the closest surface S atom to the removed S atom is significantly changed. This atom follows the direction of the arrow and becomes located at the top of the inner S atom (light green) with charge 6.6 electrons. Other two surface S atoms move toward the vacancies and their charges reduce to 6.0 and 6.2 electrons. The lattice parameters reduce to the values $a_1 = 14.90 \text{ \AA}$ and $a_2 = 10.13 \text{ \AA}$. Compared to the other vacancy types its formation energy value is the highest with the value 16.15 eV.

DOS diagram of TiS_3 with TiS-vacancy is illustrated in Figure 3.4(e). Like Ti and double S-vacancies, this vacancy type also leads to a metallic character. But, unlike the double S-vacancy, Fermi level consists of orbitals of S atom. As given in Table 3.1, the magnetic moment of this case is $0.3 \mu_B/\text{supercell}$.

3.1.1.3. Oxidation of Pristine and Defective Single Layer TiS_3

It is well-known that two-dimensional ultra-thin structures such as graphene, MoS_2 , phosphorene etc. are prone to oxidation (Vinogradov *et al.*, 2011; Wang *et al.*, 2015; Yamamoto *et al.*, 2013). Therefore, the search for structural and environmental stability of

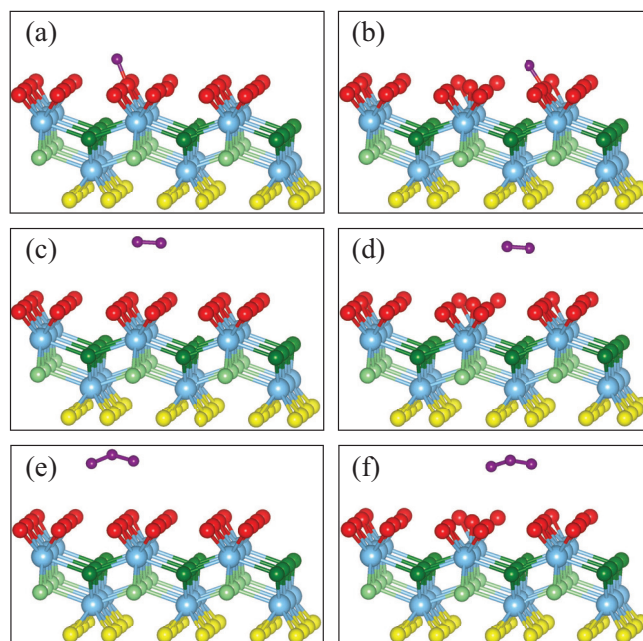


Figure 3.5. Tilted side view of (a) O, (c) O₂ and (e) O₃ adsorbed on pristine TiS₃. (b) O, (d) O₂ and (f) O₃ adsorbed on an S-vacant TiS₃.

TiS₃ is of importance. After the investigation of possible defect types in monolayer TiS₃, in this section we address the oxidation process and the role of vacancies in that process.

O atom adsorption on pristine and defective TiS₃

We start to investigate the oxidation with atomic Oxygen on pristine TiS₃. The atmosphere comprises various molecules which contain O, like O₂, H₂O, CO₂, etc. Thus, during experiments in ambient conditions, the presence of O atom is inevitable. As shown in Figure 3.5(a), the optimized structures show that, an O atom is adsorbed by an S atom on the pristine TiS₃ surface. The distance between O and S atoms is about 1.49 Å. The presence of the O atom does not have any significant effect on the lattice structure of TiS₃. O atom binds strongly to the S atom whose bond has an ionic character. The amount of charge transfer between O and S atoms is about 1.3 electrons from S to the O atom. The binding energy of the O atom on TiS₃ crystal is -3.89 eV. When O atom binds to the TiS₃ surface, it loses its magnetic moment and the whole system does not exhibit any net magnetic moment.

The vacancy calculations have shown that the most probable defect type of TiS₃ is the S atom vacancy. Since the O atom readily binds to the pristine TiS₃ surface, the

effect of the S-vacancy on the adsorption of atomic O is in order. Figure 3.5(b) shows that, instead of being the nearest S atom to the vacancy, O atom prefers to bind to the other surface-S atom from tilted-top site. Compared to the pristine case, the presence of the S vacancy increases the binding energy of O atom from -3.89 eV to -4.01 eV. The bond distance between O and S atoms is 1.48 Å. Unlike the pristine case, O atom distorts the lattice of defective TiS_3 and the new lattice vectors are expanded to $a_1 = 14.93$ Å and $a_2 = 10.19$ Å. O atom binds ionically to the surface S atom and 1.1 electrons transfer from surface S atom to the O atom. Like in the pristine case, the net magnetic moment of the whole system is zero.

We also investigate substitutional adsorption of O atom on the surface of single layer TiS_3 . The formation energy of the substitutional O atom at S site is calculated using the formula $E_{Subs} = E_{M+O} - E_M - E_O + E_S$, where E_{M+O} denotes the energy of O-doped TiS_3 , E_M is the energy of pristine TiS_3 , E_O and E_S are single atom energies. Substitution energy of O with S is found to be -1.38 eV. Negative value for O atom indicates the spontaneous formation of substitutional doping at the S site for O atom. It is also seen that the presence of substitutional O does not change the nonmagnetic structure of TiS_3 .

O_2 molecule adsorption on pristine and defective TiS_3

Approximately 21% of the earth atmosphere is composed of O_2 molecules. Thus, the binding mechanism of O_2 molecule on TiS_3 surface and the stability of TiS_3 in the presence of this molecule are very crucial. The results of our calculations show that compared to atomic O, the O_2 molecule binds very weakly to the TiS_3 surface and its binding energy is -0.07 eV. Figure 3.5(c) shows that O_2 locates 3.2 Å above the TiS_3 surface and it prefers to bind on top of the vicinity of S atom. The presence of O_2 on the TiS_3 surface does not cause any distortion on the lattice structure. Contrary to the single O atom case, there is no significant charge transfer between the surface and the molecule. Total magnetic moment of the system is $2\mu_B$, which is equal to the magnetic moment of an isolated O_2 molecule.

The presence of an S-vacancy does not have any significant effect on the adsorption of O_2 molecule on the TiS_3 crystal. Similar to the pristine case, O_2 molecule binds rather weakly to S-vacancy with a binding energy of -0.05 eV. Compared to the pristine case, O_2 molecule is localized more close to the TiS_3 surface at a z -distance of 2.89 Å. The presence of O_2 molecule does not cause any notable distortion of the defected TiS_3 crystal. Like in the pristine case, there is almost no charge transfer between TiS_3 and the O_2 molecule and the net magnetic moment of O_2 molecule which is $2\mu_B$, does not change

in the presence of the S-vacancy.

O₃ molecule adsorption on pristine and defective TiS₃

To complete the analysis of oxidation of TiS₃, the binding mechanism of the O₃ molecule on the TiS₃ surface is investigated. It is found that, compared to O₂ molecule, O₃ molecule binds more strongly to the TiS₃ surface. Binding energy of O₃ molecule on TiS₃ surface is -0.21 eV. As seen from Figure 3.5(e), O₃ molecule locates 3.15 Å above the TiS₃ surface with two edge O atoms being closer to the surface compared to the middle O atom. The stability of TiS₃ is not affected by O₃. When the O₃ molecule is placed on the TiS₃ surface, it receives an extra 0.2 electrons from the TiS₃. The net magnetic moment of the O₃ molecule adsorbed pristine TiS₃ is zero.

Finally, the adsorption of O₃ molecule on an S-vacancy is investigated. As seen from Figure 3.5(f), O₃ molecule locates approximately 2.95 Å above the TiS₃ surface. In the S vacancy case the end O atoms are placed closer to the surface compared to the middle O atom. Presence of S vacancy slightly affects the binding energy of O₃ molecule which is equal to -0.20 eV. O₃ molecule does not make any significant effect on the lattice structure of TiS₃ with an S-vacancy. The charge transfer from the surface to the molecule is about 0.2 electrons. The adsorbed O₃ molecule on an S-vacancy does not possess any net magnetic moment.

3.1.1.4. Conclusions

In this work, a detailed analyses of structural, electronic and magnetic properties of pristine, defective and oxidized structures of monolayer TiS₃ are presented by using first-principles calculations. In addition to the PBE version of GGA, the HSE06 form of hybrid functionals were also used to describe the exchange-correlation density functional. Electronic structure calculations using HSE06 hybrid functional indicated that monolayer TiS₃ is a direct band gap semiconductor with a band gap of 1.05 eV. Our calculations also revealed interesting bonding nature of the monolayer TiS₃ crystal that has ionic character inside and covalent character for surface atoms. The negatively charged surface of the crystal may also find some interesting applications.

Among various vacancy defects including S, Ti, TiS and double S vacancies, the single S vacancy has the lowest formation energy. While the S vacancy leads to an opening in the band gap, other vacancies result in metallicity in single layer TiS₃. Pristine

and S vacancy defected TiS_3 does not possess any net magnetic moment, whereas other considered vacancies are magnetic. Our DFT oxidation studies revealed that, TiS_3 readily oxidizes with atomic O. Moreover, it is found that, oxidation of TiS_3 with O_3 is most likely to occur, while oxidation with O_2 is less favorable on pristine and S defected TiS_3 surface. S vacancy has a slightly negative effect on the adsorption of O_2 and O_3 molecules on TiS_3 surface, however it has a favoring effect on the adsorption of atomic O.

3.1.2. Hydrogenation of Single-layer TiSe_2

One of the recently synthesized single layer TMDs is TiSe_2 (Sugawara *et al.*, 2015). TiSe_2 has an octahedral crystal structure with van der Waals stacked layers. Although there are several experimental studies to determine whether the electronic structure of bulk TiSe_2 is semiconducting or semimetallic, the exact electronic structure of it remains controversial. Among TMDs, bulk TiSe_2 has sparked particular attention due to its $(2 \times 2 \times 2)$ charge-density-wave (CDW) transition with periodic lattice distortions at a critical temperature $T_C \sim 202$ K (Di Salvo *et al.*, 1976). CDW transition has been extensively studied in several 2D TMDs, recently. For instance, layered TaS_2 (Ritschel *et al.*, 2015), TaSe_2 (Samnakay *et al.*, 2015) and NbSe_2 (Xi *et al.*, 2015) have been synthesized and their transition temperatures to the CDW phase have been reported. CDW phase in the single layer form of TiSe_2 is more robust than that of bulk with an elevated $T_C \sim 232$ K (Chen *et al.*, 2015). The transition is attributed to band structure effect stemming from energy minimization. Angle-resolved photoemission spectroscopy (ARPES) measurements show that single-layer TiSe_2 has a temperature-tunable small band gap at room temperature and the gap increases with decreasing temperature (Chen *et al.*, 2015). Fang *et al.* showed that distortions of Ti and Se atoms in the CDW phase of TiSe_2 are related to their atomic mass ratio (Fang *et al.*, 2017).

To functionalize 2D materials, many strategies have been proposed, such as applying strain (Johari and Shenoy, 2012; Song *et al.*, 2015)), fabrication of their nanoribbons (Yagmurcukardes *et al.*, 2016; Chen *et al.*, 2017)), implanting impurities and vacancies (Komsa *et al.*, 2012; Iyikanat *et al.*, 2014)). For example, Nair *et al.* synthesized fluorographene by exposing of graphene to atomic F (Nair *et al.*, 2010). It was found that fluorographene is an insulator with an optical gap of 3 eV. Produced fluorographene shows similar mechanical properties with graphene. Sahin *et al.* have reported possible chlorinated graphene derivatives (Sahin and Ciraci, 2012). It was found that two-face chlorinated graphene is stable and it is a direct gap semiconductor. Hydrogen is commonly

used to functionalize 2D materials. For example, Elias *et al.* have found that compared to pristine graphene, the electronic properties of hydrogenated graphene (graphane) change drastically (Elias *et al.*, 2009). Moreover, it was shown that the reaction with hydrogen is reversible, thus distinctive properties of graphene can be restored. In the recent study of Bacaksiz *et al.*, the interaction between H atom and PbI_2 surface was studied (Bacaksiz and Sahin, 2016). It was reported that (2×1) and (2×2) Jahn-Teller type distortions occur for the half-hydrogenated and full hydrogenated PbI_2 , respectively. These reconstructions lead to significant modifications on the electronic and magnetic properties of the material.

Motivated by these studies, in this work, structural, phononic, thermal and electronic properties of pristine and fully-hydrogenated single-layer TiSe_2 were studied by using density functional theory based calculations. It was found that TiSe_2 has a distorted CDW phase in its ground state. The phase transition from distorted CDW phase to T_d phase is observed via hydrogenation of TiSe_2 . In addition, the effect of hydrogenation on the characteristic properties of single-layer TiSe_2 was investigated.

3.1.2.1. Pristine TiSe_2

A single-layer TiSe_2 consists of stacked Se-Ti-Se atomic layers. Ti and Se atoms are strongly bound within the layer. Recent ARPES and scanning tunneling microscopy (STM) measurements revealed that single-layer TiSe_2 exhibits a (1×1) 1T phase at room temperature and a (2×2) CDW phase at low temperatures (Peng *et al.*, 2015; Sugawara *et al.*, 2015).

Structural Properties

The optimized atomic structures of 1T and CDW phases of TiSe_2 are shown in Figure 3.6 (a). The lattice parameters of the optimized crystal structures of (1×1) 1T and (2×2) CDW phases are 3.50 and 7.00 Å, respectively. 1T phase belongs to $P\bar{3}m1$ space group, with an hexagonal Bravais lattice. The bond distance between Ti and Se atoms for 1T phase is 2.55 Å. On the other hand, CDW phase exhibits periodic lattice distortions and Ti-Se bond lengths vary from 2.49 Å to 2.63 Å. There are two types of Ti (Se) atoms in the unit cell. While one of Ti (Se) remains fixed, the other is displaced to form the lattice distortions. Fixed and displaced Ti (Se) atoms in the unit cell are labeled as Ti_f (Se_f) and Ti_d (Se_d), respectively (shown in Figure 3 (a)). Proportional magnitudes and directions of atomic displacements of displaced Ti and Se are shown by dark blue and

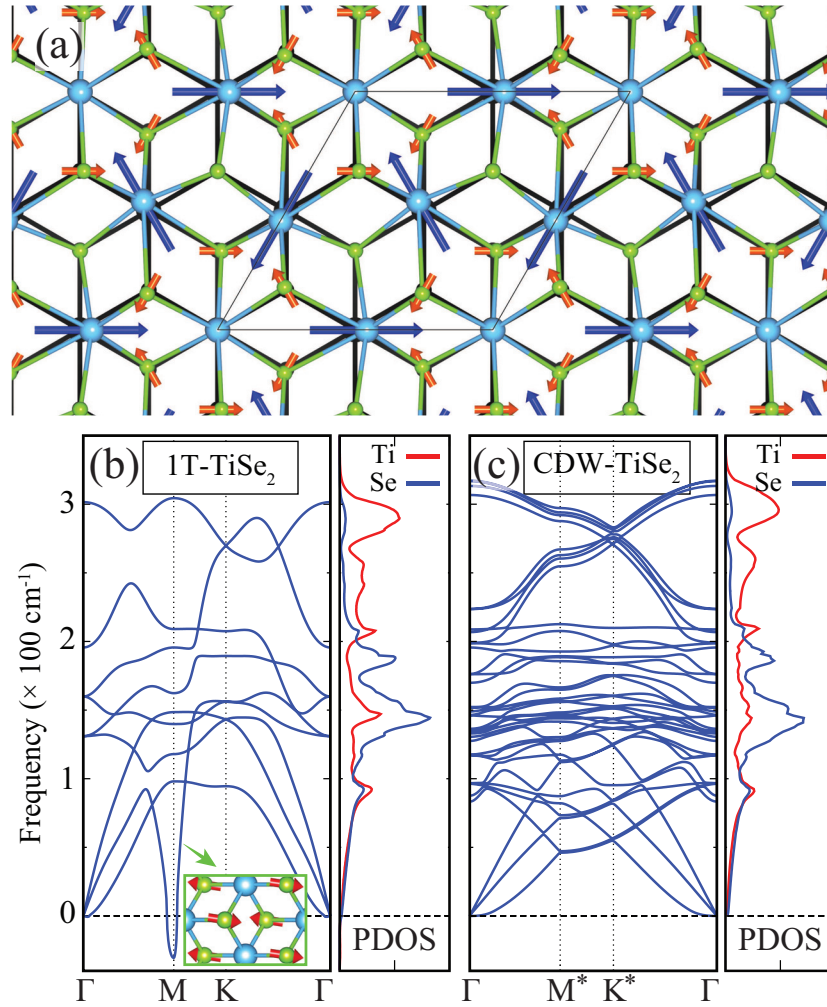


Figure 3.6. (a) Top view of CDW phase of single-layer TiSe₂. Black lattice in the background illustrates the 1T phase of TiSe₂. Light blue and green balls illustrate Ti and Se atoms, respectively. Dark blue and orange vectors show proportional magnitudes and directions of the relevant atomic displacements. Phonon band diagrams and partial phonon DOS of (b) 1T phase (Inset: Top view of atomic displacements of the corresponding mode) and (c) CDW phase of single-layer TiSe₂.

orange vectors in Figure 3.6 (a). The calculated atomic displacements of Ti and Se atoms are 0.09 Å and 0.03 Å, respectively. To determine the most favorable structure of single-layer TiSe₂, the total energies of 1T phase and CDW phase for the same number of atoms are calculated. It is found that CDW phase is energetically the most favorable structure, which has 4 meV lower energy per formula unit than the 1T phase.

Phononic Properties

Vibrational properties are critical for the analysis of dynamic stability of a material. The phonon dispersions of 1T and CDW phases of single-layer TiSe₂ are shown in Figures 3.6 (b) and (c), respectively. The unit cells of 1T and CDW phases consist of 3 and 12 atoms, respectively. Therefore, the phonon dispersion of the 1T phase yields 3 acoustic and 6 optical modes, whereas that of CDW phase possesses 3 acoustic and 33 optical modes. The force constant matrix is calculated by displacing atoms from their equilibrium positions in $6 \times 6 \times 1$ and $3 \times 3 \times 1$ supercells for the (1×1) 1T and (2×2) CDW phases, respectively.

Figure 3.6 (b) shows that 1T phase is dynamically unstable with a Kohn-type soft phonon mode at the M high symmetry point (Kohn, 1959). In order to further understand the instability of the 1T phase, atomic displacements of the soft phonon mode are shown in the inset of Figure 3.6 (b). It is seen that the mode responsible for the instability of the 1T phase is due to in-plane motion of Se atoms towards to Ti-Ti bonding center. Imaginary eigenfrequencies at the M high symmetry point indicate the lack of required restoring force against the motion of Se atoms towards to Ti-Ti bonding center, and they can be cured by a structural phase transition from 1T phase to CDW phase. As seen from Figure 3.6(c), phonon spectra of (2×2) CDW phase have positive eigenfrequencies in the whole Brillouin Zone that indicate the dynamical stability of the CDW phase. As seen in Figure 3.6(c), distortions of the CDW phase lead to almost flat phonon bands near the 200 cm^{-1} . It is known that materials with hexagonal (or trigonal) crystal symmetry exhibit linear crossing phonon branches at the K high symmetry point. As clear from Figure 3.6(a), despite the distorted structure, trigonal symmetry of the CDW phase is protected. Therefore, phonon dispersion of the CDW phase exhibits the linear crossing at the K^* high symmetry point (shown in Figure 3.6 (c)).

In addition, partial phonon density of states of 1T and CDW phases are also shown in Figure 3.6. For both phases, the low-frequency modes, below 100 cm^{-1} , originate from vibrations of the Ti and Se atoms. The medium-frequency modes, 100-200 cm^{-1} , are dominated by vibrations of the Se atom, whereas the high-frequency modes, above

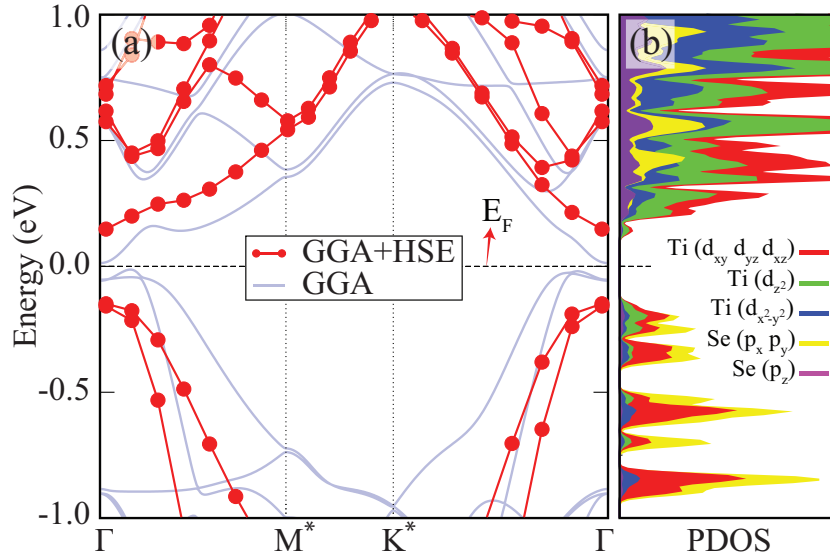


Figure 3.7. (a) The energy-band structure of CDW phase of TiSe₂. Light blue and red-dotted bands are for GGA and GGA+HSE, respectively. (b) GGA+HSE calculated partial density of states of CDW phase of TiSe₂.

200 cm⁻¹, are mainly composed of vibrations of the Ti atom, since atomic mass of Se is higher than Ti.

Electronic Properties

The electronic band structure and partial density of states (PDOS) of CDW phase of single-layer TiSe₂ are shown in Figure 3.7. The band gap of TiSe₂ is calculated to be 25 meV by using the PBE approximation. Since the bare PBE functional usually underestimates the band gap of semiconducting materials, the HSE06 functional is used to get a more precise band gap. Therefore, TiSe₂ is found to be a direct gap semiconductor with a band gap of 319 meV with HSE06 functional. The valence band maximum (VBM) and conduction band minimum (CBM) reside at the Γ point, as shown in Figure 3.7. The calculated electronic band structure within HSE06 agrees well with previous experimental and theoretical results. Chen, Sugawara

Previous studies showed that *p-d* orbital hybridizations play an important role in determining the electronic and structural characteristics of 4*d*-TMDs (Yu *et al.*, 2017). Therefore, these orbital interactions deserve considerable attention to determine exact electronic structure of single-layer TiSe₂. Calculated PDOS reveals that the CBM is made up of the *t*_{2*g*} (*d*_{*xy*}, *d*_{*yz*}, *d*_{*zx*}) and *d*_{*z*²} orbitals of Ti atoms. The states in the vicinity of VBM

are mainly composed of hybridization of t_{2g} and d_{z^2} orbitals of Ti atom and p_x and p_y orbitals of Se atom. Near the Fermi level, overlap of PDOS peak positions and shapes of p orbitals of Se atom and d orbitals of Ti atom reveal strong coupling of these orbitals.

In 4d-TMDs (such as (1×1) 1T phase of TiSe_2) Ti atoms can interact with each other through intermetal t_{2g} orbitals. Due to weak coupling of these orbitals, t_{2g} states are mostly located near the Fermi level, with no energy gap. Differing from the (1×1) 1T phase, periodic lattice distortions of the (2×2) CDW phase lead to increase in the intermetal t_{2g} orbital interactions. Furthermore, excess electrons of Se atoms lead to attractive interaction in the t_{2g} - p orbitals. Therefore, Se atoms are exposed to a force towards to Ti-Ti bonding center and occupied p states of the Se atom shift to lower energies. As a result, CDW phase transition has a significant effect on the electronic structure and leads to opening of a band gap in TiSe_2 .

3.1.2.2. Interaction with a Single H atom

Understanding of the adsorption properties of a single H atom on TiSe_2 is crucial to the investigation of its hydrogenated derivatives.

Structural and Electronic Properties

We simulate the adsorption of a H atom on a CDW phase of single-layer TiSe_2 by considering six inequivalent adsorption sites, as illustrated in Figure 3.8 (a). A 2×2 supercell of TiSe_2 containing 16 Ti and 32 Se is used to hinder H-H interaction. The nearest distance between H adatoms is larger than 14 Å. The atomic positions were fully relaxed starting from the six different adatom initial configurations: Ti_f , Ti_d , Se_f^t , Se_f^b , Se_d^t , and Se_d^b as shown in Figure 3.8. The binding energy of a H atom is calculated as

$$E_b = E_{\text{TiSe}_2} + E_H - E_{\text{TiSe}_2+\text{H}} \quad (3.1)$$

where E_{TiSe_2} denotes the energy of the (2×2) supercell of CDW phase of single-layer TiSe_2 , E_H is the energy of isolated H atom, and $E_{\text{TiSe}_2+\text{H}}$ denotes the total energy when the H is adsorbed on TiSe_2 .

Calculated lattice constants, binding energies, and the equilibrium distance between the adatom and the nearest Se atom are given in Table 3.2. It is found that the

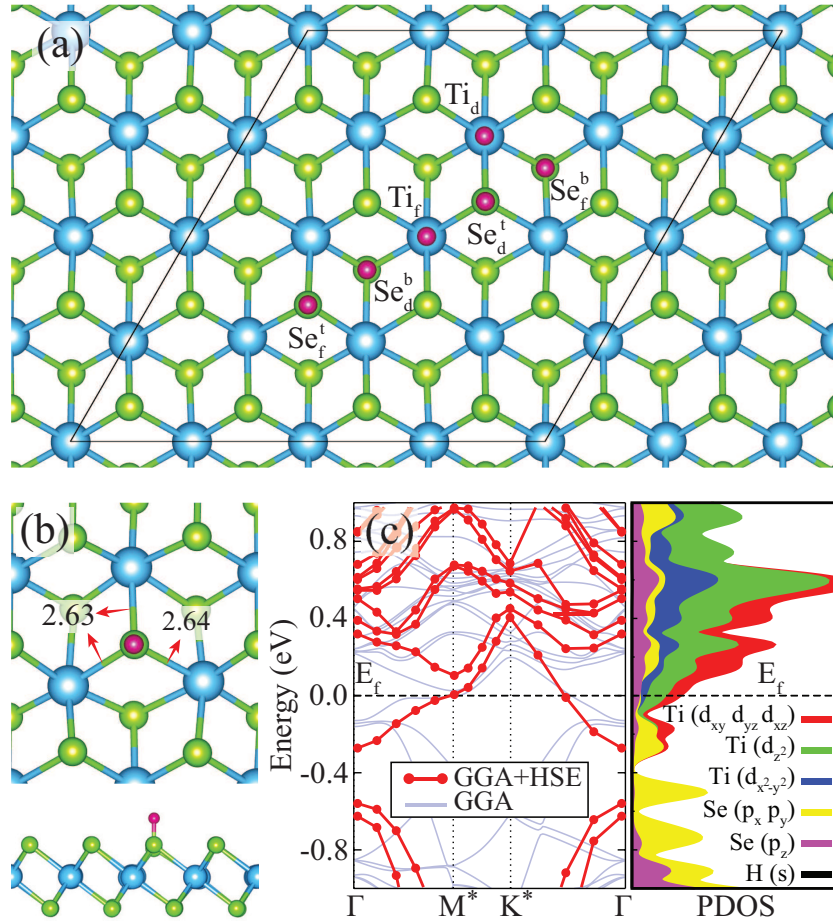


Figure 3.8. (a) Top view of six inequivalent adsorption configurations for a H atom on CDW phase of TiSe₂. (b) Top and side views of fully relaxed geometric structure of single H atom adsorbed CDW phase of TiSe₂. (c) The electronic band structure and PDOS of single H atom adsorbed CDW phase of TiSe₂. Light blue and red-dotted bands are for GGA and GGA+HSE, respectively.

binding energy of H atom is 1.69 eV for both configuration H on top of Se_f^t or Se_d^t . These sites are energetically the most favorable ones. When a single H adsorption is introduced, the 2×2 supercell of TiSe_2 enlarges from 14.00 Å to 14.08 Å. As shown in Figure 3.8 (b), the adsorbed H atom modifies the local atomic structure around it. The nearest Se-Ti bonds to the adsorbed atom are increased from 2.49, 2.56, and 2.63 Å to 2.63, 2.63, and 2.64 Å, respectively. The distance between H and Se atoms is 1.48 Å.

Energy-band dispersion and PDOS of a H atom-adsorbed single-layer TiSe_2 are shown in Figure 3.8 (c). When single H atom is adsorbed on TiSe_2 , the structure becomes metallic. Although H atom has a major effect on the electronic structure of TiSe_2 , the states originating from H atom reside at deep energy levels, as shown in Figure 3.8 (c). The states around the Fermi level are mainly composed of d orbitals of Ti atoms. The presence of a H adatom does not change the nonmagnetic character of TiSe_2 .

Table 3.2. The lattice constants, a and b ; the distance from adsorbed H atom to the TiSe_2 surface, $d_{\text{Se-H}}$; binding energy, E_b ; HSE calculated electronic band gap, E_g ; of CDW phase, single-H adsorbed and fully-hydrogenated TiSe_2 (fH- TiSe_2).

	a (Å)	b (Å)	$d_{\text{Se-H}}$ (Å)	E_b (eV)	E_g (meV)
CDW phase	7.00	7.00	-	-	319
Single-H on TiSe_2	14.08	14.08	1.48	1.69	-
fH- TiSe_2	3.61	6.50	1.53/1.49	2.55	119

3.1.2.3. Full Hydrogenation

Following the analysis of the adsorption of a H atom on CDW phase of TiSe_2 , modifications of structural, electronic, phononic and thermal properties of TiSe_2 upon full hydrogenation are investigated.

Structural and Phononic Properties

To construct a fully covered structure the most favorable position of an isolated H atom is used. Therefore, fully-hydrogenated TiSe_2 , with each H atom resides on top of a Se atom is investigated. It is found that through full hydrogenation, TiSe_2 experiences

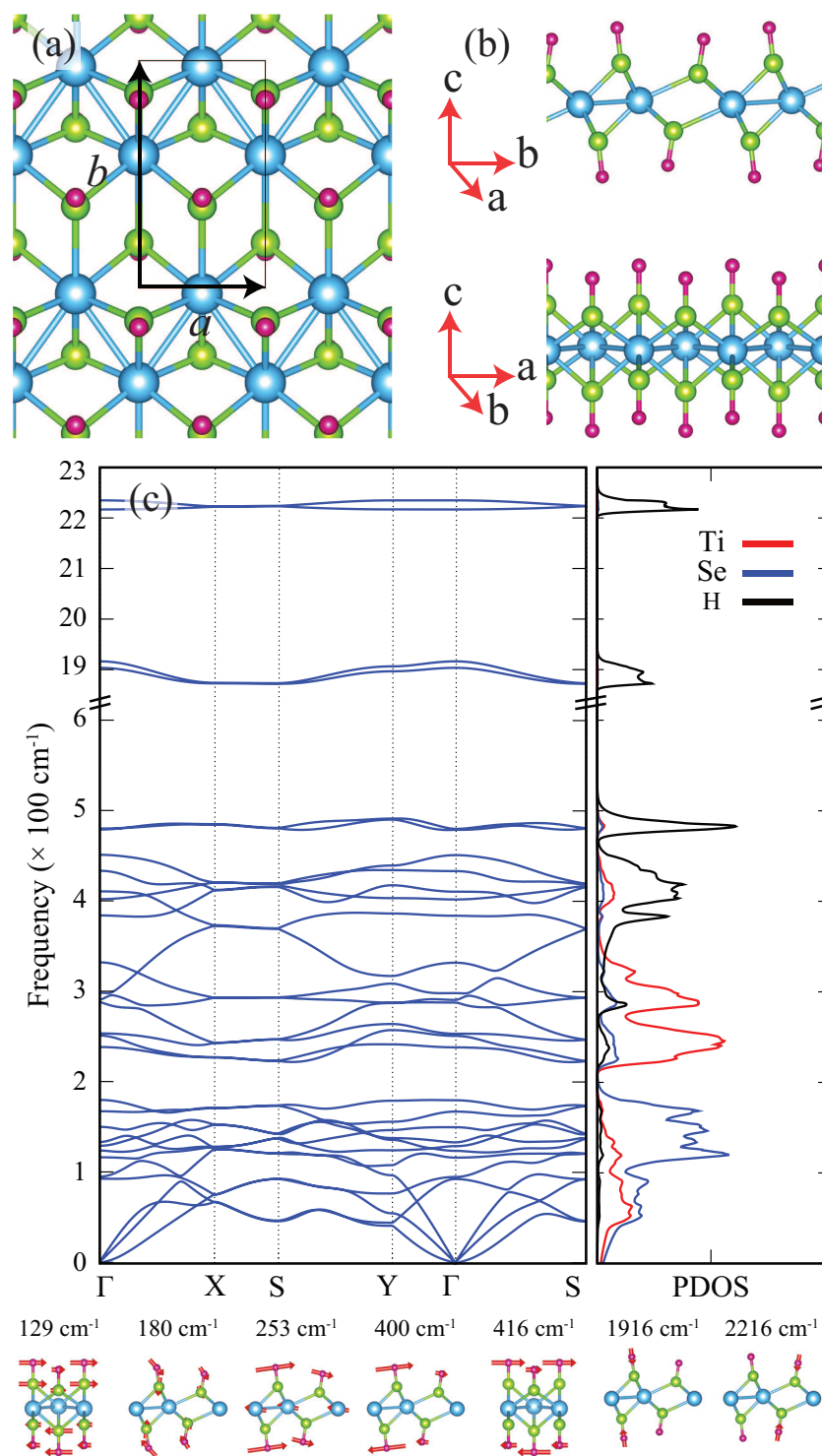


Figure 3.9. (a) Top and (b) side view geometries and (c) phonon band diagram and partial phonon DOS of fH-TiSe₂. The branches of the possible Raman-active modes are shown on the lower panel.

a structural phase transition from CDW phase to T_d phase. Figures 3.9 (a) and (b) show top and side views of the optimized atomic structure of fully-hydrogenated single-layer TiSe_2 (fH- TiSe_2). T_d phase has a rectangular unit cell with calculated lattice constants of $a = 3.61 \text{ \AA}$ and $b = 6.50 \text{ \AA}$. The unit cell of fH- TiSe_2 is composed of two Ti, four Se, and four H atoms. The hydrogenation of each Se atom leads to a reduced interaction between Ti and Se atoms. Therefore, transition metal atoms get closer and form separated zig-zag chains. Ti-Ti bond distance in the zig-zag chain is calculated to be 3.12 \AA . The bond distance between Ti and Se atom is in the range of $2.48\text{-}2.76 \text{ \AA}$. Due to reduced symmetry of the T_d phase, there are two different Se atoms: outer-Se and inner-Se. H atoms reside on top of these Se atoms. The bond length between outer-Se (inner-Se) and H atom is 1.53 (1.49) \AA . The calculated average binding energy of a H atom is 2.55 eV , which is much higher than the binding energy of a H adsorption case.

Phonon dispersion and partial phonon DOS of the fH- TiSe_2 are shown in Figure 3.9 (c). $4 \times 2 \times 1$ supercell is used for the phonon calculations of fH- TiSe_2 . It is found that fully-hydrogenated TiSe_2 has real vibrational eigenfrequencies in the whole Brillouin Zone and hence fH- TiSe_2 is dynamically stable. The unit cell of fH- TiSe_2 consists of 10 atoms, consequently it possesses 30 phonon bands, 3 acoustic and 27 optical. As mentioned above, hydrogenation of TiSe_2 induces a significant structural transition from CDW phase to T_d phase. Comparison between the phonon calculations of pristine and fully-hydrogenated TiSe_2 shows significant differences. Unlike the pristine case, the high-frequency optical modes of fH- TiSe_2 are separated from the low-frequency modes by a gap of 42 cm^{-1} . Full hydrogenation causes to presence of optical phonon branches at quite high frequencies. It is seen from the right panel of Figure 3.9 (c), above 350 cm^{-1} the phonon partial DOS almost entirely consists of vibrations of H atoms.

In Figure 3.9 (c) the atomic displacements of possible Raman active modes are also presented. The low frequency characteristic Raman-active mode at 129 cm^{-1} corresponds to an in-plane (E_g like) a counter-phase motion of top and bottom Se and H layers (parallel to the \vec{a}). The Raman-active mode with frequency of 180 cm^{-1} corresponds to a mixed in-plane and out-of-plane (A_g like) counter-phase motion of top and bottom Se and H layers (parallel to the \vec{b}). However, the character of the phonon mode at 253 cm^{-1} is mostly in-plane and while Se atoms stay fixed, Ti and H atoms move in opposite directions to each other (parallel to the \vec{b}). The phonon modes at 400 and 416 cm^{-1} correspond to in-plane counter-phase motions of top and bottom H layers (parallel to the \vec{b} and \vec{a} , respectively). As can be seen from the Figure 3.9 (c), the high-frequency modes at 1916 and 2216 cm^{-1} are Se-H stretching modes.

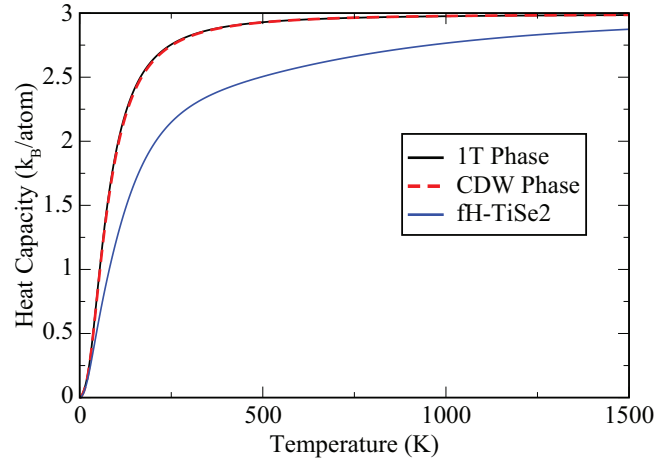


Figure 3.10. Constant-volume heat capacity of single-layer crystal structures of 1T and CDW phases of pristine TiSe_2 and fH- TiSe_2 .

Heat Capacity

The thermal properties of ultra-thin materials can be investigated through the calculation of heat capacity (C_v). It is known that contribution of free conduction electrons to the heat capacity of ultra-thin materials is negligible. Hence, the heat capacity is constituted almost entirely from lattice vibrations of the material.

In this part we discuss the effect of hydrogenation on the heat capacity of TiSe_2 . The heat capacities of 1T, CDW phases and fully-hydrogenated TiSe_2 as a function of temperature are shown in Figure 3.10. Previously, it was shown that hydrogenation of ultra-thin materials leads to an increase in the heat capacity of the materials (Neek-Amal and Peeters, 2011). However, as seen from Figure 3.10, the heat capacity of fully-hydrogenated TiSe_2 is always lower than the heat capacity of 1T and CDW phases of TiSe_2 for all temperatures. Decrease in the heat capacity is attributed to the phonon band gap observed at relatively low frequencies (between $180\text{-}222\text{ cm}^{-1}$). It is known that the heat capacity is closely related with the phonon DOS of the material. Lack of phonon DOS at the phonon band gap lead to decrease in the heat capacity of the material. At room temperature, C_v of 1T and CDW phases are equal to $2.82\text{ k}_B/\text{atom}$, whereas C_v of fH- TiSe_2 is $2.27\text{ k}_B/\text{atom}$. At 1500 K, the heat capacity for 1T and CDW phases of TiSe_2 approach the value of Dulong-Petit law $C_v = 3NR$, where R is the universal gas constant and N is the number of atoms per unit cell. However, the heat capacity for fH- TiSe_2 approaches to this value at higher temperatures. Calculated Debye temperature values of

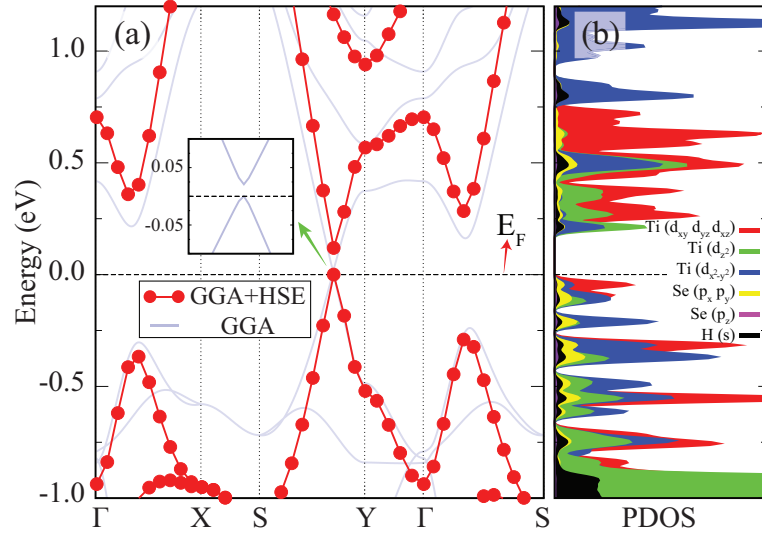


Figure 3.11. (a) The electronic band structure of fH-TiSe₂. Light blue and red-dotted bands are for GGA and GGA+HSE calculated band dispersions, respectively. (Inset: GGA calculated band dispersion near the fermi level.) (b) GGA+HSE calculated PDOS of fH-TiSe₂. The valence band maximum is set to zero.

1T, CDW phases and fH-TiSe₂ are 335, 341, and 1378 K, respectively.

Electronic Properties

The electronic band dispersions and PDOS obtained by using HSE06 functional of fH-TiSe₂ are shown in Figures 3.11 (a) and (b), respectively. It is found that hydrogenation of single-layer TiSe₂ leads to reduction in the energy band gap. Band gap of fully-hydrogenated TiSe₂ is calculated to be 119 meV when HSE06 functional is used (GGA value: 21 meV). Although TiSe₂ conserves its direct gap semiconducting behavior with hydrogenation, both VBM and CBM transfer to different wavevector point within Y and S from Γ point, where VBM and CBM of pristine TiSe₂ reside.

Calculated PDOS shows that the states in the VBM are mainly made up of the t_{2g} orbitals of Ti atom, whereas the states in the CBM have d_{z^2} and $d_{x^2-y^2}$ orbitals of Ti atom. It is clearly seen from Figure 3.11 (b), near the Fermi level the contribution from t_{2g} orbital of Ti atom is increased by hydrogenation, while p orbital contribution of Se atom is decreased. Compared to the pristine case, decreased overlap of PDOS peak positions and shapes of t_{2g} orbitals of Ti atom and p orbitals of Se atom exhibit weak coupling of these orbitals through hydrogenation. This weak coupling can be attributed

to the weakening of the bonds between the Ti and Se atoms due to the binding of H atoms to each Se atom. Therefore, Ti atoms are released, they move toward to each other. This leads to a structural phase transition from the CDW phase to the T_d phase.

3.1.2.4. Conclusions

In summary, the structural, phononic, thermal, and electronic properties of pristine and hydrogenated single-layer TiSe_2 were investigated within first-principles DFT calculations. It was found that the periodic lattice distortions in the CDW phase provide the stability of the layer. Our calculations showed that experimentally fabricated low temperature phase (CDW phase) of TiSe_2 has an HSE06-calculated direct band gap of 319 meV.

In addition, adsorption of one H atom on the CDW phase of TiSe_2 was investigated. Preferred adsorption site, binding energy and electronic properties of single-H adsorbed CDW phase of TiSe_2 were determined. Moreover, our calculations revealed a structural transition resulting from the rearrangement of the Ti atoms after full hydrogenation of single-layer TiSe_2 . The fully-hydrogenated TiSe_2 prefers T_d phase which exhibits Ti-Ti dimerization along one of the lattice parameters. Structural stability of the fully-hydrogenated TiSe_2 was confirmed by calculated phonon spectra of the layer. Direct electronic band gap of the material decreased to 119 meV upon full hydrogenation. Furthermore, it was found that full hydrogenation of TiSe_2 leads to a dramatic decrease in the heat capacity. Single-layer TiSe_2 with robust semiconducting character, sensitive thermal properties, and hydrogenation-induced structural transition is highly desired material for nanoscale device applications.

3.2. Thinning of Two-Dimensional Materials

In this section, we investigate the effect of dimensional crossover on the characteristic properties of CsPb_2Br_5 and PtSe_2 crystals.

3.2.1. Thinning CsPb₂Br₅ Perovskite Down to Monolayers

In recent years, hybrid organic-inorganic lead halide perovskites have attracted immense interest because of their low cost, easy fabrication and superior optoelectronic properties (Grätzel, 2014; Tan *et al.*, 2014). These hybrid perovskites exhibit great potential in device applications such as photodetectors (Dou *et al.*, 2014), laser devices (Zhu *et al.*, 2015), flexible solar cells (Yang *et al.*, 2015), and light emitting diodes (LEDs) (Kim *et al.*, 2015; Xing *et al.*, 2016)). One of the most studied organic-inorganic hybrid perovskite is CH₃NH₃PbX₃ (where X = Cl, Br, or I). Noh *et al.* showed that the band gap of CH₃NH₃Pb(I_{1-X}Br_X) can be controlled by composition engineering and the absorption edge of the mixed halide perovskite can be altered in a controlled manner to cover almost the whole visible spectrum (Noh *et al.*, 2013). It was also demonstrated that organic-inorganic hybrid perovskites exhibit high power conversion efficiency of exceeding 20% (Ergen *et al.*, 2017; Jeon *et al.*, 2015)). The fully inorganic CsPbX₃ (X = Cl, Br, or I) exhibits higher chemical stability and excellent optoelectronic properties compared to organic-inorganic perovskites (Protesescu *et al.*, 2015; Kulbak *et al.*, 2015; Wang *et al.*, 2015). It was found that these all-inorganic materials exhibit extremely high fluorescence quantum yield, very narrow emission bandwidth, and suppressed fluorescence blinking (Swarnkar *et al.*, 2015; Li *et al.*, 2016)). It was shown that CsPbBr₃ exhibits high carrier mobility and large diffusion length (Yettapu *et al.*, 2016). It has been theoretically predicted that CsPbBr₃ is highly defect-tolerant in terms of its electronic structure (Kang and Wang, 2017).

The rapid progress in the synthesis and fabrication methods of 2D materials has not only led to exploration of graphene-like materials but also monolayer 2D hybrid perovskites. It was reported that thickness and photoluminescence emission of hybrid perovskite nanoplatelets can be controlled by varying the ratio of the organic cations used (Sichert *et al.*, 2015). Recently, atomically thin organic-inorganic hybrid perovskite synthesized with efficient photoluminescence and modulation of color have been achieved by tuning the thickness and composition of the crystal (Dou *et al.*, 2015). The synthesis of layered CH₃NH₃PbX₃ (where X = Cl, Br, or I) down to a thickness of a few unit cell and even single unit cell layers were accomplished by a combined solution process and vapor-phase conversion method (Liu *et al.*, 2016). It was found that by controlling atomic ratio of the halide anions, stability of the hybrid perovskites can be improved (Noh *et al.*, 2013). Compared to organic-inorganic hybrid perovskites, all-inorganic perovskites, in which cesium ions replace organic cations, exhibit higher chemical stability

(Kulbak *et al.*, 2015; Song *et al.*, 2015)). However, low environmental stability of hybrid organic-inorganic perovskites is a crucial issue that needs to be addressed for potential future applications.

Moreover, all-inorganic CsPb_2Br_5 emerged as a 2D version of lead halide perovskite materials. CsPb_2Br_5 has a tetragonal phase which consists of alternating Cs^+ and $[\text{Pb}_2\text{Br}_5]^-$ polyhedron layers. Theoretical and experimental investigations showed that CsPb_2Br_5 is an indirect band gap semiconductor with a band gap of 2.98 eV (Li *et al.*, 2016). Large-scale synthesis of highly luminescent CsPb_2Br_5 nanoplatelets was already reported (Wang *et al.*, 2016). It was found that a dual phase of CsPbBr_3 - CsPb_2Br_5 exhibits increased conductivity and improved emission life time compare to that of the pure CsPbBr_3 (Zhang *et al.*, 2016). However, thickness and composition dependent structural stability and electronic properties of CsPb_2Br_5 remain almost unexplored. It is known that ultrathin 2D materials are more sensitive to environmental conditions than their bulk counterpart. Environmental conditions and substrate can affect the structural stability and characteristic properties of ultrathin 2D materials. It was reported that in the presence of chlorine, when $\text{CH}_3\text{NH}_3\text{PbI}_3$ films are deposited on a TiO_2 mesoporous layer, a stable cubic phase is formed in $\text{CH}_3\text{NH}_3\text{PbI}_3$ perovskite, instead of the commonly observed tetragonal phase (Wang *et al.*, 2015). In a recent study CsPb_2Br_5 nanosheets were obtained via an oriented attachment of CsPbBr_3 nanocubes (Li *et al.*, 2016). It was also reported that inorganic Cs atom plays a significant role in the stability of perovskites (Zhang *et al.*, 2017; Saliba *et al.*, 2016). The Cs atom as a cation, donates charge to the lattice of a perovskite and fulfill the charge neutrality.

Although the bulk forms of many perovskites have been studied intensely, effect of dimensional reduction in the characteristic properties of CsPb_2Br_5 crystal has not been investigated before. In the current study, using first principles calculations based on density functional theory (DFT), we present a detailed analysis of the structural, electronic, vibrational and vacancy-dependent characteristics of single-layer CsPb_2Br_5 .

3.2.1.1. Bulk CsPb_2Br_5

Before a detailed discussion of the potential single-layer forms of CsPb_2Br_5 , we first investigate structural properties of bulk form of the crystal. The tetragonal phase of CsPb_2Br_5 is shown in Fig 3.12 (a). CsPb_2Br_5 consists of sandwiched structure with alternating Cs and Pb-Br polyhedron layers. The calculated lattice parameters are $a = 8.24 \text{ \AA}$ and $c = 14.57 \text{ \AA}$. Tilted side and top views of Pb-Br polyhedron layer are shown in

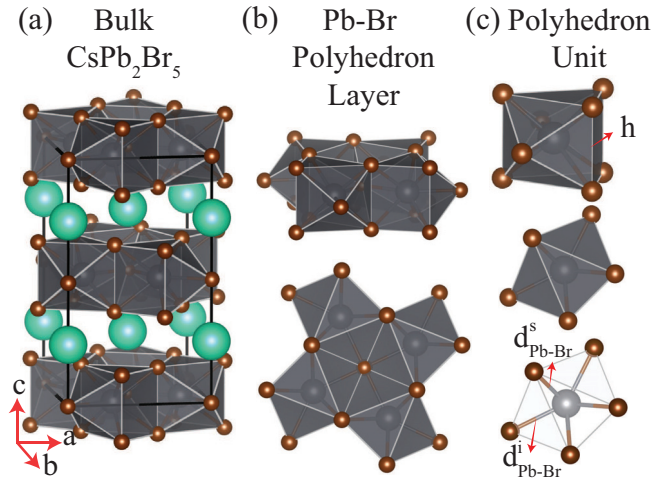


Figure 3.12. (a) Tilted side view of bulk CsPb_2Br_5 . (b) Tilted side and top views of Pb-Br polyhedron layer. (c) Tilted side and top views of Pb-Br polyhedron. Green, brown, and gray balls illustrate Cs, Br, and Pb atoms, respectively.

Fig 3.12 (b). Pb-Br polyhedron layer is composed of Pb-Br polyhedrons which are formed by putting a triangular prism and two rectangular pyramids together. Tilted side and top views of Pb-Br polyhedron are shown Fig 3.12 (c). There are two different bromine atoms in the polyhedron: one of them is located at the surface of Pb-Br polyhedron layer (Br_s) and the other one is located at the inner plane of the layer (Br_i). Br_i is located in the same plane with Pb atoms and it has the Pb-Br bond distance of $d_{\text{Pb-Br}}^i = 3.08 \text{ \AA}$. The bond length between Br_s and Pb atoms is $d_{\text{Pb-Br}}^s = 2.92 \text{ \AA}$. The thickness of Pb-Br polyhedron layer is $h = 3.83 \text{ \AA}$. The distance between Cs and surface Br atoms is $d_{\text{Cs-Br}}^s = 3.53 \text{ \AA}$. It is found that the cohesive energy per atom of CsPb_2Br_5 crystal is 3.42 eV.

For detailed investigation of the bondings in CsPb_2Br_5 crystal Bader charge analysis is also performed. It is found that 0.8 and 1.0 e charges are donated by each Cs and Pb atoms, respectively. On the other hand, each Br atom receives 0.6 e charge. Therefore, analysis of the electronic structure reveals that ionic interaction arises between the layers of Cs and Pb-Br skeleton via vertical charge transport from Cs layer to the Pb-Br skeleton. Furthermore, the bond between Pb and Br atoms in the Pb-Br skeleton has also an ionic character. Cs terminated surface of CsPb_2Br_5 crystal has a low work function of $\Phi = 1.17 \text{ eV}$.

Figure 3.13 shows the band structure and projected density of states (PDOS) for CsPb_2Br_5 crystal. It can clearly be seen from the figure, that bulk CsPb_2Br_5 exhibits an indirect band gap, with the valence band maximum (VBM) residing along the line Γ -

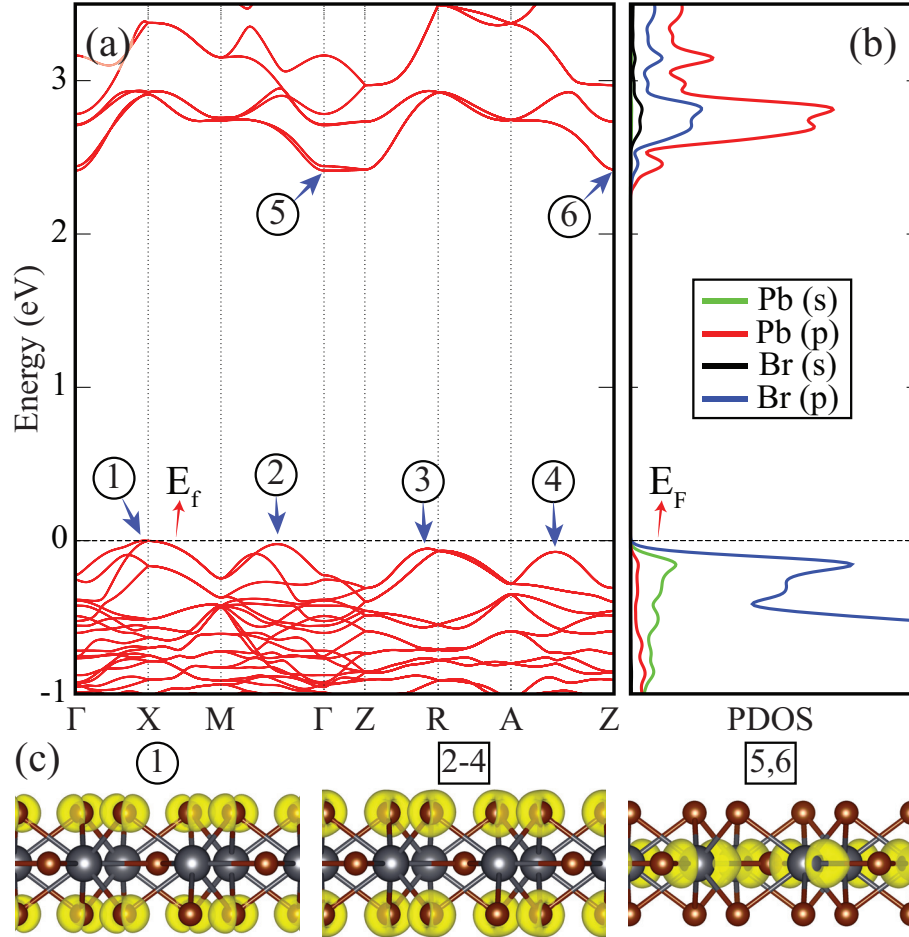


Figure 3.13. (a) The energy-band dispersion and (b) partial density of states of bulk CsPb_2Br_5 . (c) The band decomposed charge densities of the bulk CsPb_2Br_5 at the labeled band edges. Isosurface value of charge density is $2 \times 10^{-5} e/\text{\AA}^3$.

X (①), while the conduction band minimum (CBM) being located at the Γ point (⑤). The indirect gap calculated with LDA+SOC is 2.41 eV. It is known that experimentally observed band gaps, which are underestimated by both bare-LDA and bare-GGA functionals, can be well-approximated by the considering screening (GW calculations) and excitonic (solving Bethe-Salpeter equation) effects. However, due to high computational cost, GW and BSE calculations are not taken into account here. The partial contributions of orbital states to electronic DOS of bulk CsPb_2Br_5 crystal are given in the Figure 3.13 (b). It appears that the major contribution to the states around the band edges originates from Pb and Br atoms. While the VBM is dominated by p orbitals of Br atom, the CBM is mostly composed of the p orbitals of Pb atom. The states of the Cs atom reside at deep energy levels, therefore, they have no effect on the electronic structure of the crystal. Band-decomposed charge densities of the valence and conduction band edges are also given in the Figure 3.13. As seen in the figure, edges in the top of valence band are composed of the p_x and p_y orbitals of Br_s atoms. Valance band edges in between Γ and M (②), Z and R (③), A and Z (④) points differ by 23, 53 and 74 meV energy than the VBM of the single-layer, respectively. On the other hand, top of conduction band edges (⑤ and ⑥) are mostly made up of p_x and p_y orbitals of Pb atom.

3.2.1.2. Thinning CsPb_2Br_5 down to Monolayers

Five reasonable single-layer configurations derived from bulk CsPb_2Br_5 structure are shown in Figure 3.14. According to their chemical compositions, these five structures are named as Pb_2Br_5 , $\text{CsPb}_4\text{Br}_{10}$, single-side Cs terminated CsPb_2Br_5 (*ss*- CsPb_2Br_5), double-side Cs terminated CsPb_2Br_5 (*ds*- CsPb_2Br_5) and $\text{Cs}_2\text{Pb}_2\text{Br}_5$. Depending on whether the synthesis technique is growth or mechanical exfoliation process one of these of the single layer crystal structures or their mixtures can be obtained.

Single-layer Pb_2Br_5 is a Cs-free skeleton composed of only Pb-Br polyhedrons. As given in Table 3.3, the calculated lattice parameter and thickness of Pb_2Br_5 are $a = 8.09 \text{ \AA}$ and $h = 3.72 \text{ \AA}$, respectively. These values are relatively small compared to those of bulk. The calculated bond lengths between the atoms of the structure are given in the Table 3.3. To assess the dynamical stability, phonon dispersions of single-layer Pb_2Br_5 are calculated and shown in Figure 3.14 (a). A $3 \times 3 \times 1$ supercell is used for the phonon band structure calculations of single-layer forms of the crystal. The phonon spectra of the structure exhibit imaginary eigenvalues through all the symmetry points, indicating the instability of the structure. Instability in the structure could be attributed to the charge

Table 3.3. The calculated ground state properties for bulk (**b**) CsPb₂Br₅ and single-layer Pb₂Br₅, CsPb₄Br₁₀, *ss*-CsPb₂Br₅, *ds*-CsPb₂Br₅, and Cs₂Pb₂Br₅: The lattice constants in the lateral and vertical directions, a and c , respectively; thickness of the Pb-Br polyhedron layer, h ; atomic distances between Pb and Br atoms, d_{Pb-Br}^i and d_{Pb-Br}^s ; atomic distance between Cs and surface Br atoms, d_{Cs-Br}^s ; the cohesive energies, E_{coh} ; the energy band gap of the structure, Gap; the work function, Φ .

	a (Å)	c (Å)	h (Å)	d_{Pb-Br}^i (Å)	d_{Pb-Br}^s (Å)	d_{Cs-Br}^s (Å)	E_{coh} (eV)	Gap (eV)	Φ (eV)
b CsPb ₂ Br ₅	8.24	14.57	3.83	3.08	2.92	3.53	3.42	2.41	1.17
Pb ₂ Br ₅	8.09	-	3.72	3.02	2.88	-	3.08	-	7.00
CsPb ₄ Br ₁₀	8.18	-	3.77	3.05, 3.08	2.94	3.44	3.21	-	4.53
<i>ss</i> -CsPb ₂ Br ₅	8.29	-	3.85	3.11	2.84	3.42	3.31	2.53	2.75
<i>ds</i> -CsPb ₂ Br ₅	8.29	-	3.81	3.11	2.92	3.43	3.32	2.54	4.79
Cs ₂ Pb ₂ Br ₅	8.21	-	4.31	3.18	3.22	3.35	3.15	-	1.45

transfer mechanism between ions of the structure. Bader charge analysis reveals that resulting charges of Br atoms of Pb₂Br₅ are lower than that of bulk CsPb₂Br₅. Although each Pb atom donates 1.0 e charge, each Br _{i} and Br _{s} atoms receive 0.5 and 0.4 e charges, respectively. Therefore, unsaturated Br _{i} and Br _{s} atoms may lead to dynamical instability in single-layer Pb₂Br₅.

For a deeper analysis of instability of single-layer Pb₂Br₅, atomic displacements of the lowest mode are shown in the inset of phonon band diagram of Figure 3.14 (a). It appears that the mode responsible for the instability of the structure is due to vibrations of Br _{i} and Br _{s} atoms normal and parallel to the plane of the structure, respectively. Imaginary eigenfrequencies in the whole Brillouin Zone indicate the lack of required restoring force against these atomic motions. Therefore, the structure is unstable under this motion and transforms to another phase. This instability can be cured by increasing the bond strength between Pb and Br atoms through adding an extra charges. As shown in the Figure 3.14 (b), single-layer of CsPb₄Br₁₀ is formed through half of the single-side of Pb-Br layer covered by Cs atoms. The lattice parameter and the thickness of the structure are $a = 8.18$ Å and $h = 3.77$ Å, respectively. It is found that the single-layer CsPb₄Br₁₀ is formed by a cohesive energy of 3.21 eV. Since one side of the structure is covered by Cs atoms, the bonds show anisotropy in the vertical direction (see Table 3.3). Given values of the bond lengths belong to Cs terminated side of the structure. The phonon spectra of single-layer CsPb₄Br₁₀ exhibit real eigenvalues through all the symmetry points, confirming the dynamical stability of the layers. Bader charge analysis shows that Cs and Pb

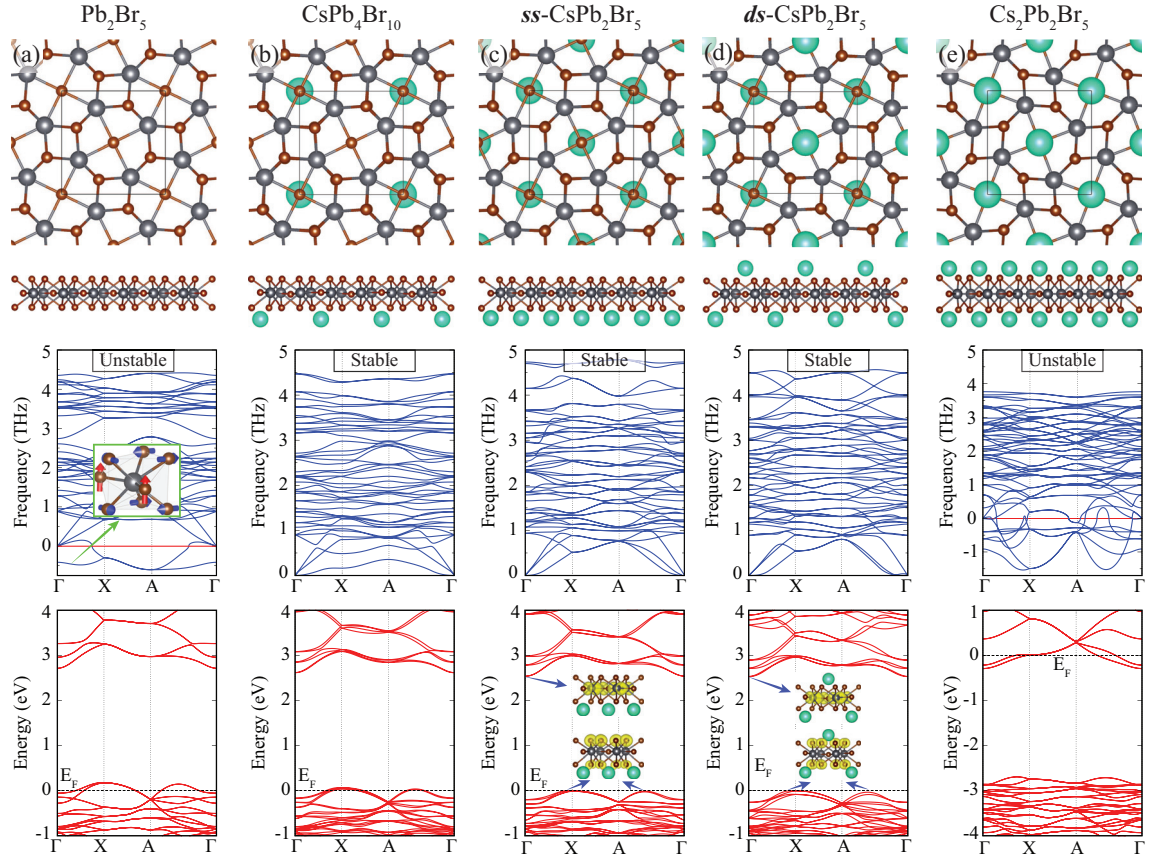


Figure 3.14. Possible single-layer structures of CsPb_2Br_5 crystal. Top and side views of the structures, phonon spectrum, and SOC included electronic band diagrams of single-layer (a) Pb_2Br_5 , (Inset: Tilted side view of atomic displacements of the corresponding mode.) (b) $\text{CsPb}_4\text{Br}_{10}$, (c) $ss\text{-CsPb}_2\text{Br}_5$, (d) $ds\text{-CsPb}_2\text{Br}_5$, and (e) $\text{Cs}_2\text{Pb}_2\text{Br}_5$. Isosurface value of band decomposed charge densities (inset of band structure of $ss\text{-CsPb}_2\text{Br}_5$) is $2 \times 10^{-5} e/\text{\AA}^3$.

atoms of the structure donate 0.8 and 1.0 e charges, respectively. Therefore the amount of received charges by each Br atom is 0.5 e . The work function of the structure is calculated to be 4.53 eV. It is also seen from the Figure 3.14 (b) that lowering the concentration of Cs atoms leads to unfilling of the valence band edge and therefore p-type conductivity in the single-layer CsPb₄Br₁₀.

Relaxed geometric structures of *ss*-CsPb₂Br₅ and *ds*-CsPb₂Br₅ are shown in Figures 3.14 (c) and (d), respectively. These two structures possess the same chemical composition with the CsPb₂Br₅ crystal. The lattice parameters of both of the structures are $a = 8.29$ Å. The thickness of the Pb₂Br₅ sublayer of *ss*-CsPb₂Br₅ and *ds*-CsPb₂Br₅ are $h = 3.85$ and 3.81 Å, respectively. As given in the Table 3.3, the atom-atom bond distances of these two structures are very similar to that of the bulk CsPb₂Br₅. Real frequencies in the phonon spectra of single-layer structures (Figures 3.14 (c) and (d)) of *ss*-CsPb₂Br₅ and *ds*-CsPb₂Br₅ appear in a whole Brillouin Zone, indicating the dynamical stabilities of these two structures. Bader charge analysis reveals that the charge transfer mechanism of single-layers of *ss*-CsPb₂Br₅ and *ds*-CsPb₂Br₅ are very similar to the bulk CsPb₂Br₅. Cs and Pb atoms of the both structures donate 0.8 and 1.0 e charges, respectively. The amount of charge received by Br atoms of the two structures are in the range of 0.5-0.6 e . Therefore, Pb-Br skeletons of the two structures are saturated with enough charges to maintain stable bonding mechanism. In addition, cohesive energies of these two structures are given in Table 3.3. Among the single-layer forms of the crystal, due to the vertical symmetry and the same chemical composition with the bulk counterpart, *ds*-CsPb₂Br₅ has the highest cohesive energy. Furthermore, calculated work function values of single-layers of *ss*-CsPb₂Br₅ and *ds*-CsPb₂Br₅ are 2.75 and 4.79 eV, respectively. Calculated values of the work functions belong to Cs-terminated side of the structure. Hence, the work function shows a decreasing behavior with increasing concentration of Cs atoms of Cs-terminated side.

As shown in Figures 3.14 (c) and (d), single-layer *ss*-CsPb₂Br₅ and *ds*-CsPb₂Br₅ have very similar electronic band diagrams and they are indirect band gap semiconductors. The VBMs of the two structures reside at X point, whereas their CBMs reside at Γ point. It is worth mentioning that valence band edge in between A and Γ points differs only by 24 meV energy from the VBM of the two structure. Band decomposed charge densities at the valence band and the conduction band edges of the two structures are shown in Figures 3.14 (c) and (d). Band edge characteristics of these structures possess very similar behavior with their bulk counterpart. As given in Table 3.3, the SOC included band gap of *ss*-CsPb₂Br₅ and *ds*-CsPb₂Br₅ are 2.53 and 2.54 eV therefore with decreasing thickness

from bulk to single-layer, the band gap of CsPb_2Br_5 increases by ~ 0.13 eV.

The single-layer $\text{Cs}_2\text{Pb}_2\text{Br}_5$ is constructed by three submonolayers: a Pb_2Br_5 sublayer and two surrounding sublayers of Cs atoms. The calculated lattice parameter of $\text{Cs}_2\text{Pb}_2\text{Br}_5$, $a = 8.21$ Å is very similar to bulk lattice parameter of the crystal. However, the thickness of Pb_2Br_5 sublayer is $h = 4.31$ Å, which is much higher than that of the other single-layer forms of the crystal. As in Pb_2Br_5 , phonon spectra of single-layer $\text{Cs}_2\text{Pb}_2\text{Br}_5$, shown in Figure 3.14 (e), exhibit imaginary eigenvalues through whole the symmetry points, indicating the dynamical instability of the structure. In single-layer $\text{Cs}_2\text{Pb}_2\text{Br}_5$, while each Cs and Pb atom donate $0.8 e$ charges, each Br_i and Br_s atoms receive 0.6 and $0.7 e$ charges, respectively. Extra charges provided by Cs atoms lead to a decrease in charge transfer between Pb and Br atoms. Therefore, the Cs-induced weakening of the Pb-Br bonds is the reason of the instability in the single-layer $\text{Cs}_2\text{Pb}_2\text{Br}_5$.

3.2.1.3. Effect of Cs Atoms via The Charging of Pb_2Br_5 Skeleton

In this chapter, in order to facilitate a deeper understanding of the role of Cs atoms, we examine the stability of Cs-free Pb_2Br_5 , which is already presented to be unstable in the previous chapter, via charging calculations.

One low-lying optical and one acoustic phonon branches that have imaginary eigenfrequencies are the direct indication of dynamical instability in the single layer structure of Cs-free Pb_2Br_5 . However, as calculated in the previous chapter, single layer skeleton structure of Pb_2Br_5 can be stabilized through the adsorption of Cs atoms. Therefore, the question arises as to whether or not the stability of CsPb_2Br_5 is provided only by the charge transferred from Cs atoms to Pb_2Br_5 skeleton.

As shown in Figure 3.15, the role of electron transfer on the stability of Pb_2Br_5 can be examined through the addition of extra electrons into the primitive unit cell. Here, it is important to note that once the unit cell is charged by extra electrons, structure is re-optimized by considering the new charge distribution and phonon calculations are performed for this fully-relaxed structure. Figure 3.15 shows that one acoustic and one low-lying optical branches, having imaginary eigenfrequencies, of the Pb_2Br_5 skeleton can be fixed upon the charging. It appears that while the structure is fully stabilized under $1.4 e$ charging, it exhibits instability under over-charged and less-charged situations. Therefore, it can be concluded that Cs atoms play an important role as stabilizer of the Pb_2Br_5 skeleton by charge transfer. Such a charge dependent stability may pave the way to synthesize novel Cs-free perovskite structures and to fix the vacancy-dependent instabilities

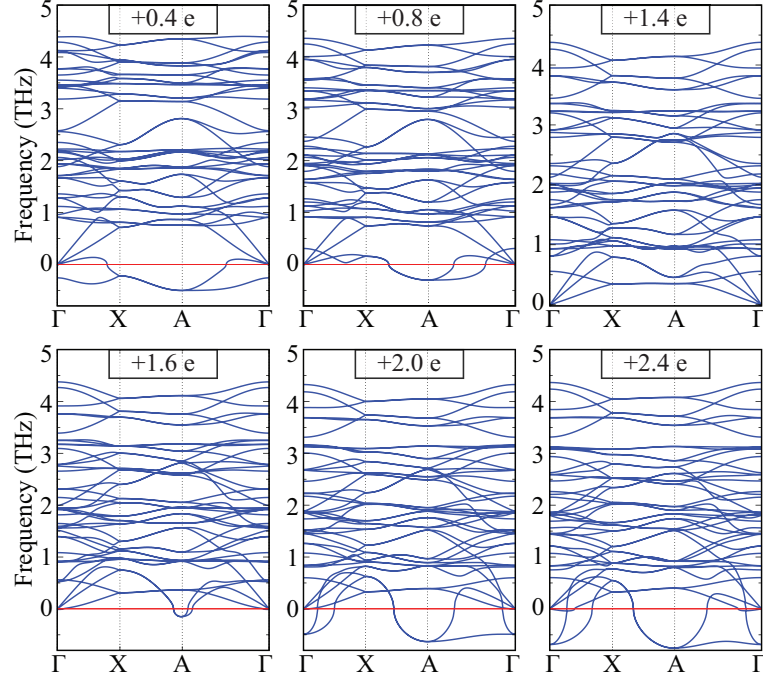


Figure 3.15. Charging-dependent phonon dispersion of single layer skeleton structure of Pb_2Br_5

in similar structures.

3.2.1.4. Vacancy Defects in Single-Layer CsPb_2Br_5

During the growth or exfoliation of layered crystals, existence of various lattice imperfections is inevitable. One of the most common lattice imperfection in layered crystals is vacancies. The formation of vacancies in ionically bonded materials are the source of trap states and profoundly alter the electronic and optical properties of semiconductors. Therefore, it is important to investigate how vacancies are formed and what are the characteristic features. In this section, four different vacancy types in single-layer *ds*- CsPb_2Br_5 that corresponds to the energetically the most favorable structure are considered, Cs vacancy (V_{Cs}), Br_i vacancy (V_{Br_i}), Br_s vacancy (V_{Br_s}), and Pb vacancy (V_{Pb}). In order to hinder the interaction between vacancies in adjacent cells, a 64-atom supercell was used. Relative stabilities of the four vacancies are calculated according to the formula:

$$E_{\text{form}} = E_{\text{SL}+\text{vac}} + E_{\text{A}} - E_{\text{SL}} \quad (3.2)$$

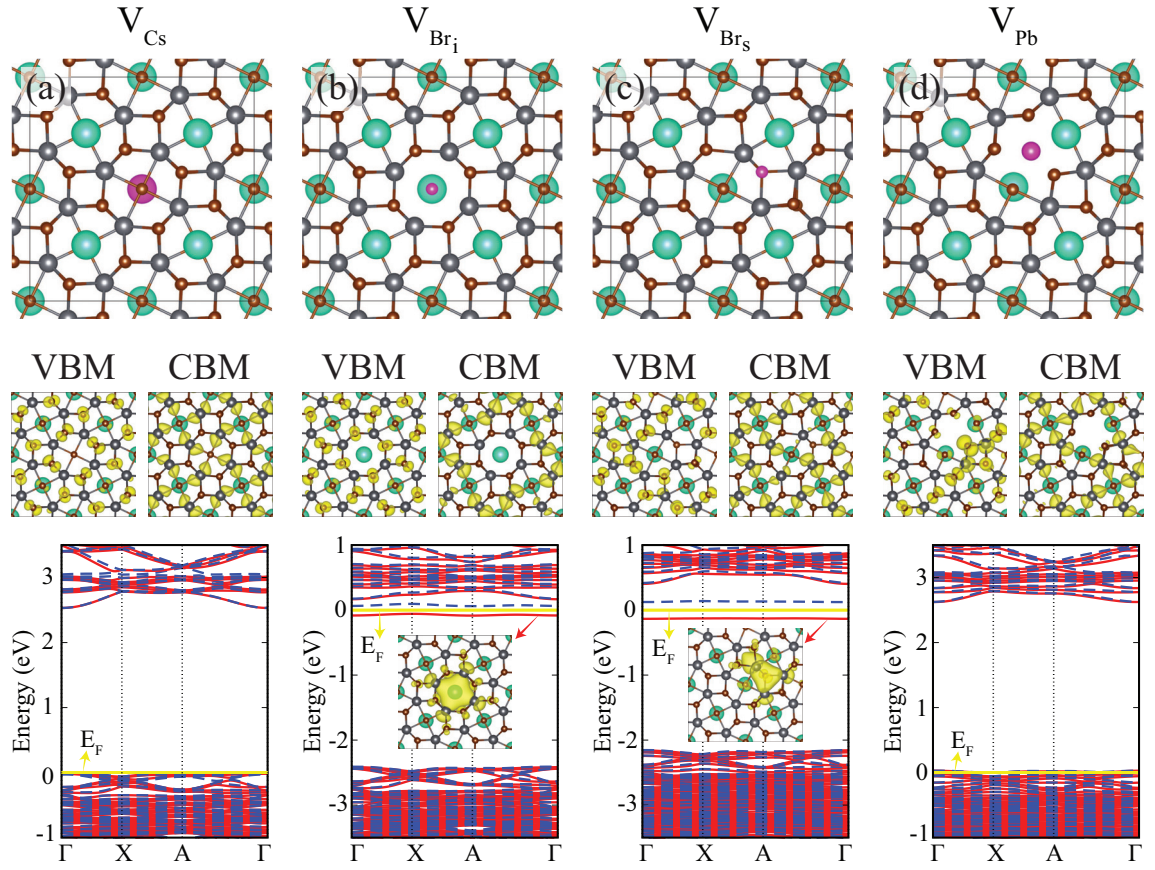


Figure 3.16. Top view of the structures, band decomposed charge densities of the VBM and CBM, and electronic band structures of single-layer *ds*-CsPb₂Br₅ with (a) Cs vacancy, (b) Br_{*i*} vacancy, (c) Br_{*s*} vacancy, and (d) Pb vacancy. Pink atoms illustrate removed atoms. Yellow, red, and dashed blue lines in band diagrams illustrate the Fermi level, majority, and minority spin bands, respectively. Band decomposed charge densities of in-gap states of V_{Br_{*i*}} and V_{Br_{*s*}} are shown in the insets of the corresponding band diagrams. Isosurface value of charge density is $6 \times 10^{-6} e/\text{\AA}^3$.

where E_{form} is the formation energy of the relevant vacancy, E_{SL+vac} is the total energy of the supercell with vacancy, E_A is the isolated-single-atom energy of the removed atom and E_{SL} is the total energy of supercell of single layer.

Table 3.4. The lattice constants, a ; formation energies, E_{form} ; magnetic moments, M ; electronic characteristics, and band gaps of four different defected forms of $2 \times 2 \times 1$ supercell of the single-layer $CsPb_2Br_5$.

	a (Å)	E_{form} (eV)	M (μ_B)	Electronic Characteristic	Band Gap (eV)
V_{Cs}	16.48	4.82	0.0	semiconductor	2.53
V_{Br_i}	16.44	5.02	1.0	semiconductor	0.12
V_{Br_s}	16.48	4.51	1.0	semiconductor	0.25
V_{Pb}	16.46	8.20	0.0	metal	-

Relaxed geometric structures when a single Cs, Br_i , Br_s and Pb are created in the ds - $CsPb_2Br_5$ are shown in Figures 3.16 (a)-(d), respectively. Formation of these vacancies leads to negligible distortion on the single-layer ds - $CsPb_2Br_5$. As given in the Table 3.4 fully relaxed lattice parameters of V_{Cs} , V_{Br_i} , V_{Br_s} and V_{Pb} are 16.48, 16.44, 16.48 and 16.46 Å, respectively. The formation of Pb vacancy (V_{Pb}) leads to minor local reconstructions. When Pb vacancy is introduced, the closest Br atoms to the extracted Pb atom are released and they move toward the neighboring Pb atoms. The formation energies of V_{Cs} , V_{Br_i} , V_{Br_s} and V_{Pb} are calculated to be 4.82, 5.02, 4.51 and 8.20 eV, respectively. Therefore, one can conclude that formation of Cs and Br vacancies in single-layer ds - $CsPb_2Br_5$ perovskite are more likely.

The electronic band structures of ds - $CsPb_2Br_5$ with V_{Cs} , V_{Br_i} , V_{Br_s} and V_{Pb} are presented in Figures 3.16 (a)-(d), respectively. It appears that electronic properties of single-layer ds - $CsPb_2Br_5$ do not change significantly with the removal of Cs atom. Band decomposed charge densities at the valence band and conduction band edges of V_{Cs} show similar behavior with that of pristine ds - $CsPb_2Br_5$. Figures 3.16 (b) and (c) display band decomposed charge densities and electronic band diagrams of V_{Br_i} and V_{Br_s} . It is seen that only the formation of Br vacancies leads to presence of in-gap states. Such dispersionless electronic states can be attributed to the unpaired electrons of neighboring Pb and Br atoms. For V_{Br_i} and V_{Br_s} vacancies, two spin-polarized in-gap states are symmetrically placed around the Fermi level with band gaps of 0.12 and 0.25 eV, respectively, which then describe a singly occupied in-gap state with a magnetic moment of 1 μ_B . Figure 3.16 (d) shows that when formation of Pb vacancy is created, some states of ds -

CsPb₂Br₅ discharge due to the lack of donor electrons of Pb atom. As a result, formation of Pb vacancy leads to p-type conductivity in single-layer *ds*-CsPb₂Br₅.

3.2.1.5. Conclusions

In conclusion, using first-principle calculations, we investigated the structural, electronic and vibrational properties of CsPb₂Br₅ crystal, and how these properties are affected by dimensional crossover. Bulk CsPb₂Br₅ is an indirect band gap semiconductor with a band gap of 2.41 (LDA+SOC) eV. It was calculated that while the valence and conduction band edges of bulk CsPb₂Br₅ crystal are mainly composed of Pb and Br atoms, Cs atoms do not play role in electronic properties.

Then, we predicted that there are two dynamically stable phases of single layer CsPb₂Br₅. These two structures were found to be stable in both total energy optimization and phonon calculations. Single-layer structures of CsPb₂Br₅ display indirect semiconducting character with a band gap of ~ 2.54 eV within LDA+SOC. Moreover, we showed that stability of single layer CsPb₂Br₅ structures strongly depend on the concentration of Cs atoms. As supported by charging-dependent phonon dispersion calculations, Cs atoms provide stability by 0.8 *e* per atom charge transfer from Cs atoms to the Pb₂Br₅ skeleton.

In addition, formation characteristics, electronic structure, and magnetic ground state of four different vacancy types in single-layer CsPb₂Br₅ were investigated. It was seen that the formation of Br vacancy is the most likely one and it leads to emergence of localized in-gap states. Moreover, single-layer *ds*-CsPb₂Br₅ has a ferromagnetic ground state upon the formation of Br vacancies. On the other hand, p-type doping occurs in semiconducting single-layer CsPb₂Br₅ when Pb and Cs vacancies are formed.

3.2.2. Structural and Electronic Properties of PtSe₂: from Monolayer to Bulk

Among TMDs, apart from well-known Mo and W dichalcogenides, lamellar crystals of Pt dichalcogenides have also attracted interest due to their semi-metallic electronic structure (Guo and Liang, 1986; Kliche, 1985), high optoelectronic performance (Yeo *et al.*, 2002), and enhanced photocatalytic activities (Ullah *et al.*, 2014; Ye and Oh, 2016). Besides their bulk form, 2D Pt dichalcogenides suggest promising materials for nanoelectronic device applications due to their intriguing electronic properties such as transition

from metal to semiconductor (Wang *et al.*, 2015; Zhao *et al.*, 2016; Du *et al.*, 2018). It was shown that few-layer PtS₂ phototransistor exhibits a very high responsivity reaching $1.56 \times 10^3 \text{ A W}^{-1}$ (Li *et al.*, 2017). In addition, Zhao *et al.* reported that few-layer PtSe₂ field effect transistor (FET) exhibits high electron mobility at room-temperature ($\approx 210 \text{ cm}^2 \text{ V}^{-1} \text{ s}^{-1}$) on SiO₂/Si substrate (Zhao *et al.*, 2017). Chia *et al.* investigated the correlation between varying chalcogen type to the electrochemical and catalytic performances of Pt dichalcogenides (Chia *et al.*, 2016). Very recently, it was revealed that vertically aligned PtSe₂/GaAs heterojunction shows broad sensitivity to illumination ranging from deep ultraviolet (UV) to near-infrared (NIR) light (Zeng *et al.*, 2018). Similarly it was shown that multilayer PtSe₂/FA_{0.85}Cs_{0.15}PbI₃ perovskite heterojunction photodetectors are ultra-fast, self-driven and air-stable and also exhibited high sensitivity to illumination range from the UV to NIR spectrum region (Zhang *et al.*, 2018). Sajjad *et al.* demonstrated that monolayer 1T-PtSe₂ is a good candidate for gas sensor applications due to high adsorption energy and robust character of the band edges of electronic band structure (Sajjad *et al.*, 2017). Furthermore, Yao *et al.* investigated that centrosymmetric monolayer PtSe₂ thin film exhibits R-2 Rashba effect and intrinsic spin-layer locking (Yao *et al.*, 2017). In the very recent study Ciarrocchi *et al.* showed that high electrical conductivity and efficient transistor operation can be achieved by using only PtSe₂ material by varying the thickness from 14 to 2 nm (Ciarrocchi *et al.*, 2018).

In this study, motivated by the recent studies revealing the superior optoelectronic properties of TMDs, we present a comprehensive investigation on thickness-dependent characteristics of 1T-PtSe₂ by performing the state of the art first-principles calculations.

3.2.2.1. Monolayer PtSe₂

For a complete analysis how structural, electronic and phononic properties of the PtSe₂ crystal evolve with the thickness, we first investigate characteristics of monolayers comprehensively.

The optimized atomic structure of the octahedral coordination forming 1T polytype of PtSe₂ belongs to $P\bar{3}m1$ space group. As shown in Figure 3.17(a), the Bravais lattice of 1T-PtSe₂ monolayer is hexagonal with lattice vectors, $\vec{a} = 0.5a(\sqrt{3}\hat{x} - \hat{y})$, $\vec{b} = 0.5a(\sqrt{3}\hat{x} + \hat{y})$, $\vec{c} = c\hat{z}$. 1T-PtSe₂ structure with D_{3d} point group symmetry is composed of three atomic sub-layers with Pt layer sandwiched between two Se layers. The lattice constant of the primitive unit cell of the monolayer 1T-PtSe₂ structure is calculated to be 3.70 Å which is in perfect agreement with previously reported scanning transmission

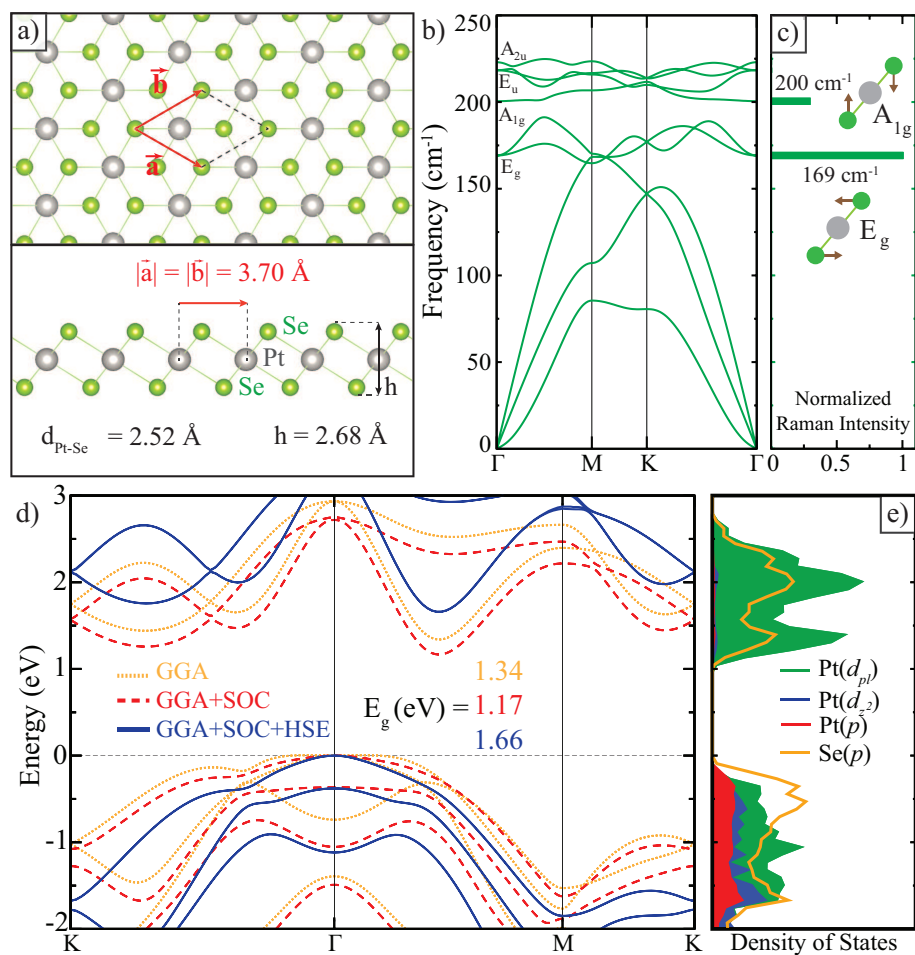


Figure 3.17. (a) Top and side views of geometric structures of 1T-PtSe₂ monolayer. Gray and green atoms show Pt and Se atoms, respectively. (b) The phonon band diagram and (c) normalized Raman intensity of 1T-PtSe₂ monolayer. (d) The electronic band diagram and (e) partial density of states of the monolayer structure. The Fermi level is set to zero.

Table 3.5. The calculated parameters for the 1T-PtSe₂ structures are; the lattice constants, $a=b$; overall thickness as the uppermost-lowermost Se-Se distance in the unitcell, h ; the charge donation from Pt to Se atoms, $\Delta\rho$; the cohesive energy per atom, E_{Coh} ; Φ and μ are the values of work function and magnetization, respectively; E_{gap} , the energy band gap of the structure.

	$a=b$ (Å)	h (Å/unitcell)	$\Delta\rho$ (e^-)	E_{Coh} (eV)	Φ (eV)	E_{gap} (eV)
1L PtSe ₂	3.70	2.68	0	4.43	5.36	1.17
2L PtSe ₂	3.73	7.39	0	4.53	4.64	0.19
3L PtSe ₂	3.74	12.04	0	4.57	4.67	0
4L PtSe ₂	3.75	16.67	0	4.59	4.67	0
Bulk PtSe ₂	3.77	2.56	0	4.65	0.79	0

electron microscopy (STEM) data (Wang *et al.*, 2015). The Pt-Se bond length in the 1T phase of PtSe₂ crystal structure is found to be 2.52 Å. Moreover, the thickness, defined as vertical distance between uppermost and lowermost Se layers, of 1T-PtSe₂ monolayer is (2.68 Å) is also close to the reported value of 2.53 Å (Wang *et al.*, 2015).

It is also found that the monolayer 1T-PtSe₂ is formed by a cohesive energy of 4.43 eV/atom which is comparable to the cohesive energy of MoSe₂ and WSe₂ (~ 4.56 and ~ 5.15 eV/atom, respectively) (Lee *et al.*, 2017). According to Bader charge analysis, there is no net charge transfer between bonded atoms in monolayer 1T-PtSe₂ structure and the bond character is entirely covalent in monolayer 1T-PtSe₂ structure. In addition, the work function is obtained as 5.36 eV in the monolayer 1T-PtSe₂ which is higher than that of similar dichalcogenides such as MoSe₂ and WSe₂ (4.57 and 4.21 eV, respectively) (Gong *et al.*, 2013).

However, structures obtained from total energy optimization calculations may not correspond to the ground state structure, therefore; for a reliable analysis on the stability of a structure it is also necessary to examine the dynamical stability via phonon calculations. The phonon dispersion curves of the 1T-PtSe₂ crystal structure are shown in Figure 3.17(b).

For the primitive unit cell of 1T-PtSe₂ composed of 3 atoms, phonon spectrum includes 9 phonon, 3 acoustic and 6 optical, branches, Analysis of lattice dynamics shows that the decomposition of the vibration representation of optical modes at the Γ point is $\Gamma=2E_g+2E_u+A_{1g}+A_{2u}$ for the 1T-PtSe₂ monolayer structure. Optical phonons include two doubly degenerate in-plane vibrational modes at 169 cm⁻¹ (E_g) and 218 cm⁻¹ (E_u), and two singly degenerate out-of-plane vibrational modes at 200 cm⁻¹ (A_{1g}) and 223

cm^{-1} (A_{2u}). Vibrational spectrum with eigenfrequencies through whole the Brillouin Zone indicate that of the 1T-PtSe₂ phase corresponds to a dynamically stable crystal structure.

Regarding Raman intensities, in the vibrational spectrum of 1T-PtSe₂, there are two prominent peaks likely to be observed in experiments. As shown in Figure 3.17(c), (i) one highly intense in-plane E_g mode at 169 cm^{-1} and (ii) one moderate intense out-of-plane A_{1g} mode at 200 cm^{-1} . Due to strong covalent character between Pt and Se atoms, out-of-plane motion of the Se atoms has less contribution in the Raman intensity compared to in-plane motion of the Se atoms. Corresponding eigenvectors of the Raman active E_g and A_{1g} modes are also sketched in Figure 3.17(c).

As shown in Figure 3.17(d), (e), 1T-PtSe₂ monolayer is an indirect band gap semiconductor with its valence band maximum (VBM) residing at Γ point and conduction band minimum (CBM) within Γ -M point. Calculations with, without spin-orbit interactions and HSE correction show that the band gaps of 1T-PtSe₂ monolayer are 1.34, 1.17 and 1.66 eV, besides; no change is seen at the band edges of CBM and VBM. With the effect of spin-orbit coupling (SOC), double degenerate VBM is separated at Γ point about 0.4 eV in the 1T-PtSe₂ monolayer and also CBM splits 170 meV at the point between Γ and M. It is seen that HSE correction increases the band gap about 0.5 eV.

As seen in Figure 3.17(e), PDOS shows that d and p orbitals of Pt, and p orbitals of Se are responsible for the VBM of the monolayer, whereas only d_{xy}, d_{yz}, d_{xz} and $d_{x^2-y^2}$ orbitals (d_{pl}) of Pt are dominantly responsible for CBM of the 1T-PtSe₂ structure.

Since the effect of strain due the adjacent layers is inevitable in such lamellar crystal structures, before studying the thickness dependent properties, we investigate electronic and structural parameters under biaxial strain. Here we apply the strain by scanning the lattice parameters in between monolayer and bulk 1T-PtSe₂. It is found that the Pt-Se bond length monotonically increases, while tensile strain rate increases. As seen from Figure 3.18, while VBM at the Γ point is quite insensitive against the biaxial strain, CBM at the Γ -M symmetry point shifts upwards slightly in the energy space. Hence, the reasonable tensile strain causes to change slightly the electronic band gap of the monolayer 1T-PtSe₂ structure. Against tensile deformation, the 1T-PtSe₂ monolayer is the quite robust semiconductor material which is the essential factor for its utilization in future nanoelectronics.

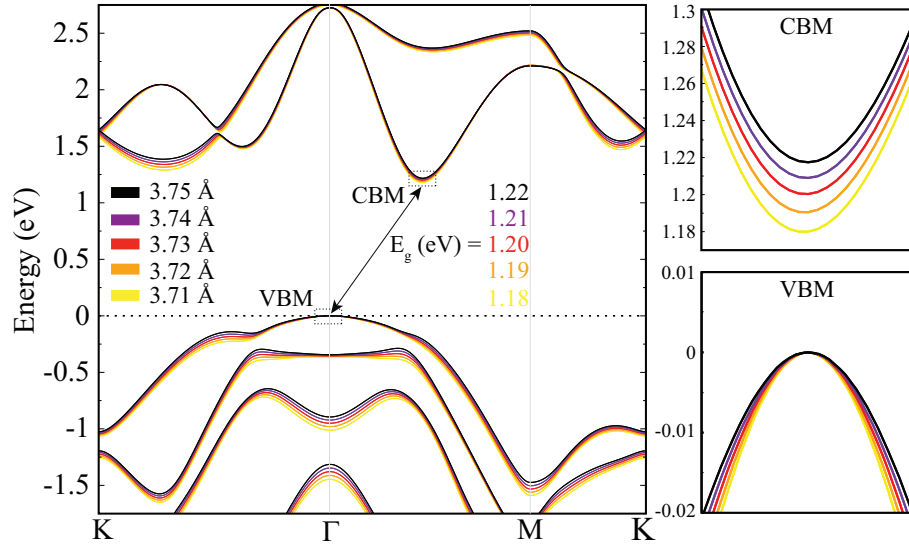


Figure 3.18. The SOC included electronic band diagrams of 1T-PtSe₂ monolayer as a function of tensile biaxial strain. The Fermi level is set to zero. Side views show the valence band maximum (VBM) and conduction band minimum (CBM) on an enlarged scale.

3.2.2.2. Dimensional Crossover From Monolayer to Bulk

Stacking order of the sublayers in a layered material directly determines its structural, vibrational, electronic and optical properties. Therefore, theoretical prediction, prior to experimental synthesis, of stacking order is of importance.

Stacking Types

Possible stacking orders in 1T-PtSe₂ crystal namely AA, AB, A'A, and A'B are presented in Figure 3.19. It is found that energetically favorable stacking order is top to top (AA), as shown in Figure 3.19 (a). In addition, AB, A'A, and A'B, stackings are found to be 159, 321 and 91 meV, respectively, less favorable than the ground state structure. The lattice constant of AA stacked structure, 3.73 Å, is consistent with the experimentally reported value (Wang *et al.*, 2015). Furthermore, the interlayer distances are calculated to be 2.14, 2.89, 3.61, and 2.63 Å for AA, AB, A'A, and A'B stacking orders, respectively.

It is also seen that while the thickness of single layer PtSe₂ is 2.68 Å, with additional layers thickness of each single layer is reduced and finally reaches to bulk value of 2.56 Å. Moreover, going from bilayer to bulk, the interlayer distance (vertical vacuum

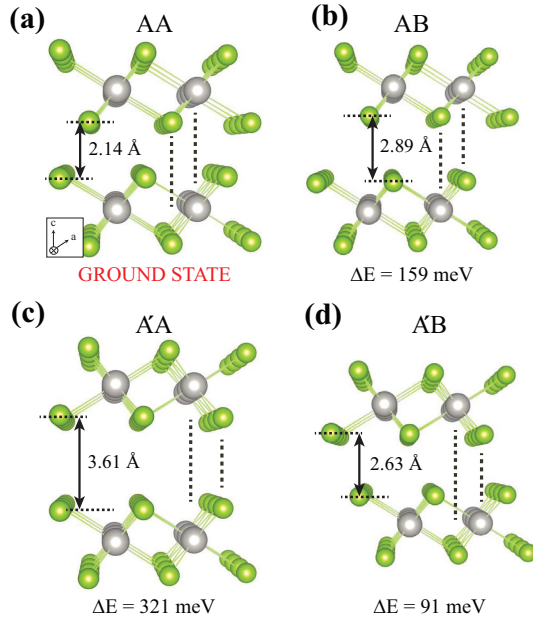


Figure 3.19. Top and side views of crystal structure of bilayer 1T-PtSe₂; (a) AA, (b) AB (c) A'A, and (d) A'B stacking orders. The ground-state energy differences are given under each stacking type labeled with ΔE .

spacing between the adjacent layers) also decreases from 2.14 to 2.07 Å. Apparently, there is an increasing trend in layer-layer interaction in the out-of-plane direction and therefore, as a result of thickness-driven compression, covalent Pt-Se bonds are enlarged. As listed in Table I, lattice constant of the bilayer, trilayer, four-layer, and bulk structures are found to be 3.73, 3.74, 3.75, and 3.77 Å, respectively.

Thickness Dependence of Electronic Properties

In order to determine how the electronic characteristics are modified with increasing number of layers, we also calculate the electronic band dispersions of monolayer, bilayer, trilayer, and bulk PtSe₂. As shown in Figure 3.20, going from monolayer to bilayer structure, the electronic band gap of the material rapidly decreases from 1.17 eV to 0.19 eV and it is also found that PtSe₂ crystals having thickness larger than the two layers all exhibit metallic behavior. In monolayer and bilayer structures of PtSe₂ the CBM states are composed of *d* state electrons that occupy d_{xy}, d_{yz}, d_{xz} and $d_{x^2-y^2}$ orbitals of Pt atom.

While the location of CBM in BZ remains same (at the Γ -M) when going from monolayer to bilayer, VBM is shifted from the Γ to the K- Γ high symmetry point. It is also worth to note that local minimum energy state of the CBM of the monolayer within

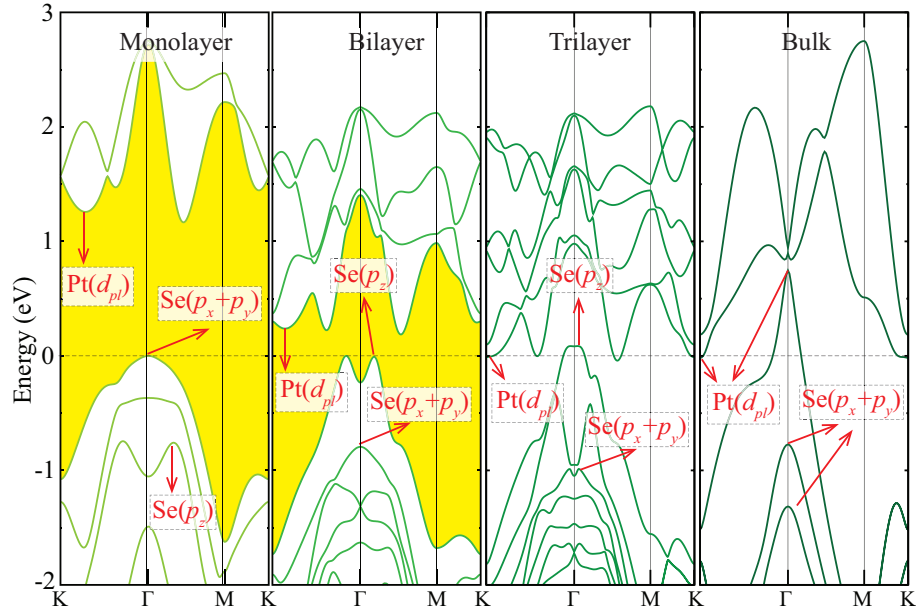


Figure 3.20. The electronic band dispersions of monolayer, bilayer, trilayer, bulk 1T-PtSe₂. The Fermi level is set to zero.

the K- Γ translocates its position in the Brillouin Zone to the K symmetry point with the effect of additional layers. Rapid decrease in band energy of CB states and increase in VB states leads to metallization starting from trilayers.

On the other hand, the VBM state of the monolayer, that originates from p_x and p_y states of Se atoms, changes its energy space and takes position at the states energetically lower than the VBM state of the few-layer PtSe₂. Moreover, the VBM state of the bilayer, which consists of p_z orbitals of Se atoms, crosses Fermi level and becomes one of the metallic transition band at the few-layer PtSe₂, as seen in the first case same trend appears in the p_z orbitals of the Se atoms. It is obviously seen that the nesting in the corresponding state disappears while number of layer of PtSe₂ increases.

Thickness Dependence of Vibrational Properties

Investigation of the vibrational properties not only allows one to deduce the dynamical stability of the structure but also allows determination of characteristic properties such as bond strengths, layer thickness and polarizability. In this subsection, thickness dependency of phonon band dispersions, Raman intensities and eigen-frequency shifts of the prominent peaks of bilayer, trilayer, four layer and bulk PtSe₂ are investigated.

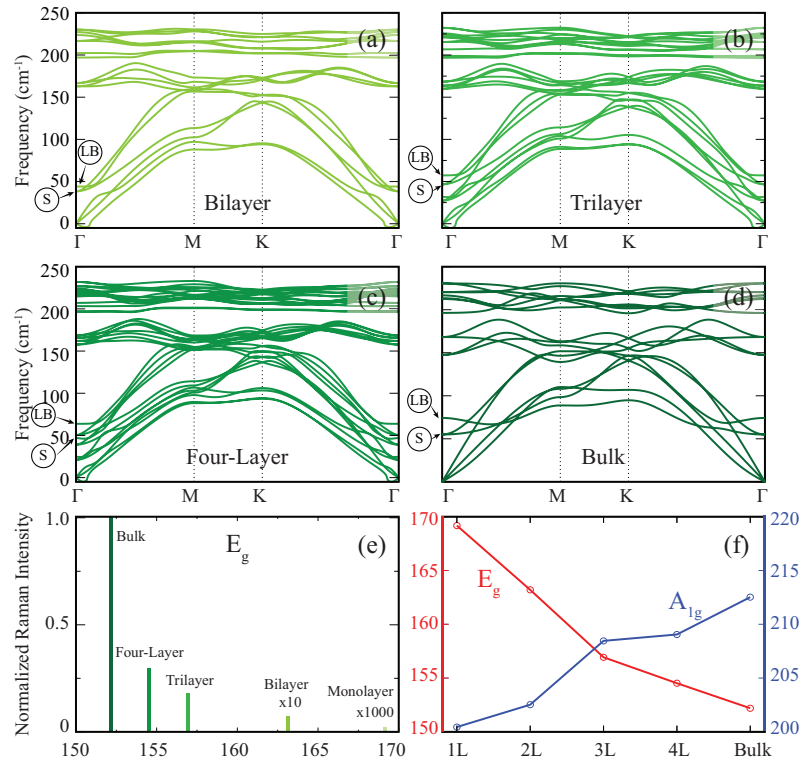


Figure 3.21. The phonon band dispersions of (a) bilayer, (b) trilayer, (c) four-layer and (d) bulk. The S and LB mode frequencies are indicated. (e) Layer dependent Raman intensity of E_g mode. (f) Frequency shifts of the E_g and A_g modes with respect to number of layers. 1L, 2L, 3L and 4L denote monolayer, bilayer, trilayer and four-layer, respectively.

Figures 3.21 (a)-(d) show the calculated phonon band structure of bilayer, trilayer, four layer and bulk PtSe₂. It is seen that all the phonon modes have real eigenfrequencies, which indicate that bulk and few-layered PtSe₂ are stable. The appearance of small imaginary frequencies (less than 5 cm⁻¹) near the gamma point are not an indication of instability, they are numerical artifacts caused by the inaccuracy of the FFT grid. As shown in Figures 3.21 (a)-(d), while LA modes cross the low-frequency optical modes, highest-frequency dispersionless optical modes are well-separated from low-lying phonon branches. Computationally predicted modes at 152.2 and 212.5 cm⁻¹ correspond to the E_g and A_{1g} phonons of bulk PtSe₂ are in good agreement with previous experimental results indicating the reliability of computational methodology of phonons (O'Brien *et al.*, 2016). As shown in the figure, in addition to the E_g and A_{1g} modes of the monolayer structure, additional peaks with low frequencies correspond to shear (S) and layer-breathing (LB) appear with the increasing thickness. It is found that S and LB modes are Raman active and as the number of layer increases from bilayer to bulk, the frequencies of S and LB modes increase from 38.8 and 44.0 cm⁻¹ to 55.0 and 74.3 cm⁻¹, respectively.

It is also worth noting that, as shown in Figure 3.21 (e), Raman vibrational characteristics of the E_g phonon strongly depend on the material thickness. It appears that, with increasing thickness, layer-layer interaction originated compression on each sub-layer yields two consequences in PtSe₂; (i) phonon softening due to enlarged Pt-Se bonds and (ii) increasing Raman activity due to enhanced polarizability.

It is also seen from Figure 3.21 (f), when the number of layers is increased, A_{1g} peak hardens while E_g peak softens. The downshift in the frequency of E_g peak is ascribed to the change in the dielectric screening environment for long-range Coulomb interactions as the thickness of the material increases. However, the upshift in the frequency of A_{1g} peak is attributed to increasing interlayer interactions which enhance the restoring forces on the atoms (Lee *et al.*, 2010; Molina-Sanchez and Wirtz, 2011). Therefore, the strong layer dependency of Raman intensity of E_g mode and peak positions of E_g and A_{1g} modes can be used to determine the material thickness.

3.2.2.3. Conclusions

In this study, we investigated thickness dependency of structural, vibrational and electronic properties of the 1T-PtSe₂ by performing first-principles calculations. First, it was found that the monolayer of platinum diselenide forms a dynamically stable hexagonal 1T phase, and the monolayer is an indirect band gap semiconductor.

The electronic nature of the monolayer structure changes negligibly under biaxial tensile deformation revealing the robust semiconductor character of the material. In addition, electronic dispersion calculations on crystals of various thickness showed that while monolayer and bilayer structures of 1T-PtSe₂ are indirect band-gap semiconductors, all thicker structures exhibit metallic character.

The layer-dependent vibrational spectra of the 1T-PtSe₂ structures reveal that Raman active shear mode, layer-breathing mode, E_g mode, and A_{1g} mode display significant shifts indicating the increasing layer-layer interaction. Moreover, Raman intensity of the E_g phonon branch is found to be quite sensitive to the material thickness and therefore it can be used for determination of number of layers by Raman spectroscopy.

Our study provides an insight into the electronic and vibrational properties of ultra-thin 1T-PtSe₂ materials and also a computational strategy for identifying the number of layers of 1T-PtSe₂ at the atomic scale.

3.3. Effect of in-plane strain

The built-in strain is inevitable as single-layer materials are usually grown on a substrate. It was shown that strain can significantly alter mechanical, electronic and magnetic properties of ultra-thin materials (Rodin *et al.*, 2014; Jiang and Park, 2014; Tao *et al.*, 2014). In this section, we investigate the strain dependence of the characteristic properties of α -RuCl₃ and CdTe monolayers.

3.3.1. Tuning Electronic and Magnetic Properties of Monolayer

α -RuCl₃ by In-plane Strain

Nanoscale magnetic materials and their tunable characteristics are important for the design of nanosized controllable magnets that can be utilized for spintronic applications. A large family of two-dimensional (2D) materials are essential for fundamental studies of magnetism at the 2D limit. Although pristine graphene is nonmagnetic, nanoribbons and patches of graphene exhibit magnetic properties (Golor *et al.*, 2014; Jung and MacDonald, 2009; Wassmann *et al.*, 2008; Şahin *et al.*, 2010; Ezawa, 2007). It was also found that MoS₂ nanosheets with high density of prismatic edges show weak magnetism (Zhang *et al.*, 2007). These nanosheets exhibit 2.5 % magnetoresistance effect with a Curie temperature of 685 K. It was predicted that monolayer forms of pristine VS₂

and VSe_2 exhibit magnetic behavior (Ma *et al.*, 2012). Magnetic moment and strength of magnetic coupling strongly depend on applied strain in these materials. In previous studies, several groups have shown that the magnetism in the ultra-thin materials can be induced and engineered by applied strain (Yang *et al.*, 2015; Zhou *et al.*, 2012; Zheng *et al.*, 2014), doping by adatoms (Krashennnikov *et al.*, 2009), and by introducing vacancy defects (Yazyev and Helm, 2007; Ugeda *et al.*, 2010).

As a new member of layered materials, $\alpha\text{-RuCl}_3$, has attracted considerable attention in recent years due to its unusual magnetic properties. $\alpha\text{-RuCl}_3$ has a layered structure consisting of planes of edge-sharing RuCl_6 octahedra arranged in a slightly distorted honeycomb lattice (Fletcher *et al.*, 1967). The layers in the crystal structure are held together by weak van der Waals forces (Pollini, 1994). Spectroscopic investigations revealed that $\alpha\text{-RuCl}_3$ is a Mott insulator (Pollini, 1996). It was shown that strong electron correlations play an essential role in determining the exact ground state of this material (Plumb *et al.*, 2014).

In a recent study Kim *et al.* demonstrated that due to the electron correlations, Kitaev interactions arise in $4d$ -orbitals of $\alpha\text{-RuCl}_3$ (Kim *et al.*, 2015). It was found that the magnetic ground state of $\alpha\text{-RuCl}_3$ is a zigzag-ordered phase. Majumder *et al.* showed that $\alpha\text{-RuCl}_3$ possesses strong magnetic anisotropy and the successive magnetic order at low temperatures could be completely suppressed by applying fields up to 14 T in the honeycomb plane, whereas the magnetic order is robust when the field applied perpendicular to the crystal plane (Majumder *et al.*, 2015). It was found that g -factors of $\alpha\text{-RuCl}_3$ are strongly anisotropic (Kubota *et al.*, 2015). In another study, signature of a magnetic transition in magnetic susceptibility and specific heat data were observed (Sears *et al.*, 2015). It was found that there is zigzag type magnetic order in the honeycomb plane in this material. However, stacking disorder along the direction perpendicular to the plane leads to quite low ordering of magnetic moments. Recently, as a first case in halides, exfoliation of the $\alpha\text{-RuCl}_3$ into monolayers has been reported (Weber *et al.*, 2016).

Even though bulk form of $\alpha\text{-RuCl}_3$ was studied very extensively, very little is known about its monolayer form. The aim of the present study is to determine the structural, electronic, and magnetic ground state of monolayer $\alpha\text{-RuCl}_3$ and to investigate the effect of in-plane uniaxial strain on these properties.

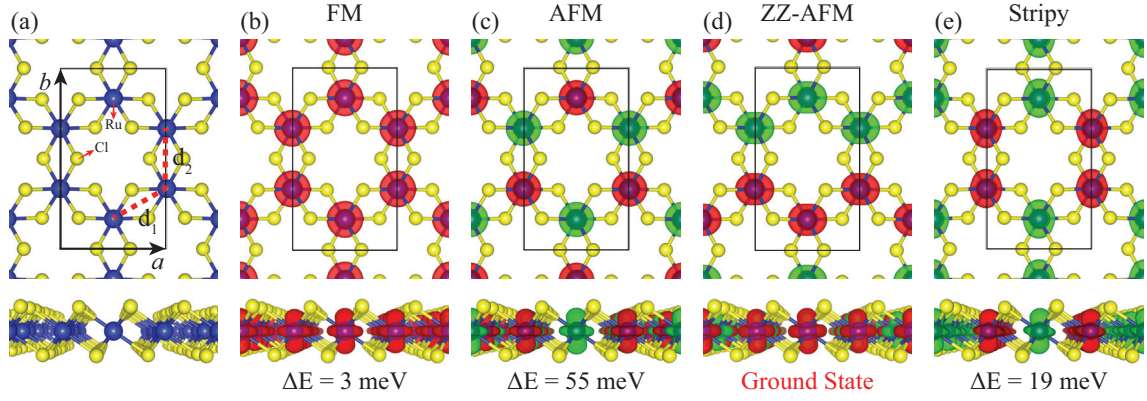


Figure 3.22. (a) Top and side views of the geometric structure of monolayer α -RuCl₃. Blue and yellow atoms show Ru and Cl, respectively. Ru-Ru distances are shown by d_1 and d_2 . Top and side views of the spin density plot of (b) FM, (c) AFM, (d) ZZ-AFM, and (e) stripy configurations (keeping the same isosurface value of $0.01 e/\text{\AA}^3$ for each of the plots). Red and green isosurfaces represent majority and minority spin densities.

3.3.1.1. Electronic and Magnetic Properties

Determination of magnetic ground state of monolayer α -RuCl₃, in which each Ru atom possess a $0.9 \mu_B$ magnetic moment, is essential for a reliable approximation of the electronic band dispersion. Four different magnetic configurations are considered such as; ferromagnetic (FM), antiferromagnetic (AFM), zigzag-antiferromagnetic (ZZ-AFM) and stripy. Spin-polarized charge densities of these magnetic configurations are shown in Figure 3.22. The conventional cell of monolayer α -RuCl₃ comprises 4 Ru and 12 Cl atoms. Total energy calculations reveal that while ZZ-AFM state is the ground state, FM, AFM and stripy configurations have 3, 55, and 19 meV per conventional cell higher energies than ZZ-AFM, respectively. Since the total energy of the FM state is quite close to the ground state, we only consider the ZZ-AFM and FM states in the rest of the paper.

The calculated lattice parameters and octahedron distances (d_1 and d_2) of ZZ-AFM and FM configurations are given in Table 3.6. It is obvious that the different magnetic orders among the Ru atoms change the equilibrium lattice parameters. RuCl₆ octahedrons of the material have quite ordered honeycomb structure in the FM state, thus the octahedron distances are the same and equal to 3.46 \AA for FM. On the other hand, magnetic interactions between Ru atoms of ZZ-AFM lead to dimer formation in the lattice. Ru atoms form dimers by decreasing d_1 to 3.45 \AA and increasing d_2 to 3.48 \AA for ZZ-AFM.

Table 3.6. Calculated conventional cell lattice parameters a and b , Ru-Ru distances d_1 and d_2 (they are shown in Figure 3.22 (a)), Bader charge transferred between Ru and Cl atoms ρ , absolute magnetic moment per Ru atom μ (Bohr magneton), magnetic anisotropy energy per Ru atom (MAE), and the energy band gap E_g .

	a (Å)	b (Å)	d_1 (Å)	d_2 (Å)	ρ (e)	μ (μ_B)	MAE (meV)	E_g (eV)
ZZ-AFM	5.97	10.44	3.45	3.48	0.3	0.9	0.80	0.96
FM	6.00	10.38	3.46	3.46	0.3	0.9	0.95	0.69

As seen in Figure 3.22, each Ru atom interacts with six Cl atoms, half of them from the top Cl-layer and the other half from the bottom Cl-layer. The bond length between Ru and Cl atoms is 2.38 Å for the FM state, whereas that of ZZ-AFM state vary from 2.37 to 2.39 Å. To investigate the bonding character in monolayer α -RuCl₃ Bader charge analysis was used. Our results show that Ru and Cl atoms are covalently bonded. Such a bond is constructed by a charge transfer of $\sim 0.3 e$ from Ru to Cl.

It is found that each Ru atom in both configurations of α -RuCl₃ has 0.9 μ_B net magnetic moment. Magnetic anisotropy energy (MAE) of the both configurations are also calculated. The MAE is the energy difference between the easy axis magnetization energy (E_{easy}) and the hard axis magnetization energy (E_{hard}),

$$MAE = E_{hard} - E_{easy}.$$

The spin-orbit interaction is added to the calculations with the following hamiltonian,

$$H_{SO} = \frac{1}{2r(m_e c)^2} \frac{dV}{dr} \vec{L} \cdot \vec{S},$$

where r is the radial distance from atom nuclei, m_e is the electron mass, c is the speed of light, V is the potential around the nuclei, \vec{L} and \vec{S} are the orbital momentum and spin operators, respectively.

As seen from Figure 3.22 the origin of magnetization is the electrons in d -orbital of Ru atoms which is not spherically symmetric. Therefore, magnetic anisotropy is expected in this material. Magnetic anisotropy defines the stability of the magnetization direction against thermal excitations. A large magnetic anisotropy is crucial to preserve magnetic moments from thermal fluctuations. Materials with a high magneto crystalline anisotropy are of importance for data storage, magnetic sensors, and spintronic applications.

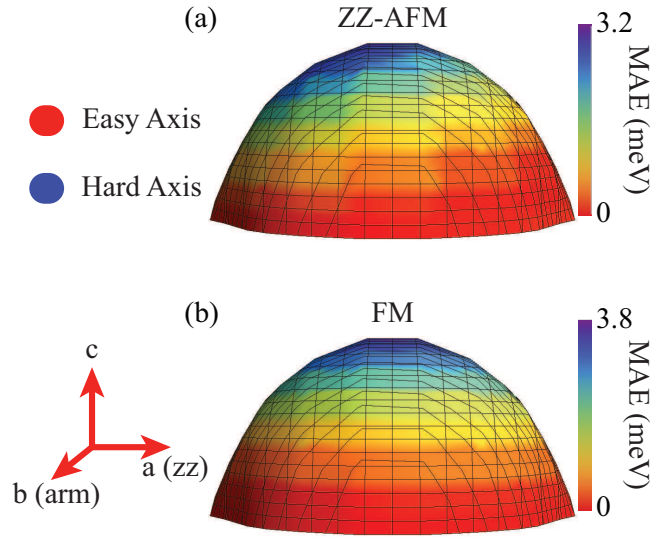


Figure 3.23. The variations of MAE values are projected on the sphere for (a) ZZ-AFM and (b) FM configurations.

Figure 3.23 shows the variations of MAE projected on the sphere for ZZ-AFM and FM configurations. The net magnetic moment of FM state is $4 \mu_B$ per conventional cell. It is found that the easy-axis for FM state is parallel to the plane of the material and in-plane anisotropy is negligibly small. However, the easy axis direction of the ZZ-AFM state makes a small angle with the plane of the material. Compared to the FM state, in-plane anisotropy of MAE is observed in the ZZ-AFM state. Energy difference between easy axis and hard axis of FM and ZZ-AFM states are 0.95 meV/Ru and 0.80 meV/Ru , respectively. Therefore, it is worth to note that although ZZ-AFM state does not have a net magnetic moment, it has comparable MAE value with the FM state.

Band dispersions of ZZ-AFM state based on GGA and GGA+SOC including U-Hubbard term are shown in Figure 3.24 (a). As seen in the figure, SOC makes negligible influence on the electronic structure of the material. ZZ-AFM state is an indirect-gap semiconductor with the calculated band gap of 0.96 eV . FM state is also an indirect-gap semiconductor, however the spin-up and spin-down bands are spin-split in both valence and conduction bands (see Figure 3.24 (b)). The band gap is much larger in the spin-up states than that of spin-down states. The band gap is 0.69 eV for the spin-up states whereas it is 2.20 eV for the spin-down states. While the conduction band minimum (CBM) of both configurations are located at the Γ symmetry point, the valence band maximum (VBM) of ZZ-AFM and FM states reside in the Y and S symmetry points, respectively. The dispersions near the VBM are quite linear for both of the cases. This indicates a

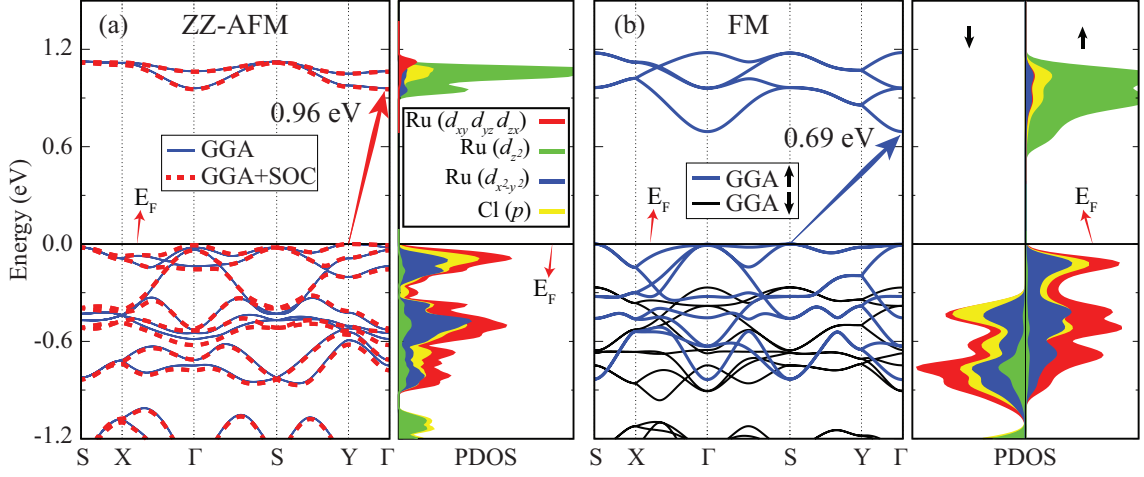


Figure 3.24. (a) Calculated band dispersions within GGA and GGA+SOC, and partial density of states (PDOS) of ZZ-AFM state of single-layer α -RuCl₃. (b) Calculated band dispersion within GGA, and partial density of states (PDOS) of FM state of single-layer α -RuCl₃. Spin-up (\uparrow) and spin-down (\downarrow) bands are shown by green and black lines, respectively. The Fermi energy (E_F) level is set to the valence band maximum.

large effective mass for the holes in this material. It is seen that the valence band edge at the Γ point differs by only 8 meV and 1 meV from the VBM of the ZZ-AFM and FM configurations, respectively. Partial density of states (PDOS) are also calculated for both of the magnetic ordering states. It is found that for both of the magnetic configurations, CBM is mostly dominated by d_{z^2} -orbitals of Ru atom, whereas VBM is composed of d_{xy} , d_{yz} , d_{zx} and $d_{x^2-y^2}$ -orbitals of Ru atom and p -orbitals of Cl atom. Near the VBM, overlap of PDOS peak positions and shapes of d -orbitals of Ru atom and p -orbitals of Cl atom reveal strong coupling in between these orbitals.

3.3.1.2. Vibrational Properties

For an accurate investigation of the dynamical stability of a material, analysis of the phonon modes provides a reliable test. We calculate the phonon-band structures based on the small-displacement method as implemented in the PHON code (Alfè, 2009). As seen on the left panel of Figures 3.25(a) and (b), both the FM and ZZ-AFM states of monolayer α -RuCl₃ are dynamically stable. There are 36 vibrational modes 3 of which are acoustical phonon branches. Since the geometry of two magnetic phases are slightly

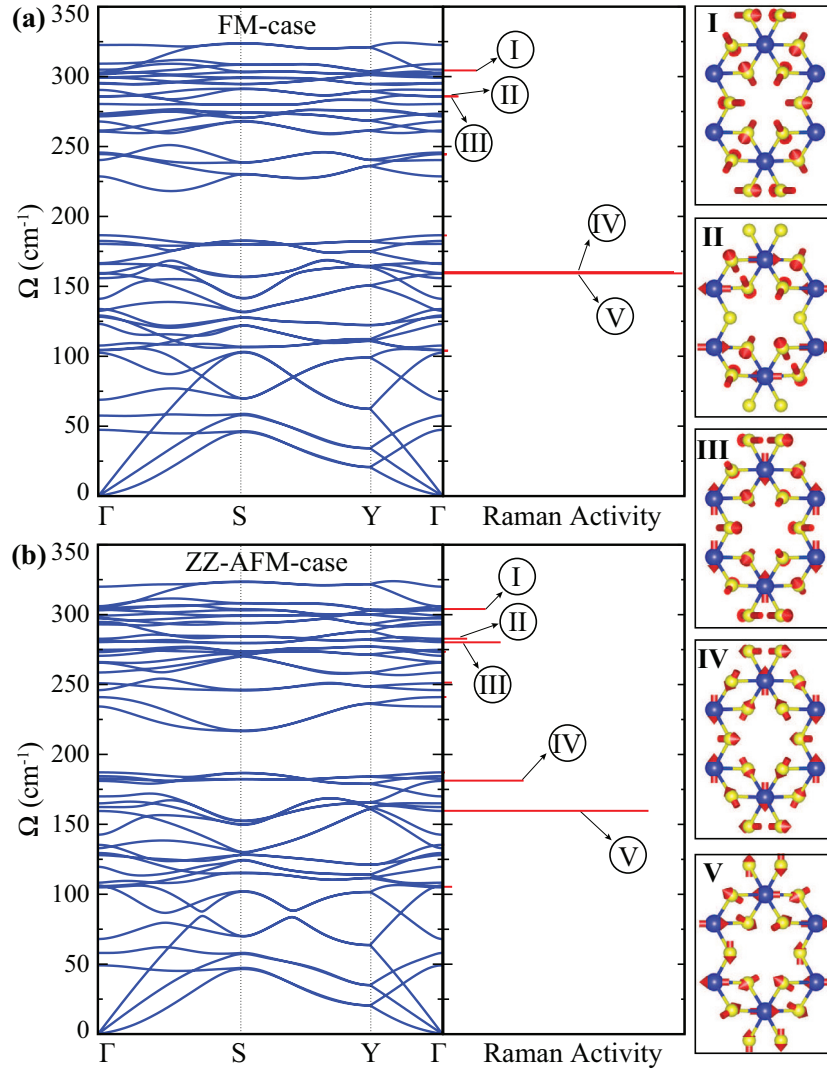


Figure 3.25. Phonon-band structure and corresponding Raman activities of monolayer α -RuCl₃ for; (a) FM and (b) ZZ-AFM configurations. Vibrational motion of individual atoms in some prominent Raman active modes are also shown on the right panel.

different (the in-plane isotropy is broken in the ZZ-AFM) phonon-band structures display differences in the peak frequencies of some phonon modes. This can be detected with a Raman measurement. As shown on the right panel of the Figures 3.25(a) and (b), there are 5 prominent Raman active phonon modes for both magnetic orders. Vibrational characteristic of the mode-I demonstrates that, the Ru atoms are stationary. Since the magnetic interaction occurs between the Ru atoms, the mode-I has approximately the same peak frequencies for both cases (305.0 and 304.0 cm^{-1} for FM and ZZ-AFM, respectively). In the other 4 phonon modes, in addition to the vibration of Cl atoms, Ru atoms also contribute to the vibration. Therefore, the shift in peak frequencies of these phonon modes is greater. The frequencies of phonon modes II and III are calculated to be 285.9 and 285.7 cm^{-1} in FM case, respectively. Although, they have very close frequencies these modes are non-degenerate. In the case of ZZ-AFM ordering, there is a splitting between modes II and III (the frequencies are 282.7 and 280.3 cm^{-1} for mode-II and III, respectively). In addition to the splitting of the frequencies, there also occurs small phonon softening in the ZZ-AFM case. In fact, the larger splitting occurs between phonon modes IV and V when the ZZ-AFM interaction exists in the crystal. The frequency of phonon mode-IV is calculated to be 159.5 and 181.1 cm^{-1} in FM and ZZ-AFM cases, respectively. This large splitting of the frequency is a strong indication of different magnetic interaction in the crystal. However, the phonon mode-V has exactly the same frequencies (159.5 cm^{-1}) in both cases. In addition, as seen in Figure 3.25, the Raman activities of phonon modes IV and V are higher in the FM case which can also be a key for the indication of different magnetic interactions in the crystal. Therefore, it can be pointed out that although, two magnetic cases have very close total energies (3 meV of difference) their Raman spectra are considerable different.

3.3.1.3. Strain Application

Formation or synthesis of monolayer crystals by removing adjacent layer not only leads to dimensional crossover from 3D to 2D behavior of elementary excitons but also increases the sensitivity of the crystal against strain. Soft materials such as RuCl_3 may exhibit interesting properties under external strain. Since it is an easy and effective method, strain is often used to manipulate fundamental properties of ultra-thin materials (Şahin *et al.*, 2009; İyikanat *et al.*, 2017; Levy *et al.*, 2010; Gui *et al.*, 2008; Ma *et al.*, 2012). Hence, the strain effect on the structural, magnetic, and electronic properties of monolayer $\alpha\text{-RuCl}_3$ are investigated in this section.

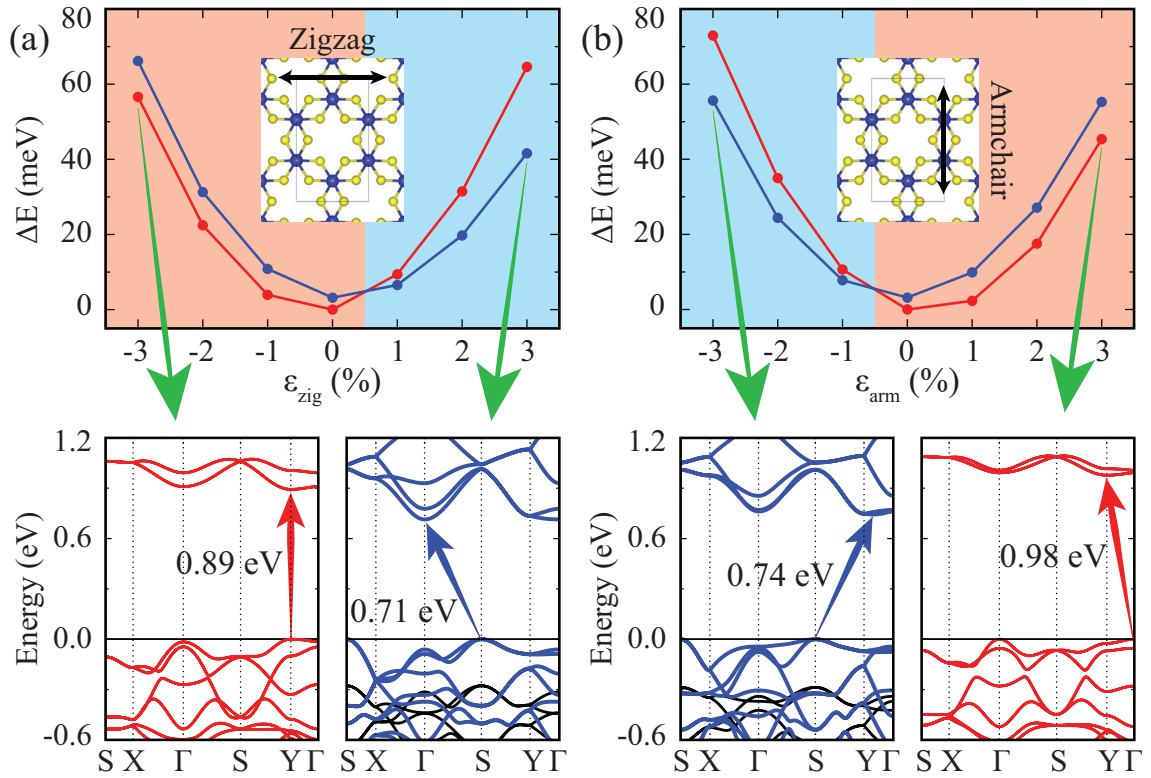


Figure 3.26. The variations of the total energy differences and ground state electronic band dispersions of ZZ-AFM and FM phases as a function of in-plane strain along (a) zigzag (ϵ_{zig}) and (b) armchair (ϵ_{arm}) directions. Blue and red shaded regions delineate the FM and ZZ-AFM regions, respectively.

Figure 3.26 shows in-plane strain-dependent total energy differences of ZZ-AFM and FM configurations with respect to the unstrained case. Using the rectangular conventional cells shown in the Figures 3.22 (b) and (d) uniaxial strain is applied along the zigzag (ϵ_{zig}) and armchair (ϵ_{arm}) directions. The lattice parameters of the conventional cells for compressive and tensile strains are changed up to 3%. The conventional cell vector perpendicular to the direction of applied strain and atomic positions are fully relaxed.

As seen in Figure 3.26 (a), the magnetic ground state of monolayer α -RuCl₃ experiences a phase transition from ZZ-AFM to FM below 1% tensile strain along the zigzag direction. While magnetic ground state of the material is still FM, energy differences between FM and ZZ-AFM states increases with the increase of tensile strain. However, applying compressive strain along the zigzag direction does not produce such a change in the magnetic ground state of the material and energy differences between ZZ-AFM and FM states are almost unchanged with the increase of compressive strain. Figure 3.26 (b) clearly shows that opposite scenario occurs when the uniaxial strain is applied along the armchair direction. The magnetic ground state changes from ZZ-AFM to FM below 1% compressive strain. Therefore, it is obvious that applying uniaxial strain is an easy and practical method to modulate magnetic ordering in this material.

Since applied in-plane strain significantly modifies interatomic distances and distribution of electrons, it can induce prominent variations in the electronic characteristics of the material as well. Hence, in this section, the modifications in the electronic structure of monolayer α -RuCl₃ caused by the in-plane strain are discussed. Lower panels of Figures 3.26 (a) and 3.26 (b) present evolution of the electronic band dispersions of ZZ-AFM and FM configurations under uniaxial strains, respectively. We find significant strain-induced changes in the VBM and CBM. The ground state of the material is ZZ-AFM and it is a semiconductor with a direct gap at the Y symmetry point when 3% compressive strain is applied along the zigzag direction. With the increase of tensile strain up to 3% along the same direction, valence band at the S point moves upwards in energy, and the FM phase exhibits an indirect gap ($S \rightarrow \Gamma$) character. The material exhibits FM configuration with an indirect gap ($S \rightarrow$ between the Y - Γ) when 3% compressive strain is applied along the armchair direction. The ground state of the material is ZZ-AFM with an indirect band gap ($\Gamma \rightarrow Y$) under 3% tensile strain along the armchair direction

3.3.1.4. Conclusions

In summary, we performed first-principles calculations in order to investigate the structural, vibrational, electronic, and magnetic properties of monolayer α -RuCl₃ and the effects of in-plane strain on these properties. Magnetic ordering in the ground state of the material is ZZ-AFM, with a FM phase present just 3 meV above the ground state. It was found that both magnetic configurations possess strong magnetic anisotropy. Our calculations revealed that both ZZ-AFM and FM phases are indirect gap semiconductors. The calculated phonon dispersion curves showed that both phases are dynamically stable. It was also predicted that since the phonon modes of the two phases exhibit substantial differences, magnetic state of the material can be monitored by a Raman measurement.

Moreover, our calculations revealed that magnetic ground state of the material can be readily tuned by certain in-plane strains. The band gaps of ZZ-AFM and FM states remain almost unchanged under in-plane strain, whereas significant modifications occur at the valence and conduction band edges. With its strain-dependent magnetic properties, monolayer α -RuCl₃ is promising material for future spintronic applications.

3.3.2. Stable Ultra-thin CdTe Crystal: A Robust Direct Gap Semiconductor

Recent studies have shown that not only layered materials but also ultra-thin forms of non-layered materials that consist of a few atomic layer thickness can form 2D crystals (Bacaksiz *et al.*, 2017; Tan and Zhang, 2015). For instance, CdSe, CdS and CdTe nanoplatelets with thicknesses ranging from 4 to 11 monolayers were synthesized (Ithurria *et al.*, 2011). The thickness dependence of the absorption and emission spectra of these nanoplatelets were demonstrated. Park *et al.* achieved successful synthesis of 1.4-nm-thick ZnSe nanosheets with wurtzite structure (Park *et al.*, 2013). Using a colloidal template method large-scale fabrication of free-standing ultra-thin and lamellar-structured CdSe with wurtzite crystal structure was achieved (Son *et al.*, 2009). Furthermore, using a lamellar hybrid intermediate, large-area, free-standing, single-layers of ZnSe were fabricated (Sun *et al.*, 2012). Single-layers of ZnSe-pa (pa stands for n-propylamine) were exfoliated from a lamellar hybrid (Zn₂Se₂)(pa) intermediate. Then, by heat treatment pa-molecules were cleared off and the colloidal suspension of clean ZnSe single-layers was obtained. Fabricated single-layer ZnSe has four-atomic-layer thickness. They showed

that, produced single-layer ZnSe was highly stable over several days. The photocurrent densities of these monolayers are much higher than that of their bulk counterparts.

Cadmium telluride (CdTe) is one of the most popular II-VI semiconductors because of its potential applications in optoelectronic devices such as photodetectors, solar cells and room temperature X- and gamma-ray detectors (Rogalski, 2005; Gupta *et al.*, 2006; Tu and Lin, 2008; Szeles, 2004). CdTe has a direct optical band gap of ~ 1.5 eV with a high absorption coefficient (Ferekides *et al.*, 2004; Mahabaduge *et al.*, 2015). CdTe crystallizes in the zinc-blende structure at room temperature. The CdTe thin films can be grown by various deposition techniques such as chemical vapor deposition (Kim *et al.*, 2010), pulsed laser deposition (Diamant *et al.*, 1998), electrochemical deposition (Bonilla and Dalchiele, 1991), and spray pyrolysis (Ison *et al.*, 2009). Generally, the intrinsic properties of ultra-thin materials exhibit drastic changes compared to their bulk counterparts. Thus, when a material is thinned from bulk to ultra-thin form, it can exhibit enhanced properties and new functionalities.

In this study, motivated by the recent synthesis of ultra-thin II-VI binary compounds, we investigate structural, electronic and vibrational properties of single-layer CdTe using first principle calculations based on density functional theory (DFT). Although there are a few prior computational studies on single-layer CdTe (Wang *et al.*, 2016; Zheng *et al.*, 2015), free-standing monolayer CdTe has not been predicted yet. We found that single-layer CdTe containing eight atoms in the primitive unit cell is structurally stable with anisotropic electronic properties. It has a direct band-gap at the Γ point and direct gap transition at the Γ point is not affected by strain along any direction. The strain-dependent anisotropic variation of the band gap value and its rapid increase under out-of-plane compression pressure are found.

3.3.2.1. Structural and Electronic Properties

It is well-known that the bonding character of zinc-blende CdTe is partly covalent and partly ionic (Groiss *et al.*, 2009; Guo *et al.*, 2013). Except for the (110) facets, zinc-blende structure of CdTe has polar surfaces, which are chemically highly active. Even if single-layer structures having these polar surfaces could be obtained, their chemical activity would hinder their stability. However, since the (110) surfaces are non-polar, cleavage along these planes could be more feasible.

The proposed structure of CdTe single-layers in our study have the same crystal structure as the fabricated highly stable single-layer of zinc-blende ZnSe (*zb*-ZnSe). Sun

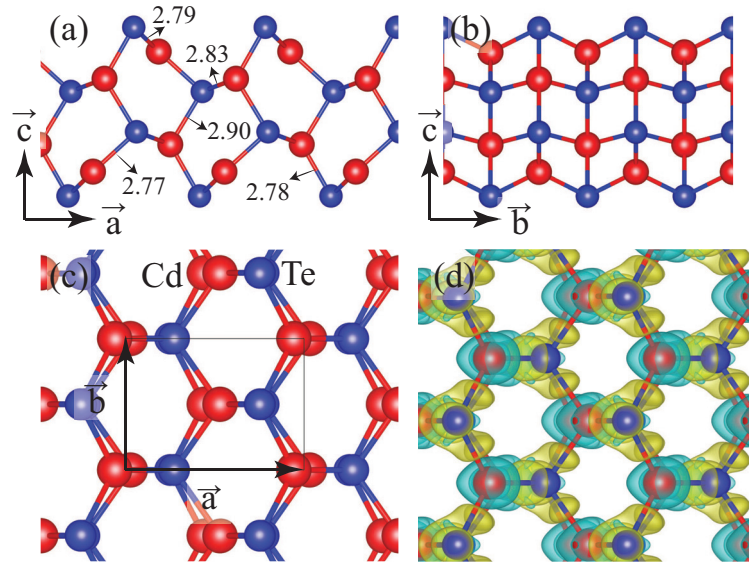


Figure 3.27. Side views (a) along \vec{a} lattice vector, (b) along \vec{b} lattice vector and (c) top view of single-layer CdTe. Black lines represent the rectangular unit cell. (d) The charge densities of the isolated Cd and Te atoms are subtracted from the charge density of single-layer CdTe. The yellow and blue densities stand for the negative and positive charges, respectively. Red and blue atoms are for Cd and Te, respectively.

Side views along \vec{a} and \vec{b} directions and top view of single-layer CdTe are shown in Figures 3.27 (a)-(c), respectively. Lattice parameters of single-layer CdTe are found to be $a = 6.18$ and $b = 4.53$ Å. Calculated lattice parameters are smaller than those for bulk CdTe which is 6.52 Å. Figure 3.27 (a) shows that the Cd-Te bond lengths vary from 2.77 to 2.90 Å, bond lengths between surface atoms being smaller than those of the inner atoms in the layer. As seen in Figure 3.27 (b), Te atoms are at the surfaces of the layer, and each surface Te atom binds to three Cd atoms. The inner Te atoms are surrounded by 4 Cd atoms with tetrahedral type bonds. During the atomic relaxation of the truncated layer, Cd atoms that are at the surface recede toward the inner Te atoms; remaining Te atoms move outward. Such reconstructions stabilize the layer surfaces.

Bader charge analysis reveals that each Cd atom donates $0.5e$ to each Te atom. To illustrate the charge transfer mechanism three dimensional charge density differences are shown in Figure 3.27 (d). The charge density differences were calculated by subtracting charge of isolated Cd and Te atoms from charge of single-layer CdTe. The charge transfer between Cd and Te atoms resembles polar-covalent bonding. Due to a difference in the electronegativities of Cd and Te atoms (1.69 and 2.10 for Cd and Te atoms, respectively),

the Cd-Te bonding has also some ionic character. Finally, the cohesive energy per atom of single-layer CdTe is 1.79 eV which is less than the bulk value of 2.20 eV per atom.

To investigate the full band dispersions and the characteristics of band edges in the Brillouin Zone (BZ), whole BZ energy-band structure is calculated and given in Figure 3.28 (a). As shown in the figure, valence band maximum (VBM) and conduction band minimum (CBM) of CdTe reside at the same symmetry point of the Γ . The calculated GGA electronic-band structure demonstrate that single-layer CdTe is a direct-gap semiconductor with a band gap of 1.42 eV. In order to give more accurate gap energy of the single-layer CdTe the calculated band structures within HSE06 correction are also shown in Figure 3.28 (a). A calculated HSE06 gap of single-layer CdTe is 2.13 eV. Since the trend and qualitative behavior of all the bands calculated using GGA and HSE06 are similar, only the GGA based results are given in the rest of the paper. In order to properly understand the electronic properties of CdTe, partial density of states (PDOS) is also plotted in Figure 3.28 (b). The states in the vicinity of VBM are mostly composed of p_y orbitals of Te. These p_y orbitals of Te atoms are parallel to the b lattice vector of the unit cell. On the other hand, CBM is mostly made up of the s orbitals of Cd and the s and p_z orbitals of Te. Note that, the p_z orbital contribution of Te atom mainly comes from surface Te atoms. Two-dimensional contour plots of the valence band (VB) and the conduction band (CB) of the single-layer CdTe are shown in Figures 3.28 (c) and (d). The directional anisotropy at the band edges is clearly seen in the surface plots. Ionization energy (I. E.) of single-layer and bulk CdTe surfaces are also calculated and are shown in Table 3.7.

Table 3.7. The calculated ground state properties for bulk and single-layer (SL) CdTe: The lattice constants, a and b ; atomic distance between Cd and Te atoms, d_{Cd-Te} ; charge transfer from Cd to Te atom, $\Delta\rho$; the cohesive energy per atom, E_c ; energy band gap, E_{gap} ; and ionization energy, I. E.

	a (Å)	b (Å)	d_{Cd-Te} (Å)	$\Delta\rho$ (e)	E_c (eV)	E_{gap} (eV)	I. E. (eV)
Bulk CdTe	6.52	-	2.82	0.5	2.20	0.72	5.22
SL CdTe	6.18	4.53	2.77-2.90	0.5	1.79	1.42	5.15

Due to reduced crystal symmetry in a single layer form of a material, its electronic characteristics are quite different from their bulk forms. Moreover, in-plane anisotropy in the ultra-thin materials can lead to significant modifications in the electronic properties of the material. Therefore, the investigation of direction-dependent electronic properties of ultra-thin materials is of importance. The effective masses of electron (m_e) and hole

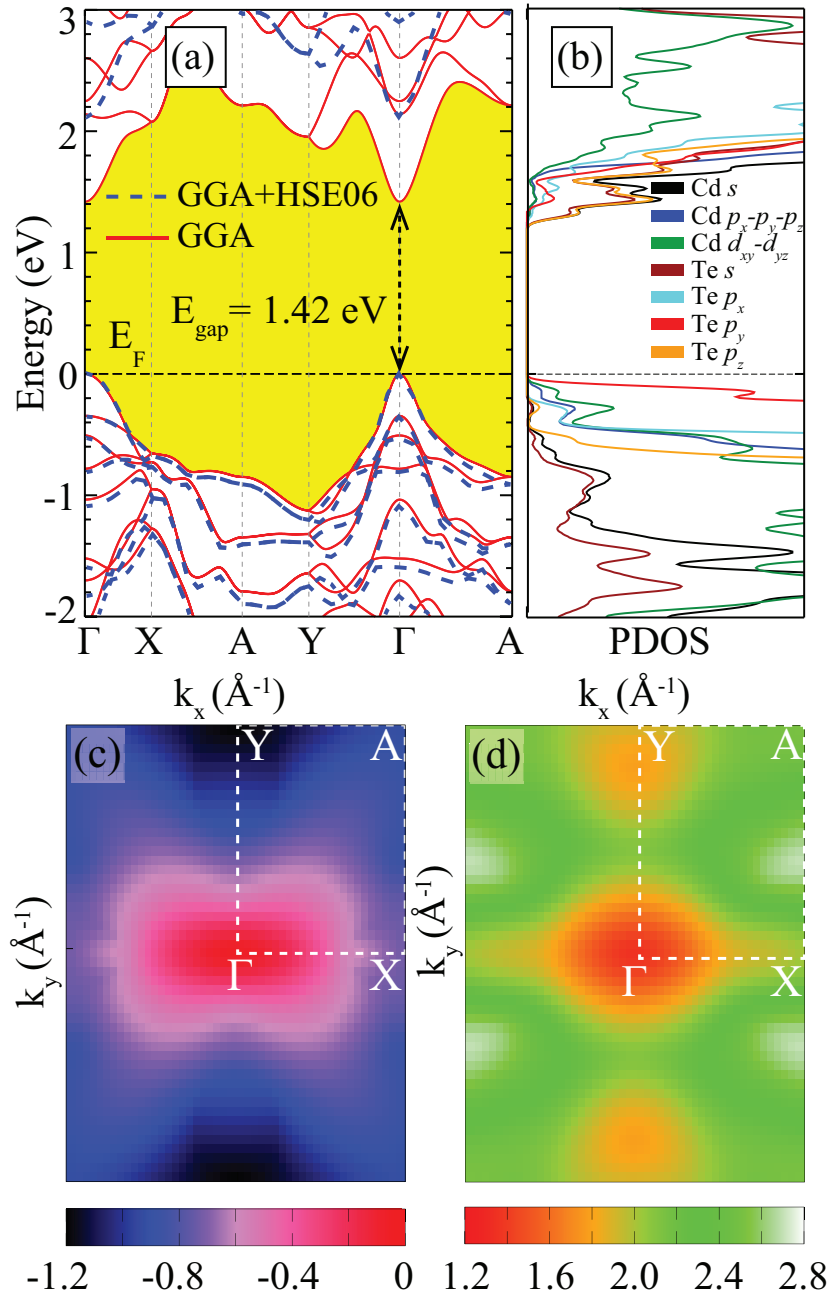


Figure 3.28. (a) Electronic band structure and (b) atom- and orbital-decomposed electronic density of states of single-layer CdTe. Fermi level is set to zero. (c) and (d) 2D surface plots of the valence band and the conduction band edges in the reciprocal space, respectively. The energy values (eV) are color coded below the plots.

(m_h) of single-layer CdTe are calculated near the Γ point. Our calculations show that the m_e and m_h effective masses are highly anisotropic around the Γ point. As given in Table 3.8 m_e values are 0.39 and 0.17 for $\Gamma \rightarrow X$ and $\Gamma \rightarrow Y$, respectively. m_h values are 0.74 and 0.14 for $\Gamma \rightarrow X$ and $\Gamma \rightarrow Y$, respectively. As seen in Figure 3.28 (b), the VBM is mainly composed of p_y electrons of Te atoms, thus this causes a high in-plane anisotropy in m_h values. The anisotropy in the electron and hole masses are evident even from the crystal structure where x - and y -directions are highly anisotropic (see Figure 3.27). For comparison, the calculated values of m_e and m_h of bulk CdTe are also given in Table 3.8.

Table 3.8. Effective masses of electrons (m_e) and holes (m_h) of bulk and single-layer (SL) CdTe.

	m_e ($\Gamma \rightarrow X$)	m_e ($\Gamma \rightarrow Y$)	m_h ($\Gamma \rightarrow X$)	m_h ($\Gamma \rightarrow Y$)
Bulk CdTe	0.09	-	0.72	-
SL CdTe	0.39	0.17	0.74	0.14

3.3.2.2. Dynamical Stability

Dynamical stability of the single-layer CdTe is investigated by examining the phonon spectra of the crystal. The small displacement method as implemented in the PHON software package is used to calculate the phonon spectra. A $4 \times 4 \times 1$ supercell is used for the phonon-band structure calculations. In Figure 3.29, we present the calculated phonon-band structure of single-layer CdTe obtained by the method described above. It is found that all the phonon modes have real eigenfrequencies, which indicate that CdTe single-layers are stable. The small imaginary frequencies (less than 1 cm^{-1}) near the Γ point are numerical artifacts caused by the inaccuracy of the FFT grid and they get cured as larger and larger supercells are considered.

The structural characteristics of bulk zb -CdTe were well studied in earlier Raman studies. The unit cell of bulk zb -CdTe consists of one Cd and one Te atoms, therefore the phonon dispersion of bulk CdTe yields three acoustic and three optical modes. Main Raman active phonon modes are transverse optical (TO) and longitudinal optical (LO) modes and they occur approximately at 141 and 168 cm^{-1} (Amirtharaj and Pollak, 1984). In addition to these prominent modes, A_1 and E symmetry modes were reported at 92 , 103 , 120 and 147 cm^{-1} which give information about the presence of Te on the surface

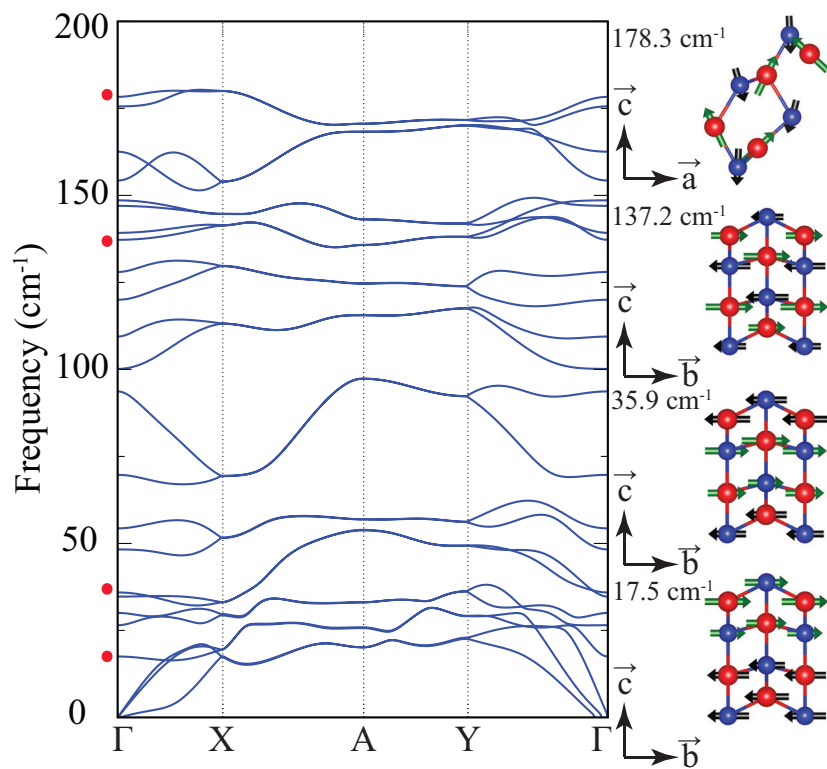


Figure 3.29. The phonon spectrum of monolayer CdTe is shown on the left. The branches of the possible Raman-active modes are indicated by the red dots and the corresponding normal modes are shown on the right.

of bulk CdTe (Amirtharaj and Pollak, 1984; Zitter, 1971).

On the other hand, the unit cell of single-layer CdTe contains four Cd atoms and four Te atoms. Therefore, the phonon dispersion of single-layer CdTe possesses three acoustic and twenty-one optical modes as shown in Figure 3.29. As pointed out in the previous section there is a relaxation of the top atomic layers in the single-layer CdTe and bond length of the surface atoms is shorter than bond length of the inner atoms. Distortions of surface atoms lead to several flat phonon bands in Figure 3.29. These distortions lift the degeneracies at the Γ point and lead to hybridization of the acoustic and optical phonon branches. Optical character and frequency of possible Raman active modes are shown in the right panel of Fig 3.29. The modes at 17.5, 35.9 and 137.2 cm^{-1} have in-plane character (E_g like) and the motion of the atoms are parallel to the \vec{b} . For the mode 137.2 cm^{-1} , Cd and Te atoms move in opposite directions. However, atomic layers exhibit contour-phase motion for the modes 17.5 and 35.9 cm^{-1} . The mode with the highest frequency of 178.3 cm^{-1} has mixed in-plane and out-of-plane character (A_g like) with Cd and Te atoms having counter-phase motion.

Due to the heavier atomic masses and more ionic electronic character, phonon modes of single-layer CdTe lie at much lower energies than phonon modes of other 2D materials such as graphene, hBN and TMDs. Moreover, it was reported that phonon modes of structurally similar material of single-layer ZnSe lie at more higher energies than that of single-layer CdTe (Bacaksiz *et al.*, 2017). Thus, it is clear that single-layer CdTe is a quite soft material.

3.3.2.3. Strain Response of Single-Layer CdTe

In this section the effects of out-of-plane compressive, in-plane compressive and tensile strains on the direct-gap semiconducting behavior of single-layer CdTe are examined. The lattice constants of the unit cell for in-plane compressive and tensile strains are changed up to 5% along zigzag (along \vec{b}) and armchair (along \vec{a}) directions. The thickness of the layer is compressed up to 5 for out-of-plane compressive strain calculations.

Figure 3.30 illustrates the evolution of electronic band structures for strained CdTe single-layer. It is clearly seen that electronic characteristics of single-layer CdTe do not change significantly with applied in-plane strain. It exhibits robust direct-gap at the Γ point under considered strain values. It is found that the band gap of single-layer CdTe is more sensitive to the in-plane strain applied along zigzag direction than armchair di-

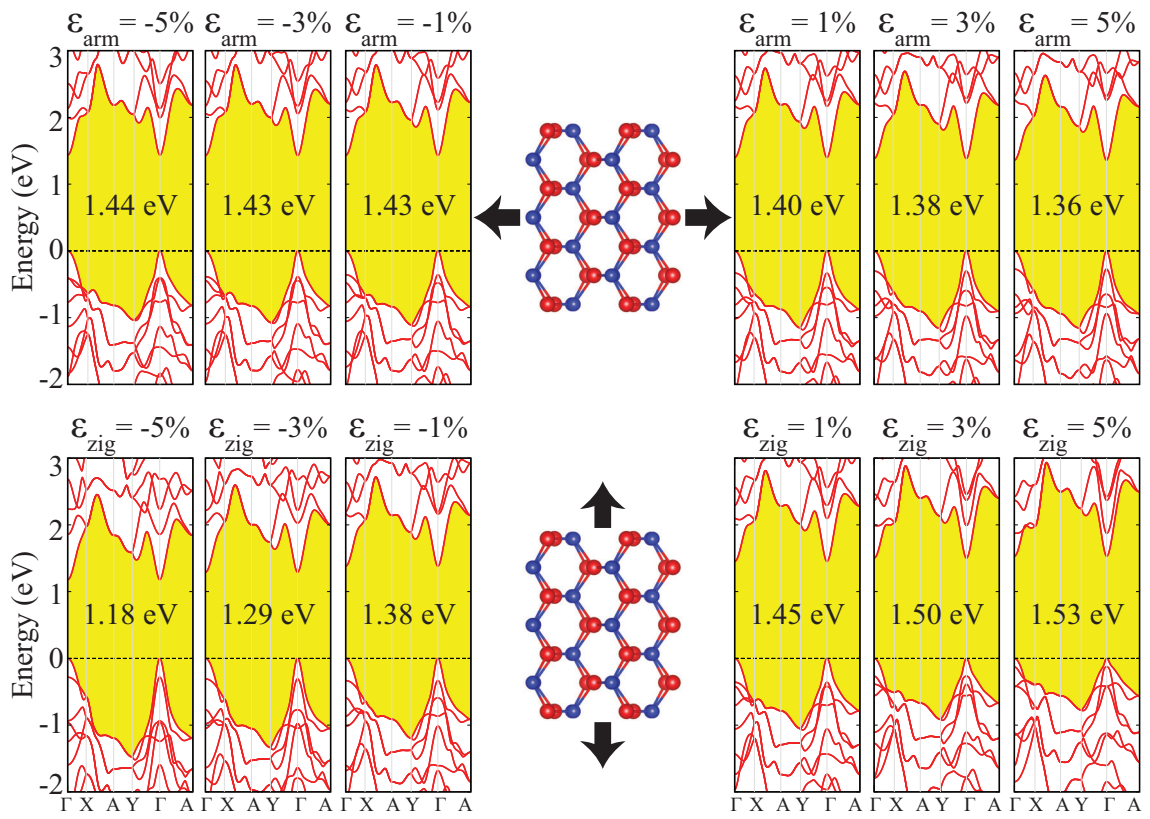


Figure 3.30. Evolution of the band dispersion of single-layer CdTe as a function of in-plane strain along armchair (ϵ_{arm}) and zigzag (ϵ_{zig}) directions. Fermi level is set to zero.

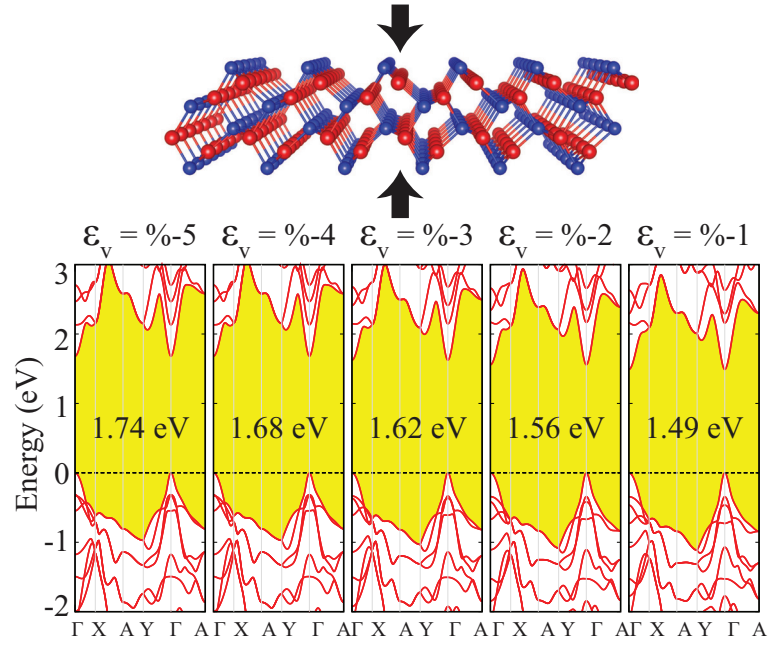


Figure 3.31. Evolution of the band dispersion of single-layer CdTe as a function of compressive strain along out-of-plane (ϵ_v) direction. Fermi level is set to zero.

rection. With the increase of tensile strain along the armchair direction, the band gap of CdTe decreases, whereas the band gap increases when compressive strain along the armchair direction is increased. However, the increase of tensile strain along zigzag direction results in an increase in the band gap of CdTe, the increase of compressive strain leads to decrease in the band gap. Figure 3.31 shows electronic band structures for single-layer of CdTe under compression along out-of-plane direction. It is found that CdTe does not show significant structural distortion under considered out-of-plane compression values. Direct gap character of CdTe at the Γ point does not change, but the electronic band gap increases as applied compressive strain increases.

Variation of the band gap of single-layer CdTe crystal under out-of-plane and in-plane strains are shown in Figure 3.32. It was already calculated that VBM of the CdTe is mainly composed of p_y orbitals of Te atoms. Since the Te- p_y orbitals are aligned in the zigzag direction, modification of band edges via applied strain occurs much faster than those in armchair direction. As shown in Figure 3.32, while the band gap slowly decreases with increasing strain in armchair direction, it rapidly increases with increasing strain in zigzag direction.

Therefore, the variation of band gap of CdTe for applied tensile strain (in ∓ 5) along armchair direction is fitted to an expression as

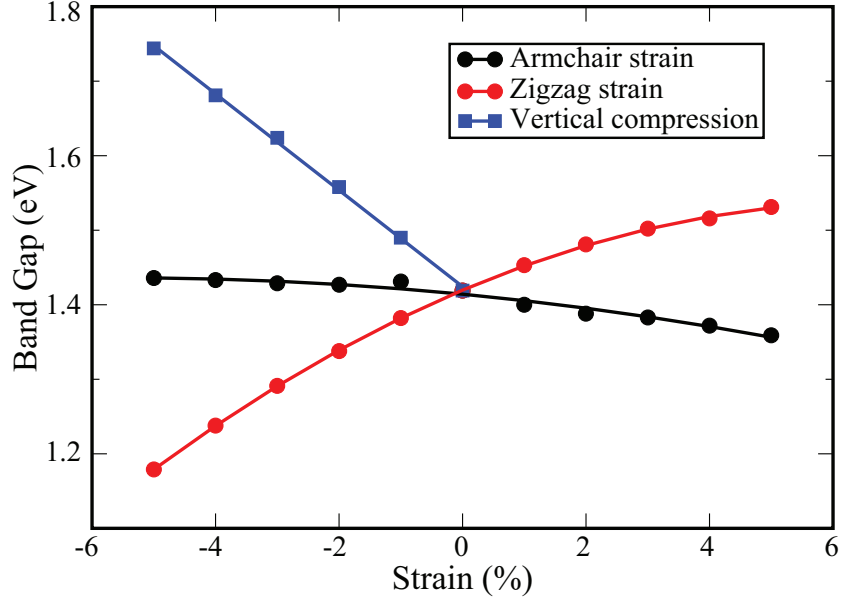


Figure 3.32. Evolution of band gaps of single-layer CdTe under in-plane and out-of-plane strain. Dots are calculated values and lines are fitted values.

$$E_{gap}(\varepsilon_{arm}) = 1.42 - \alpha\varepsilon_{arm} - \beta\varepsilon_{arm}^2 \quad (3.3)$$

α and β are fitting parameters and their values are ~ 0.008 and 0.001 eV. Compressive strain along the zigzag direction decreases the hybridization of p_y orbitals of Te atom and d orbitals of Cd atom at the VBM, whereas it increases the hybridization of Te and Cd orbitals at the CBM. Therefore, the VBM and CBM energies vary in opposite directions, thereby decreasing the band gap. The variation of band gap of single-layer CdTe for applied tensile strain along zigzag direction is fitted to an expression as

$$E_{gap}(\varepsilon_{zig}) = 1.42 + \gamma\varepsilon_{zig} - \delta\varepsilon_{zig}^2 \quad (3.4)$$

where γ and δ are fitting parameters and their values are ~ 0.035 and 0.003 eV, respectively. As a result, strain-dependence of the band gap of single-layer CdTe exhibits non-linear variations behavior when an in-plane strain is applied.

The out-of-plane strain application can easily alter the interlayer spacing of layered materials and therefore it provides an efficient way of tuning the electronic properties. In the Sec. III we found that the CBM of CdTe is dominated by p_z orbitals of Te atom. Therefore, application of compressive out-of-plane strain significantly affects the hybridization between orbitals of Cd and Te. Consequently, the band gap of CdTe

increases monotonically with increasing compressive strain along out-of-plane direction and the rate of change for band gaps is faster for the out-of-plane strain than that of in-plane strains. Increasing behavior of band gap of CdTe for applied compressive strain along out-of-plane direction is fitted to an expression as

$$E_{gap}(\varepsilon_v) = 1.42 - \zeta\varepsilon_v \quad (3.5)$$

ζ is a fitting parameter and it has a value of ~ 0.065 eV.

It appears that while the direct band gap feature is maintained, controllable modification of the band gap values of monolayer CdTe is feasible by the application of uniaxial strain along different crystallographic orientations. Mostly, electronic properties of ultra-thin materials are highly sensitive to the applied strain. It was shown that strain changes the energy dispersion, band gap, and the band edges of graphene (Wong *et al.*, 2012). In another study, the optical band gap of MoS₂ experiences a direct-to-indirect transition with applied strain, which decreases the measured photoluminescence intensity (Conley *et al.*, 2013). Previously we showed that electronic band structure of single-layer MoSe₂ undergoes a direct to indirect band gap crossover under tensile strain (Horzum *et al.*, 2013). Moreover, strain induced phase transition (from semiconducting 2H phase to metallic 1T' phase) is observed in MoTe₂ (Song *et al.*, 2015). Therefore, in contrast to typical ultra-thin materials, monolayer CdTe exhibits robust and moderate band gap that covers the broad range of the solar spectrum, which are essential for its utilization in future electronics.

3.3.2.4. Conclusions

In this study, we investigated structural, phonon and electronic characteristics of single-layer CdTe by performing state-of-the-art first principle calculations. Structural analysis revealed that ultra-thin CdTe has a crystal structure made of reconstructed 8-atomic primitive unit cell. Electronic band dispersion calculations showed that single-layer CdTe has a direct band gap of 1.42 (GGA) eV at the Γ point. Direction dependent energy band dispersions at the vicinity of VBM and CBM indicate that single-layer CdTe has anisotropic electronic and optical properties.

Moreover, it is seen that electronic characteristics of single-layer CdTe are more sensitive to in-plane strain applied along zigzag direction than armchair direction. Along

the armchair direction, the higher the tensile strain, the smaller the band gap. However, increasing the tensile strain along zigzag direction increases the band gap. In addition, when a compressive strain applied in out-of-plane direction, the rate of increase of the electronic band gap is much faster. It is also found that the direct band gap semiconducting behavior of the ultra-thin CdTe is not affected by compressive and tensile strain applied in in-plane or out-of-plane directions. Ultra-thin CdTe crystal with its strain-independent and robust direct band gap is quite suitable material for nanoscale optoelectronic device applications.

CHAPTER 4

OPTICAL PROPERTIES OF ATOMICALLY THIN LAYERED MATERIALS

Understanding the physical mechanism of light-matter interaction in materials is quite important for the development of next generation optoelectronic and photonic devices. The most important factor affecting the light-matter interaction is the relationship between the wavelength of the light and the size of the material. The size of the conventional optoelectronic devices used today is much larger than the wavelength of the light. However, the emergence of two-dimensional materials with atomic thickness made it possible to produce optoelectronic materials in sizes comparable to wavelength of the light. Increased surface effects, 2D confinement and reduced dielectric screening significantly affect the light-matter interaction in 2D materials and considerably alter the optical properties of the materials. 2D materials demonstrate a variety of new interesting optical features and exhibit great potential in device applications such as photodetectors, photovoltaics, light emitting diodes and lasers.

4.1. DFT-based Optical Calculations

In Chapter 3 we have demonstrated that DFT is highly successful in calculating the electronic properties of a wide range of materials. In this section, we focus on the layer-dependent optical properties of orthorhombic CsPbI₃ perovskites. Because a large number of atoms in the unit cell hinder the inclusion of many-body effects, DFT-level calculations will be used to calculate the optical properties of this crystal.

4.1.1. Layer-dependent Optical Properties of Orthorhombic CsPbI₃ Perovskites

In recent years, lead halide perovskites in the form of APbX₃ (where A: MA⁺, FA⁺, Cs⁺, and X: Cl⁻, Br⁻, I⁻) have attracted great attention thanks to their extraor-

dinary optical properties such as long carrier lifetime, strong light absorption, and high photoluminescence quantum yield (Protesescu *et al.*, 2015; Song *et al.*, 2015; Li *et al.*, 2017; Kovalenko *et al.*, 2017; He *et al.*, 2017). These properties make them suitable candidates for device applications such as lasers (Zhu *et al.*, 2015; Zhang *et al.*, 2016; Fu *et al.*, 2016), solar cells (Saliba *et al.*, 2016; Lee *et al.*, 2012; Green *et al.*, 2014), light emitting diodes (Wang *et al.*, 2015; Cho *et al.*, 2015), and photodetectors (Dou *et al.*, 2014; Saidaminov *et al.*, 2015). The interest in thickness dependent properties of organic, hybrid and MAPbX₃ perovskites which are suitable candidate for optoelectronic applications has started to increase and recent studies proved that optical, electronic and vibrational properties of cesium lead halide perovskites may vary with their thickness (Sichert *et al.*, 2015; Dou *et al.*, 2015).

Among cesium lead halide perovskites, cubic phase (α -CsPbI₃) show high thermal stability and excellent photoluminescence properties with a band gap of 1.73 eV which are desirable for optoelectronic device applications (Sutton *et al.*, 2016; Kulbak *et al.*, 2015). The phase transition is inevitable for α -CsPbI₃ perovskites which are stable at high temperature (>320 °C) (Dastidar *et al.*, 2017) and at ambient conditions, the α -CsPbI₃ nanocrystals transform to the orthorhombic structure which is also called yellow-phase (Sutton *et al.*, 2016; Eperon *et al.*, 2015). Although researches have been conducted the cubic CsPbI₃ to stabilize its structure, it has been found that the phase transition is inevitable and the orthorhombic phase is more favorable than the cubic phase at room temperature. Therefore, understanding this phase is a key point for dealing with cesium lead halide perovskites. However, there are very few studies (İyikanat *et al.*, 2017; Molina-Sánchez, 2018) on how the characteristic properties of cesium perovskites are modified going from their bulk to ultra-thin structures.

In this study, motivated by recent advances in synthesis and characterization of Cs perovskites, we investigate dimensional reduction dependent structural, electronic, optical and vibrational characteristics of orthorhombic CsPbI₃ perovskite crystals. A detailed analysis, based on DFT simulations, for bulk and possible bilayer and single layer structures of CsPbI₃ are presented in detail.

4.1.1.1. Possible Structures of Ultra-thin Orthorhombic CsPbI₃

This section is devoted to investigation of the possible ultra-thin crystal structures of orthorhombic CsPbI₃ structure which is the frequently obtained product at room temperature (Sutton *et al.*, 2018; Marronnier *et al.*, 2018). Crystal structures of the bulk and

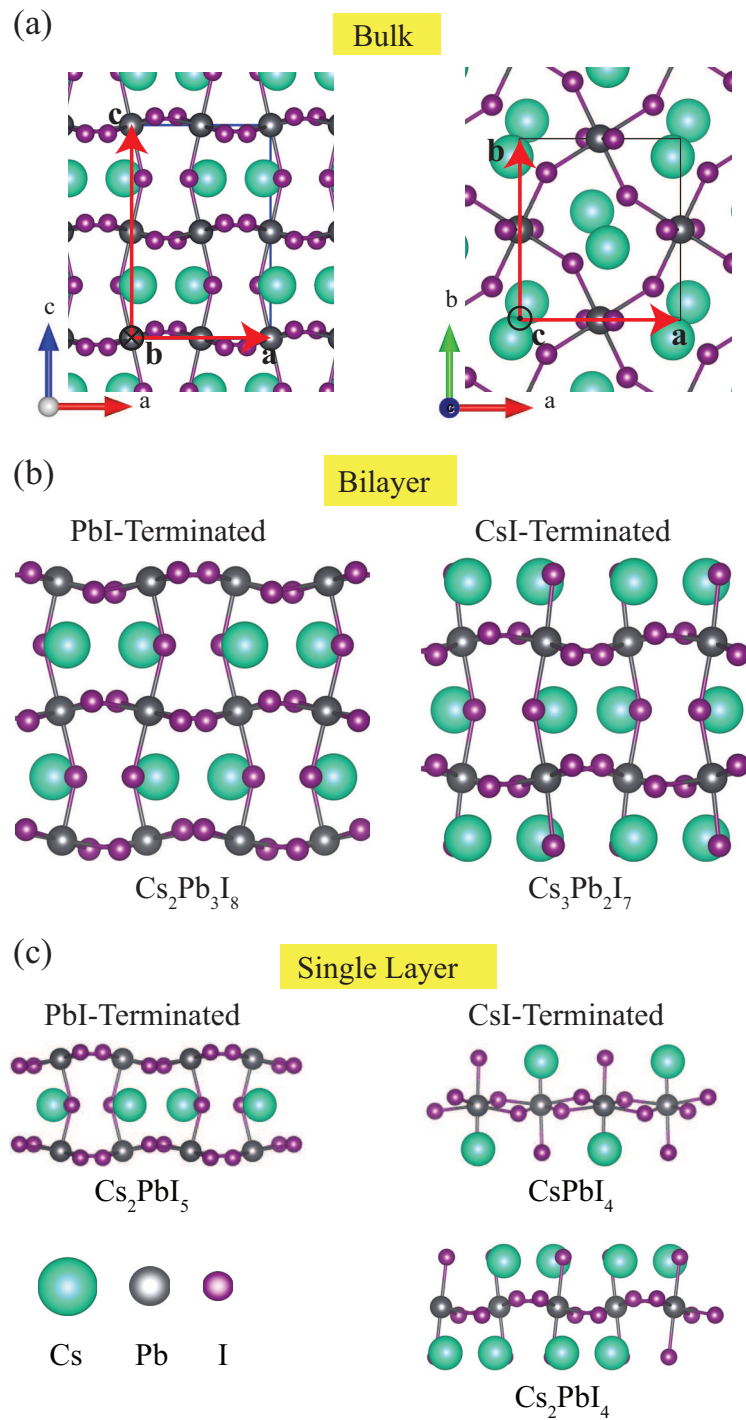


Figure 4.1. (a) Bulk, (b) bilayer, and (c) monolayer structures of CsPbI_3 crystal.

possible forms of bilayer and monolayer CsPbI₃ are shown in Figure 4.1.

Total energy optimization calculations reveal that optimized lattice parameters of bulk orthorhombic CsPbI₃ crystal are $a = 7.93 \text{ \AA}$, $b = 8.94 \text{ \AA}$, and $c = 12.21 \text{ \AA}$. CsPbI₃ crystal consists of PbI₆ octahedrals, which are tilted with respect to the cubic phase. For understanding the vibrational properties and examination of the dynamical stability phonon band dispersions of bulk CsPbI₃ are calculated (see in Figure 4.2 (a)). Phonon calculations are performed by making use of the small displacement method as implemented in the PHONOPY code (Togo and Tanaka, 2015). The phonon spectra of the bulk CsPbI₃ crystal exhibit real eigenvalues through all the symmetry points, confirming the dynamical stability of the structure and the reliability of our computational methodology. Bader charge analysis shows that Cs and Pb atoms donate 0.8 and 0.9 e , respectively while I atom receives 0.5 e .

Table 4.1. The calculated parameters for the unitcells of the bulk, bilayer and monolayer CsPbI₃; the lattice constants, a , b and c ; layer thickness, h ; the cohesive energy per atom, E_{Coh} ; the band gap of structures with LDA and PBE0, E_{gap} and E_{gap}^{PBE0} , respectively ; the work function, Φ .

	a	b	c	h	E_{Coh}	E_{gap}	E_{gap}^{PBE0}	Φ
	(\AA)	(\AA)	(\AA)	(\AA)	(eV)	(eV)	(eV)	(eV)
Bulk (CsPbI ₃)	7.93	8.94	12.21	–	3.40	0.66	1.89	–
Bilayer (Cs ₃ Pb ₂ I ₇)	7.62	9.16	-	12.46	3.13	1.26	2.58	4.52
Monolayer (Cs ₂ PbI ₄)	7.38	9.28	-	6.30	3.08	1.55	2.95	4.68

In order to figure out the thickness dependent characteristics, we first examine possible bilayer structures derived from bulk orthorhombic CsPbI₃. Two different bilayer configurations are obtained from bulk material according to atom types forming the surface of the material. Figure 4.1 (b) shows bilayer structures with Pb-I and Cs-I terminated surfaces, Cs₂Pb₃I₈ and Cs₃Pb₂I₇, respectively. It is seen from Figure 4.2 (b) that the phonon spectrum of Cs₃Pb₂I₇ exhibits real eigenvalues through all the symmetry points, whereas Cs₂Pb₃I₈ possesses imaginary eigenvalues in the large portion between the Γ and S high symmetry points. Therefore, it can be deduced that when the material is thinned down to its bilayers, only Cs₃Pb₂I₇ form is expected to be a stable. Structural analysis reveals that optimized lattice parameters of bilayer Cs₃Pb₂I₇ are $a = 7.62$ and $b = 9.16 \text{ \AA}$. The thickness of the bilayer Cs₃Pb₂I₇ is calculated to be 12.46 \AA . Bader charge analysis shows that surface and inner I atoms receive 0.6 and 0.5 e charge, respectively, whereas each Pb and Cs atoms donate 0.8 e charge. Furthermore, the cohesive energy per atom

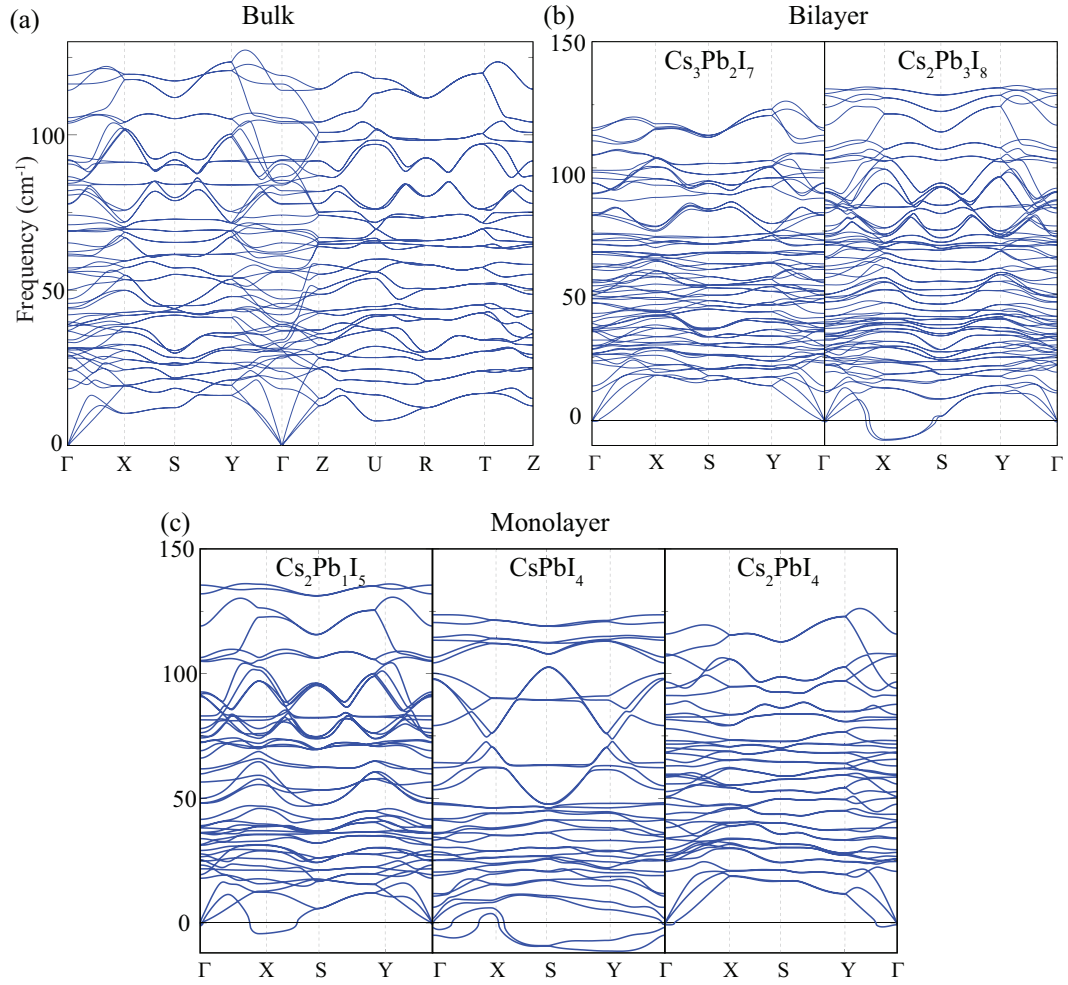


Figure 4.2. Phonon band diagram of (a) bulk CsPbI_3 crystal in orthorhombic phase, (b) $\text{Cs}_3\text{Pb}_2\text{I}_7$ and $\text{Cs}_2\text{Pb}_3\text{I}_8$ bilayers, (c) Cs_2PbI_5 , CsPbI_4 , and Cs_2PbI_4 monolayers.

of bilayer $\text{Cs}_3\text{Pb}_2\text{I}_7$ is calculated to be 3.13 eV which is smaller than that of the bulk structure (3.40 eV).

As shown in Figure 4.1 (c), there exist three possible structures when the material is thinned down to monolayer form. According to their chemical compositions, these three structures are named as Cs_2PbI_5 , CsPbI_4 , and Cs_2PbI_4 . Phonon calculations reveal that Cs_2PbI_5 and CsPbI_4 monolayers do not form dynamically stable crystal structures. On the other hand, Cs-rich form given by the formula Cs_2PbI_4 appears as the thinnest stable orthorhombic CsPbI_3 perovskite (see Fig. 4.2 (c)). It is calculated that the optimized lattice parameters of monolayer Cs_2PbI_4 are $a = 7.38$ and $b = 9.28$ Å. Apparently, reduction of the thickness of the material leads to decrease in the a lattice parameter and increase in the b lattice parameter. The thickness of the monolayer Cs_2PbI_4 is found to

be 6.30 Å. Bader charge analysis reveals that each Cs and I atoms donate 0.8 e charge, whereas I atoms receive 0.5 e charge. Table 4.1 gives that as the thickness of the material is thinned down to monolayer, the cohesive energy decreases to 3.08 eV and the work function increases to 4.68 eV.

4.1.1.2. Electronic and Optical Properties of Ultra-thin CsPbI₃

To reveal the effect of dimensional reduction on the electronic properties of CsPbI₃ perovskite nanocrystals, electronic band dispersions are calculated (by using LDA + PBE0 + SOC). As shown in Figure 4.3(a), bulk CsPbI₃ is a semiconductor with a direct band gap of 1.9 eV. Both the VBM and the CBM of the crystal reside at the Γ point. Figure 4.3 (b) and (c) show the electronic band dispersions for the stable bilayer and monolayer structures. As the thickness of the material reduces, it is evident that the electronic band dispersions remain almost unchanged while the band gap of the material increases considerably. Despite the thinning of the material and the presence of unsaturated bonds on the surface, it is seen that the material still exhibits a direct band gap at the Γ point.

Therefore, one can also expect dramatical modifications in the optical properties of CsPbI₃ upon dimensional reduction. The frequency dependent dielectric function, $\epsilon(w) = \epsilon_1(w) + i\epsilon_2(w)$, of CsPbI₃ perovskite nanocrystals was also calculated by using the PBE0 functional on top of LDA+SOC. Using the dielectric function, other optical spectral quantities such as the absorption coefficient (α), reflectivity (R), and transmissivity (T) were calculated with the following formulas;

$$\alpha(w) = \sqrt{2} \frac{w}{c} \left\{ \left[\epsilon_1(w)^2 + \epsilon_2(w)^2 \right]^{1/2} - \epsilon_1(w) \right\}^{1/2}, \quad (4.1)$$

$$R(w) = \left| \frac{\sqrt{\epsilon_1(w)} - 1}{\sqrt{\epsilon_1(w)} + 1} \right|^2, \quad (4.2)$$

$$T(w) = (1 - R(w))^2 e^{-\alpha(w)l}, \quad (4.3)$$

where l is the thickness of the material.

Frequency dependent imaginary dielectric function, absorption coefficient, reflectivity and transmissivity of bulk, bilayer, and monolayer structures are shown in Figure 4.3 (d-g). The imaginary part of dielectric functions reveals that bulk, bilayer and monolayer

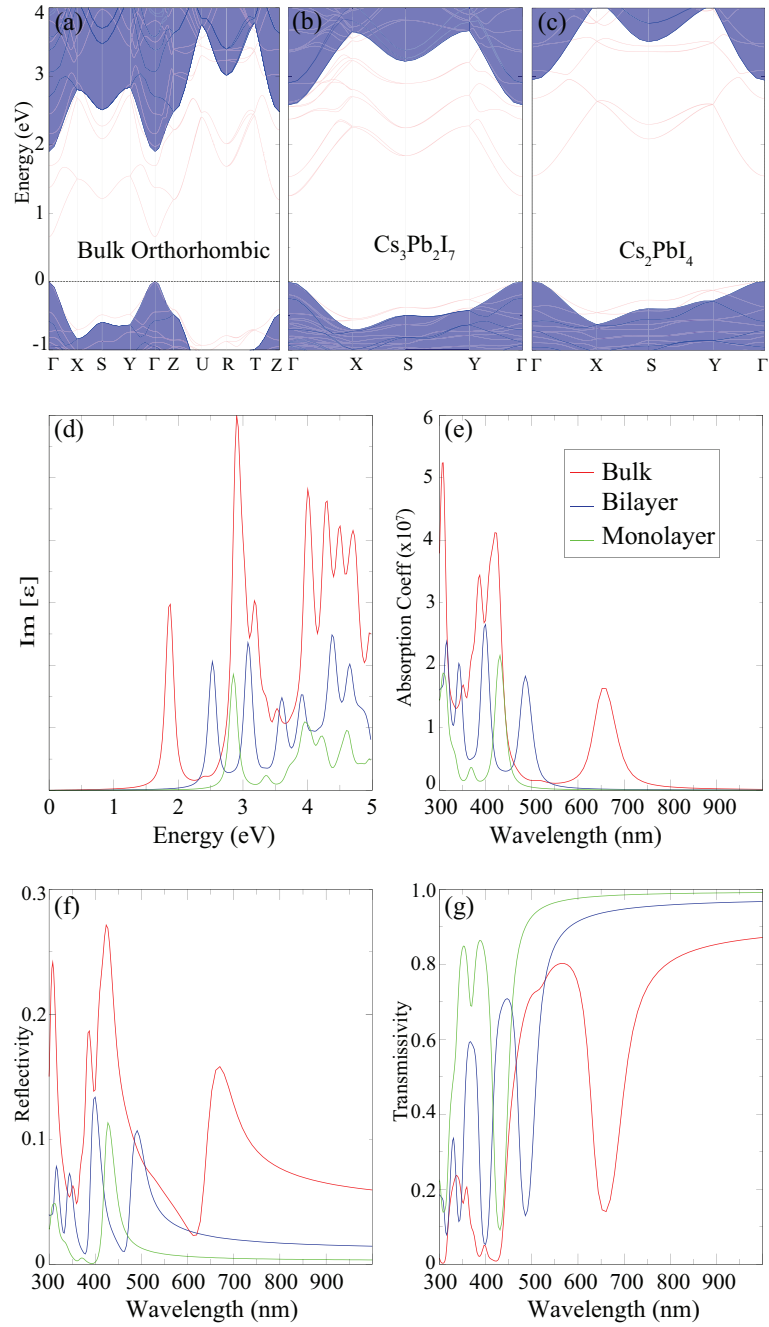


Figure 4.3. Electronic band dispersions of (a) bulk, (b) bilayer, and (c) monolayer structures of orthorhombic CsPbI_3 crystal. The layer dependent optical properties of CsPbI_3 . (a) Imaginary part of dielectric function, (b) absorption coefficient, (c) reflectivity, and (d) transmissivity of bulk, bilayer, and monolayer CsPbI_3 .

CsPbI₃ display onset around 1.86, 2.53, and 2.85 eV, respectively. In addition, absorption spectrum shows that first prominent absorption peak of bulk, bilayer and monolayer forms locate around 657, 486, and 431 nm, respectively, indicating a significant blue shift driven by dimensional reduction. As seen in Figure 4.3 (f), the reflectivity increases gradually once the layer number increases, reaching a maximum of $\sim 30\%$ for bulk. Regardless of the thickness of the material, the most significant peak of reflectivity around the visible range located in between 400-450 nm. Moreover, as illustrated in Figure 4.3 (g), as the number of layer increases the transmissivity of the material decreases. It is seen that while the transmissivity of monolayer and bilayer CsPbI₃ is very high in the 600-1000 nm, that of bulk and bilayer is almost zero near the 400 nm.

4.1.1.3. Conclusions

In conclusion, based on state-of-the-art first-principles calculations, we investigated thickness dependent characteristic properties of the orthorhombic phase of CsPbI₃ perovskite. Total energy and phonon calculations revealed that only bilayers and monolayers with Cs-I terminated surfaces may form stable thin structures. Electronic structure analysis showed that independent from the thickness all bulk, bilayer and thinnest monolayer forms of orthorhombic phase are direct band gap semiconductors with valence and conduction band edges located at the Γ symmetry point. However, as the thickness of the perovskite decreases from bulk to bilayer and then monolayer, energy band gap significantly increases. Moreover, our calculations on the optical response of the structures (dielectric function, absorption coefficient, reflectivity, and transmissivity) showed that reduction in thickness also leads to the blue shift of the absorption edge of the optical spectra. Orthorhombic CsPbI₃ perovskites, with their thickness-tunable electronic and optical properties, are quite suitable candidates for future optoelectronic applications.

4.2. Quasiparticle and Excitonic Effects in Optical Properties

Exciton is an electrically neutral quasi-particle composed of an electron and a hole interacting with Coulomb forces. Depending on the crystal structure of the material, the exciton binding energy may be an important physical quantity in determining the optical gap of the material. Due to small carrier effective mass and high dielectric screening, the exciton binding energy of typical bulk semiconductors is in the range of a few meV. Low

temperature absorption measurements showed that the exciton binding energy of GaAs crystal is 4.2 meV (Sell, 1972). Shan *et al.* showed that the electron-hole interaction in GaN and SiC is weak and therefore it is vulnerable to thermal broadening (Shan *et al.*, 1996).

Reducing the dimensionality of a material leads to enhancement of the quantum confinement effects and reduces the Coulomb screening. The reduction of the screening between the electron and the hole increases the coulomb interaction between them and this results in a very high exciton binding energy in the ultra-thin materials (Ye *et al.*, 2014; Luo *et al.*, 2011). Thus, the excitonic effects, which are highly dependent on the thickness of the ultra-thin materials, have a considerable effect on the optical spectrum of the material. It was revealed that the optical gap of single-layer MoS₂ is considerably lower than the quasiparticle band gap (Splendiani *et al.*, 2010). Ugeda *et al.* showed that many-body interactions and high exciton binding energy (0.55 eV) have a significant effect on electronic and optoelectronic properties of monolayer MoSe₂ (Ugeda *et al.*, 2014). In a theoretical and experimental study, thickness dependent exciton binding energy of few-layer black P was reported (Castellanos-Gomez *et al.*, 2014). Recently, it was found that few-layer black phosphorene has high exciton binding energy with a strong layer-dependence (Zhang *et al.*, 2018). They predicted a high exciton binding energy of ~ 800 meV for free-standing monolayer black phosphorene. In this section, we examined the effects of many-body interactions on the optical properties of ultra-thin blue phosphorene.

4.2.1. Excitonic Properties in Bilayer Blue Phosphorene

Fundamental understanding of formation of excitons is extremely important for their usage in optoelectronic devices. Previous studies reported the linear relationship between the quasiparticle band gap of a 2D material and the exciton binding energy (Choi *et al.*, 2015; Jiang *et al.*, 2017). Therefore, the exciton binding energy of wide-bandgap monolayers is expected to be much higher than that of the monolayer TMDs. Recently, monolayer form of blue phosphorene has been synthesized on Au(111) surface (Han *et al.*, 2017; Zhang *et al.*, 2016, 2018). It has a silicene-like atomic formation with a buckled layered structure. In a recent theoretical study the quasiparticle band gap of monolayer blue phosphorene was found to be much larger than that of monolayer TMDs and it has a significantly high exciton binding energy (Villegas *et al.*, 2016). Moreover it was revealed that the band gap of monolayer blue phosphorene can be altered easily by means of external stimuli (Liu *et al.*, 2015). Pontes *et al.* showed that interlayer distance of bilayer blue

phosphorene strongly depends on the stacking order (Pontes *et al.*, 2018). This feature of bilayer blue phosphorene can be exploited to engineer and manipulate the excitons for the sake of optoelectronic applications.

One of the most common methods for manipulating excitonic properties in 2D materials is to create van der Waals heterostructures. Recently, it was shown that optical spectrum of heterobilayers of TMDs is significantly altered by twist-angle dependent Moiré exciton peaks (Wu *et al.*, 2017; Yu *et al.*, 2017; Tran *et al.*, 2019). Heterostructures can host interlayer excitons where the electron and hole reside in distinct layers (Rivera *et al.*, 2015; Yu *et al.*, 2014). Because of the reduced overlap of the electron and hole wave functions, interlayer excitons exhibit longer recombination life time than intralayer excitons (Palummo *et al.*, 2015; Miller *et al.*, 2017). On the other hand, spatial separation between the charge carriers of interlayer excitons lead to reduced oscillator strength and binding energy (Torun *et al.*, 2018). Therefore, it is difficult to observe interlayer excitons in absorption experiments. Nevertheless, Deilmann *et al.* predicted formation of mixed interlayer excitons, which are composed of intralayer and interlayer excitons in bilayer MoS₂ (Deilmann and Thygesen, 2018). They stated that these mixed interlayer excitons exhibit strong and easily tunable optical amplitude.

Herein, motivated by the above studies, stacking type dependent excitonic properties of bilayer blue phosphorene are investigated by employing first principles calculations based on density functional theory (DFT) and many body perturbation theory (MBPT).

4.2.1.1. Computational Methodology

In this section, we used different first-principles simulation package; QUANTUM ESPRESSO (Giannozzi *et al.*, 2009). DFT calculations were performed with the Perdew-Burke-Ernzerhof (PBE) exchange correlation functional (Perdew *et al.*, 1996). The pseudopotentials were taken from the Pseudo-Dojo database (Van Setten *et al.*, 2018). Norm conserving pseudopotentials with a kinetic energy cutoff of 60 Ry were used. The van der Waals forces, which have a significant effect on the interlayer distances of the bilayer structures, were included using the DFT-D2 method of Grimme (Grimme, 2006). Periodic images of monolayer and bilayer structures were separated by at least 20 Å of vacuum spacing in the direction normal to the nanosheet plane. We used 18×18×1 k-point samplings for the primitive unitcells of both monolayer and bilayer structures. The cohesive energy per atom of monolayer and bilayer structures was calculated as $E_{Coh.} = (nE_s - E_T)/n$, where E_s , E_T , and n denote the single atom energy, total energy and total

number of atom in the unitcell, respectively. The convergence criterion for energy was taken to be 10^{-6} Ry between two consecutive steps. The net force on each atom was reduced to a value of less than 10^{-5} Ry/au.

The DFT eigenvalues corrected by the G_0W_0 calculation (plasmon-pole approximation) as implemented in the Yambo code (Hedin and Lundqvist, 1970; Onida *et al.*, 2002; Marini *et al.*, 2009). The excitonic effects of monolayer and bilayer blue phosphorene were calculated by solving the Bethe-Salpeter equation (BSE) on top of G_0W_0 (Rohlfing and Louie, 2000; Palumbo *et al.*, 2004). The excitations were calculated in terms of electron-hole pairs:

$$(E_{ck} - E_{vk})A_{vck}^S + \sum_{k'v'c'} \langle vck | K_{eh} | v'c'k' \rangle A_{v'c'k'}^S = \Omega^S A_{vck}^S \quad (4.4)$$

where E_{vk} and E_{ck} are the quasiparticle energies of the valence and the conduction band states, respectively. K_{eh} is describing the interaction between excited electrons and holes. A_{vck}^S and Ω^S denote the corresponding exciton eigenfunction and eigenvalue, respectively. Our test calculations showed that convergence of 50 meV of the quasiparticle band gap and optical spectrum of monolayer and bilayer structures was reached with 300 bands and $42 \times 42 \times 1$ k-point samplings. Both G_0W_0 and BSE calculations were performed with $42 \times 42 \times 1$ k-point samplings. We used 300 bands for the self-energy and 300 bands for the dynamical dielectric screening in the G_0W_0 step. The Coulomb interaction was truncated at the edges of unit cell in the direction normal to the nanosheet plane (Ismail-Beigi, 2006). Since we are interested only in the low-energy part of the optical spectra, four highest valence bands and four lowest conduction bands were included in the calculation of excitonic states.

4.2.1.2. Structural and Electronic Properties of Monolayer and Bilayer Blue Phosphorene

In this section, structural and electronic properties of monolayer and bilayer blue phosphorene with different stacking configurations are examined in detail using DFT calculations .

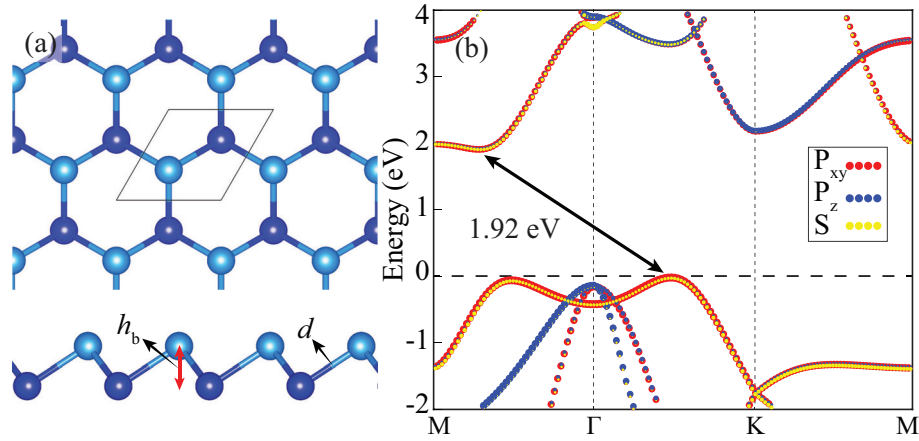


Figure 4.4. (a) Top and side views of optimized geometric structures and (b) the orbital-projected electronic band dispersions of monolayer blue phosphorene. Light and dark blue atoms show the upper and lower P atoms in the layer, respectively.

Monolayer Blue Phosphorene

As displayed in Figure 4.4 (a), monolayer blue phosphorene consists of phosphorus atoms arranged in a honeycomb lattice structure. Free-standing monolayer blue phosphorene exhibits a silicene-like buckled structure due to sp^3 hybridization. The optimized lattice constant of the monolayer blue phosphorene is found to be 3.28 \AA which is consistent with the previous experimental and theoretical studies (Zhang *et al.*, 2018; Pontes *et al.*, 2018). As given in Table 4.2, the distance between two P atoms is calculated to be $d = 2.27 \text{ \AA}$. It is found that the buckling thickness of monolayer blue phosphorene, $h_b = 1.24 \text{ \AA}$, is much larger than that of monolayer silicene (0.44 \AA). The calculated cohesive energy per atom of monolayer blue phosphorene is 3.55 eV . Previously it was predicted that while the cohesive energies of freestanding monolayer blue phosphorene and black phosphorene are very close, blue phosphorene is energetically found to be more stable than the black phosphorene, on the GaN(011), Au(111), and Cu(111) surfaces (Zeng *et al.*, 2017; Zhu and Tománek, 2014). The orbital-projected electronic band dispersions of monolayer blue phosphorene are illustrated in Figure 4.4 (b). The calculated band structure is consistent with the ones previously reported in the literature (Pontes *et al.*, 2018; Ghosh *et al.*, 2015). The monolayer blue phosphorene has an indirect band gap of 1.92 eV with the VBM located in between Γ and K points and the CBM in between Γ and M points. Orbital projected band structure reveals that the major contribution to the valence and the

Table 4.2. Calculated parameters for the monolayer and four different stacking configurations of bilayer blue phosphorene; the lattice constant, a ; P-P distance, d ; buckling height, h_b ; interlayer distance, h_i ; the cohesive energy per atom, $E_{Coh.}$; energy band gap values within GGA and GGA+G₀W₀, E_g^{GGA} and $E_g^{G_0W_0}$, respectively.

	a (Å)	d (Å)	h_b (Å)	h_i (Å)	$E_{Coh.}$ (eV)	E_g^{GGA} (eV)	$E_g^{G_0W_0}$ (eV)
Monolayer	3.28	2.27	1.24	-	3.550	1.92	3.36
AA _L	3.28	2.27	1.24	3.24	3.576	1.03	2.337
AA _H	3.28	2.27	1.24	4.12	3.563	1.52	2.965
AB _L	3.28	2.27	1.24	3.22	3.575	1.02	2.348
AB _H	3.28	2.27	1.24	4.06	3.564	1.50	2.939

conduction band edges originates from the hybridized s and p_{xy} orbitals. Moreover, there is a second valance band edge with the same orbital character as the VBM between the Γ and M points in the BZ, being only 42 meV lower in energy than the VBM.

Bilayer Blue Phosphorene

After characterizing the structural and electronic properties of the monolayer blue phosphorene, we studied its bilayer forms. It has been reported for several systems that the optical properties, electronic band dispersions and the band gaps of bilayer 2D materials strongly depend on the stacking configuration of the bilayer (Dai and Zeng, 2014; He *et al.*, 2014). Therefore, for a thorough examination of the electronic and optical properties of a bilayer material, all possible stacking configurations should be considered. As can be seen in Figure 4.5 (a)-(d) there are four different high-symmetry configurations to construct bilayer blue phosphorene. According to their stacking type and interlayer distance, we label these bilayers as follows; AA_L, top and bottom layers overlap exactly; AA_H, top and bottom layers overlap but the buckling order between the layers is reversed; AB_L, while the upper atoms of the layers overlap, lower atoms of the top layer are in the middle of the hexagon of the other layer; AB_H, while the lower atoms of the top layer are on top of the upper atoms of the bottom layer, the other atoms are in the middle of the hexagons of the other layer. Table 4.2 shows that the lattice constants, interatomic distances and buckling height of the four bilayer systems are the same as the monolayer blue phosphorene. On the other hand, the calculated interlayer distance (h_i) varies considerably depending on the type of stacking. While the interlayer distances for AA_L and AB_L

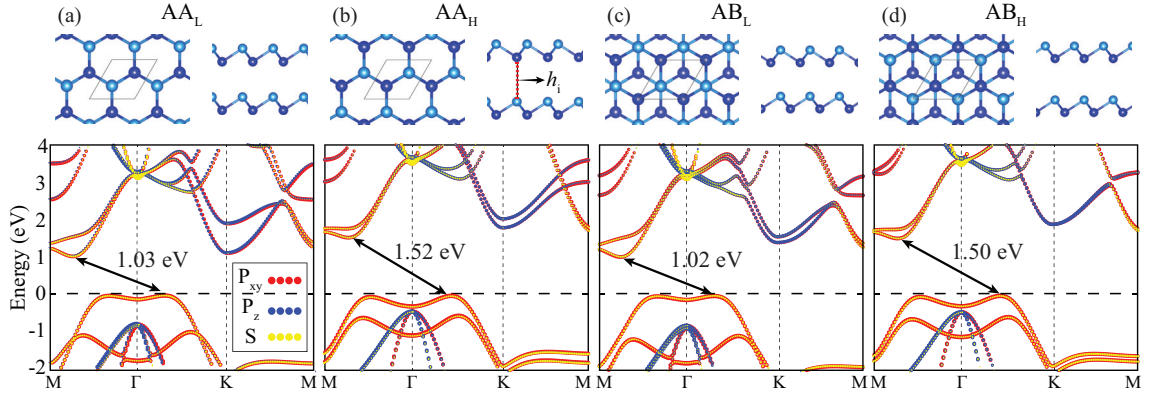


Figure 4.5. Top and side views of optimized geometric structures and the orbital projected electronic band dispersions of (a) AA_L , (b) AA_H , (c) AB_L , and (d) AB_H stacked bilayer blue phosphorene. Light and dark blue atoms show the upper and lower P atoms in each layer, respectively.

are 3.24 Å and 3.22 Å, respectively, the AA_H and AB_H configurations have almost 1 Å larger interlayer distances. (4.12 Å and 4.06 Å, respectively) In order to predict stabilities the cohesive energies of the bilayer configurations are also calculated and given in Table 4.2. AA_L stacking ordering is found to be energetically the most favorable configuration. Compared to the AA_H and AB_H stackings, reduction of the interlayer distances increases the interlayer interactions and therefore the cohesive energies in AA_L and AB_L stackings.

The orbital projected electronic band dispersions of different bilayer configurations (see the lower panel of Figure 4.5 (a)-(d)) exhibit similar indirect-gap characteristics with the monolayer blue phosphorene while the band gaps of bilayers are much lower. The indirect band gaps of AA_L , AA_H , AB_L , and AB_H are calculated to be 1.03, 1.52, 1.02, and 1.50 eV, respectively. It is clear that difference in the interlayer distances due to the stacking type plays an important role in determining the electronic band gap. As the interlayer distance increases the electronic band gap of bilayer increases. (see Table 4.2) Similar to the band structure of monolayer blue phosphorene, dominant configurations to the states of the valance and conduction band-edges emerge from the hybridized s and p_{xy} orbitals. In addition, the electronic band dispersions of AA_L (AA_H) and AB_L (AB_H) exhibit very similar behavior except for the K point in the BZ. Compared to the Bernal (AB) stacking, decreased symmetry in the AA stacking leads to splitting of conduction bands around the K point.

4.2.1.3. Excitonic Properties of Monolayer and Bilayer Blue Phosphorene

In this section, the excitonic properties of monolayer and various bilayer configurations of blue phosphorene are calculated by solving the Bethe-Salpeter equation on top of GW calculation.

Monolayer Blue Phosphorene

The quasiparticle energies of monolayer blue phosphorene are computed by performing G_0W_0 approximation on top of a DFT calculation and calculated band structure is shown in Figure 4.6 (a). The G_0W_0 approximation has significant effects on the electronic band structure and increases the indirect band gap of the monolayer blue phosphorene from 1.92 to 3.36 eV as the electron-electron interaction is enhanced due to weakly-screened Coulomb interaction in 2D structures. It is found that the inclusion of G_0W_0 correction not only shifts the band edges but also alters the band dispersions of the monolayer blue phosphorene. While the correction have a negligible effect on the dispersion of the conduction bands, the VBM is shifted toward the Γ point. Since the G_0W_0 correction is not uniform in the whole BZ, the scissor shift technique is not suitable for this material.

Although the calculation of the quasiparticle energy is sufficient to get an accurate electronic structure of a material, it is necessary to take into account the electron-hole interactions to obtain the correct optical spectrum. For this purpose, the BSE calculation is performed using the energy eigenvalues obtained from G_0W_0 calculation, this procedure is proven to be reliable in calculating highly-accurate optical properties of 2D materials. Imaginary part of dielectric function and oscillator strength of the optical transitions of monolayer blue phosphorene are shown in Figure 4.6 (b). Among several excitons located below the indirect band gap of the blue phosphorene, we only considered three main bound excitons, *A*, *B*, and *C*, located near the optical band edge with high oscillator strengths. The peak positions of *A*, *B*, and *C* excitons are found to be at 2.817, 3.213 and 3.251 eV, respectively. Our calculations show that the oscillator strength of *A* is much higher than that of *B* and *C* excitons. In Figure 4.6 (a), the band and the k-point compositions of the indicated excitons are shown. As seen in the figure, all three peaks originate from the same k-point in the BZ with the electronic band gap of 3.653 eV. The binding energies of *A*, *B*, and *C* excitons are calculated to be 0.836, 0.440, and 0.402 eV. Comparison with the projected band structure reveals that the these excitons are formed by

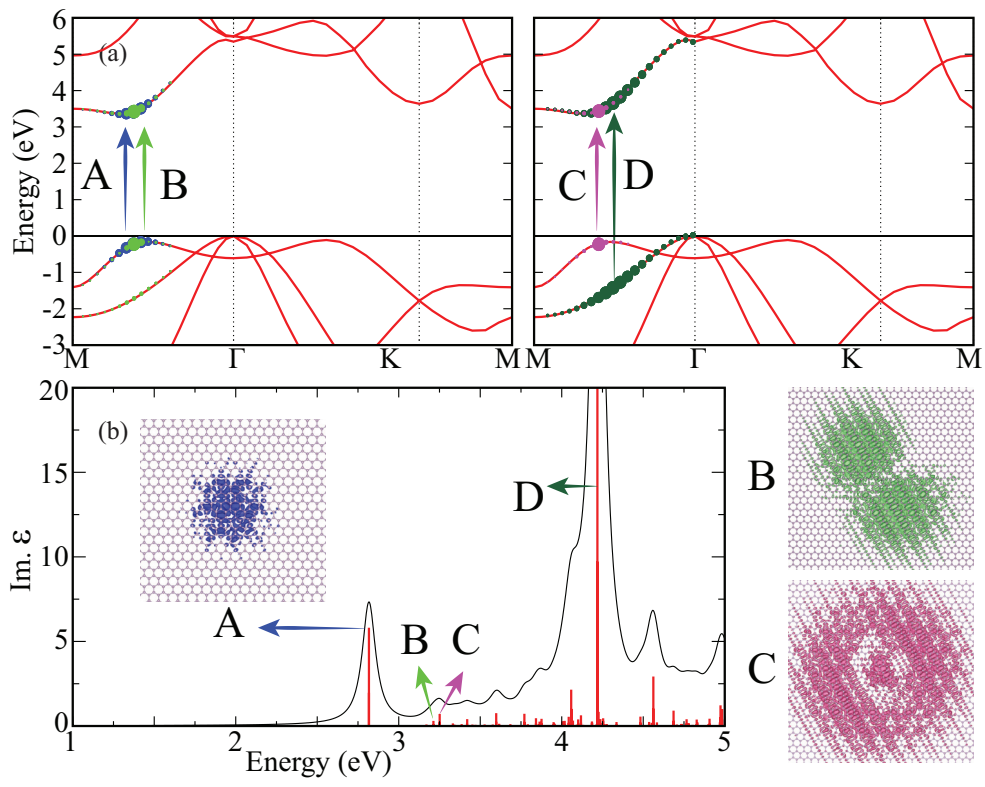


Figure 4.6. (a) Electronic band structures within G_0W_0 , (b) imaginary part of dielectric function and oscillator strengths of monolayer blue phosphorene. The insets show the real space exciton wave functions.

hybridized s and p_{xy} orbitals. In order to understand the excitonic properties in detail, the real-space excitonic wave functions of the material are calculated using the following formula

$$\Phi^S(\vec{x}_e, \vec{x}_h) = \sum_{k,v,c} A_{vck}^S \phi_{ck}(\vec{x}_e) \phi_{vk}^*(\vec{x}_h), \quad (4.5)$$

where S denotes the exciton and A_{vck}^S is the coefficient of the S exciton obtained by the diagonalization of the Bethe-Salpeter equation (Rohlfing and Louie, 2000). ϕ_{ck} and ϕ_{vk} are electron and hole wave functions, respectively. For real-space plots of A , B , and C excitons shown in the inset and side panel of Figure 4.6 (b), the hole position is fixed near the P atom in the center of the figures and the corresponding electron distributions are shown. It is clear that wavefunctions of A , B , and C excitons resemble the 1s, 2p, and 2s states of the hydrogen atom. As expected, the exciton A is more localized than the B and C excitons. Calculated exciton binding energies, peak positions and exciton wavefunctions of monolayer blue phosphorene are very similar to the previously reported values (Villegas *et al.*, 2016). Furthermore, the most prominent optical transition, D , is located at the 4.219 eV. Differing from the other excitons, the exciton D is formed by p_z orbitals and hybridized s - p_{xy} orbitals.

Bilayer Blue Phosphorene

The calculated indirect quasiparticle band gaps of AA_L , AA_H , AB_L , and AB_H stacked bilayers of blue phosphorene are 2.337, 2.965, 2.348, and 2.939 eV, respectively. Similar to the monolayer case, inclusion of G_0W_0 correction leads to ~ 1.44 eV increase in the band gap of the AA_H and AB_H stacked bilayers. However, the G_0W_0 correction for the AA_L and AB_L stacked bilayers (~ 1.33 eV) is lower than that of the monolayer. Therefore, increased interlayer interaction with the reduction of interlayer distance in AA_L and AB_L stacked bilayers causes an increase in the screening effect between the layers and a decrease in the band gap correction. Imaginary part of the dielectric function and the oscillator strength of the optical transitions of AA_L , AA_H , AB_L , and AB_H bilayers of blue phosphorene are shown in Figure 4.7 (a)-(d), respectively. Similar to the monolayer case, the optical band edge of bilayers consists of various optical transitions. For the sake of simplicity, we focus only on the in two main peaks (E_1 and E_2) near the optical band edge.

Imaginary part of the dielectric function of AA_L stacked bilayer is shown in the middle panel of Figure 4.7 (a). The first bright exciton of AA_L , AA_L^{E1} , is at 2.367 eV, which is located at the lowest energy compared to the bright excitons of the other stacking

types. The most prominent excitonic peak around the optical gap of AA_L , AA_L^{E2} , is located at 2.701 eV. The oscillator strength of the AA_L^{E1} is significantly lower than that of the AA_L^{E2} . The left panel of Figure 4.7 (a) shows that the AA_L^{E1} exciton emerges from the transitions from the highest valance band to the lowest conduction band, whereas the AA_L^{E2} is mainly due to the transitions from the highest valance band to the second conduction band. It also appears that a small contribution comes from the first conduction band to the AA_L^{E2} . Although the oscillator strength of the AA_L^{E1} and AA_L^{E2} excitons are quite different, their exciton binding energies are close to each other as 0.628 and 0.629 eV, respectively. In order to determine the character of excitons in all bilayer structures examined throughout this study, the real space exciton wave function is calculated by fixing the hole position near the P atom of the upper layer and shown in the inset of the middle panel of Figure 4.7. It is seen that the wave function of the AA_L^{E2} is more localized than AA_L^{E1} . The right panel of the Figure 4.7 (a) shows that wave functions of these excitons reside on both layers with similar density, hence they exhibit mixed interlayer exciton character in which intralayer and interlayer excitons are hybridized.

Differing from the AA_L stacking, the lowest exciton peak of the AA_H , AA_H^{E1} , is the most prominent peak around the optical gap. AA_H^{E1} (2.775 eV) and AA_H^{E2} (3.020 eV) peak positions are ~ 0.4 and ~ 0.3 eV higher than that of the AA_L^{E1} and AA_L^{E2} , respectively. The left panel of Figure 4.7 (b) shows that the AA_H^{E1} and AA_H^{E2} excitons are mainly composed of the transitions from the highest valance band to the second conduction band. It is seen from the middle panel of the Figure 4.7 (b) the oscillator strength of the AA_H^{E2} is almost half of that of the AA_H^{E1} . Top view of the wave functions of the AA_H^{E1} and AA_H^{E2} are illustrated in the same figure. While the exciton wave function of the AA_H^{E2} spreads widely to the two layers, the wave function of the AA_H^{E1} is more localized and the hole and electron are mostly located on the same layer (see the right panel of Figure 4.7 (b)). Since the hole is placed on the upper layer, compared to the AA_L configuration increased interlayer distance in the AA_H configuration leads to formation of mostly-intralayer excitons. As a result, the exciton binding energy of the AA_H^{E1} (0.633 eV) is much higher than that of the AA_H^{E2} (0.388 eV).

Imaginary part of the dielectric function of AB_L stacked bilayer blue phosphorene shows that the AB_L^{E1} and AB_L^{E2} excitons are located at 2.503 and 2.634 eV, respectively. As seen in the left panel of Figure 4.7 (c), while the AB_L^{E1} is composed of the transitions from the highest valance band to the lowest conduction band, the AB_L^{E2} consists of the transitions from the highest valance band to the first two conduction bands. The middle panel of Figure 4.7 (c) shows that the oscillator strength of the AB_L^{E1} is very weak com-

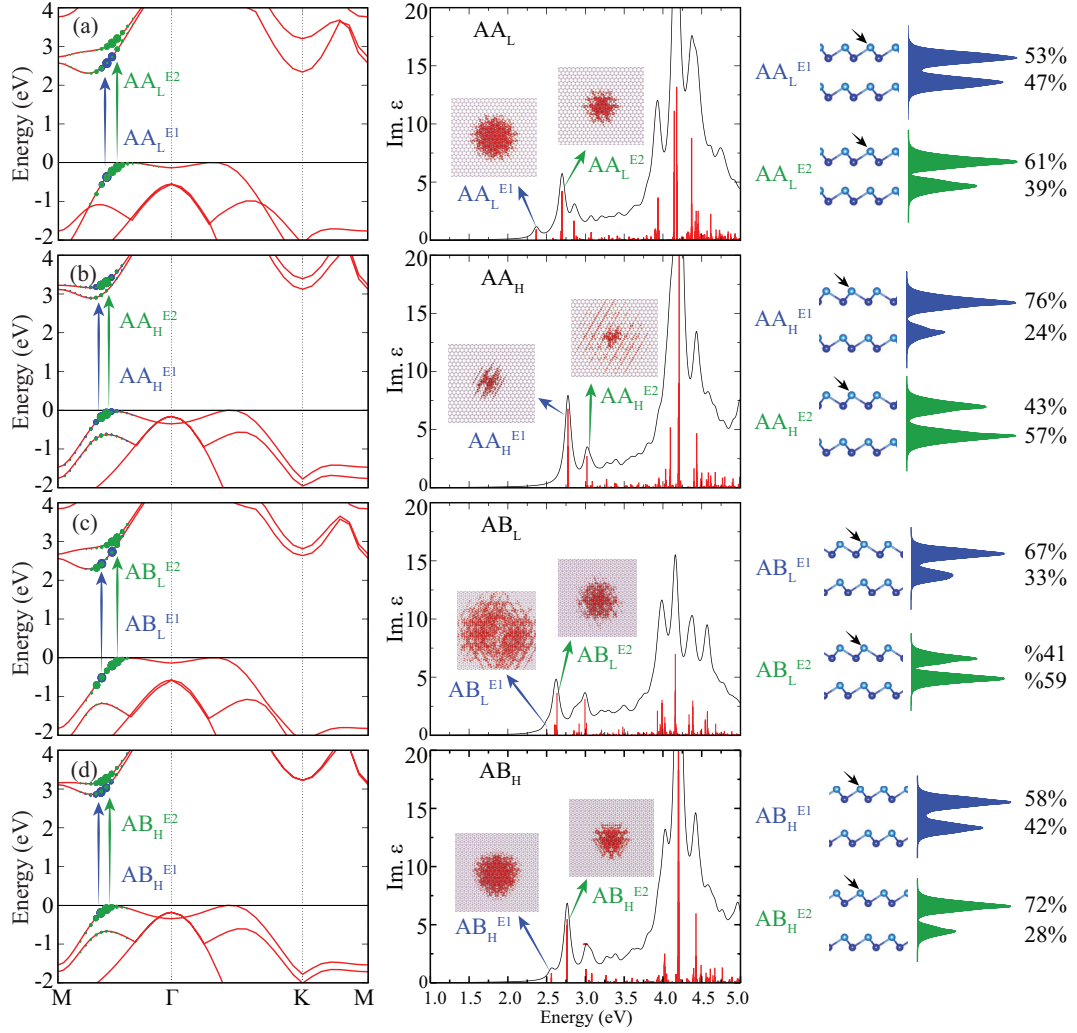


Figure 4.7. Electronic band dispersions within G_0W_0 (the left panels), imaginary part of dielectric functions, oscillator strengths, and top views of the real space exciton wave functions (the middle panels), the percentage of the excitonic wave function on each layer (the right panels) of (a) AA_L, (b) AA_H, (c) AB_L, and (d) AB_H stacked bilayer blue phosphorene. In all cases, the hole position is indicated by the black arrow.

pared to the AB_L^{E2} . It is clearly seen that a few excitations with similar oscillator strengths arise near the AB_L^{E2} exciton. Insets in the figure show that exciton wave function of the AB_L^{E2} is more localized than that of the AB_L^{E1} . The right panel of Figure 4.7 (c) shows that exciton wave functions of both AB_L^{E1} and AB_L^{E2} spread over the two layers and thus exhibit mixed interlayer character. The exciton binding energies of the AB_L^{E1} and AB_L^{E2} are calculated to be 0.488 and 0.644 eV, respectively.

It is found that while the first bright exciton of the AB_H , AB_H^{E1} , is at 2.561 eV, the most prominent peak around the optical band edge, AB_H^{E2} , is located at 2.765 eV. The left panel of Figure 4.7 (d) shows that the AB_H^{E1} is composed of the transitions from the highest valance band to the lowest conduction band. However, the AB_H^{E2} is composed of the transitions from the highest valance band to the second conduction band. As shown in the right panel of Figure 4.7 (d), AB_H^{E1} shows the mixed interlayer character, while AB_H^{E2} exhibits mostly the intralayer character. Exciton binding energies of the AB_H^{E1} and AB_H^{E2} are calculated to be 0.653 and 0.641 eV, respectively.

As a result, detailed analysis of excitonic peaks shows that different stacking types exhibit distinct optical spectrum near the optical band edge allowing to identification of the type of the stacking. The strong screening of the substrate does not significantly alter the optical spectrum of the ultra-thin materials as it similarly reduces the exciton binding energy and the quasiparticle band gap of 2D materials (Ugeda *et al.*, 2014). Therefore, we expect that the stacking type of the bilayer structure can be determined even in the presence of substrate. As expected, when the thickness of the material is increased from monolayer to bilayer, a significant decrease in exciton binding energies is determined. Our calculations show that, depending on the type of stacking, the prominent peaks near the optical band edge of the bilayer blue phosphorene are composed of mostly-intralayer or mixed interlayer excitons. In contrast to interlayer excitons of TMD heterostructures, the mixed interlayer excitons of bilayer blue phosphorene have high oscillator strength and high exciton binding energy due to the greater overlap of the electron and hole wave functions. Moreover, the mixed interlayer excitons of bilayer blue phosphorene have a longer recombination life time than the intralayer excitons of monolayer blue phosphorene because of the less overlap of electron and hole wave functions.

4.2.1.4. Conclusions

In conclusion, using first-principles calculations in the framework of MBPT we investigated the electronic and optical properties of monolayer and various bilayer config-

urations of blue phosphorene. Recently synthesized monolayer blue phosphorene exhibits a large indirect band gap. Electronic structure calculations revealed that band dispersions and the band gap of bilayer blue phosphorene are strongly depend on the stacking type.

In order to reveal excitonic properties of monolayer and bilayer configurations of blue phosphorene, the Bethe-Salpeter equation was solved on top of the G_0W_0 calculations. It was found that the lowest-energy exciton of the monolayer material is bright and has a very high exciton binding energy. It was calculated that the maximum exciton binding energy of the bilayer blue phosphorene (0.644 eV) is ~ 23 lower than binding energy of the lowest-energy exciton of the monolayer structure. Depending on the stacking types of bilayer blue phosphorene, mostly-intralayer and mixed interlayer excitons were determined near the optical band edge. Unlike the interlayer excitons of the TMD heterostructures, mixed interlayer excitons of bilayer blue phosphorene have high oscillator strengths. Thanks to its high and robust exciton binding energy and controllable optical spectra, ultra-thin blue phosphorene is a promising material for optoelectronic device applications.

CHAPTER 5

CONCLUSIONS

The present thesis focused on the study of electronic and optical properties of atomically thin layered materials by employing *ab initio* calculations in the framework of DFT and MBPT. In particular, typical *ab initio* calculations based on first principles DFT were systematically performed to examine the structural and electronic properties of these materials. On the other hand, when examining the optical properties of ultra-thin materials, GW and BSE approaches were used in order to take into account the high screening effects and excitonic properties, respectively, that dominate the optical spectrum in these materials. In this dissertation, we have used these techniques to design and predict the characteristic properties of a variety of 2D materials and to engineer these features using a variety of functionalization methods.

In the Chapter 3 we concentrated on the functionalization of the electronic properties of ultra-thin materials. Chemical functionalization of 2D materials is one of the most simplest methods to tune the electronic properties of a material. Firstly, we analyzed the structural and electronic properties of the pristine and defective structures of monolayer TiS_3 in detail. Total energy calculations showed that the most probable defect type of TiS_3 is the S atom vacancy. It was revealed that the S vacancy leads to an opening in the band gap, whereas Ti vacancy results in metallicity in monolayer TiS_3 . The oxidation calculations showed that while the atomic O and O_3 form strong bonds with TiS_3 surface, O_2 has low binding energy on the surface. The effects of hydrogenation on the structural and electronic properties of the CDW phase of monolayer TiSe_2 were investigated in another study. Our calculations showed that the periodic lattice distortions in the CDW phase provide the stability of the layer and the material has an HSE06-calculated direct band gap of 319 meV in this phase. Total energy and phonon calculations revealed that a structural phase transition occurs from the CDW phase to the T_d phase upon full hydrogenation. It was found that hydrogenation causes decreasing the electronic band gap of the material to 119 meV.

Dimensional reduction is the most important functionalization technique that leads to striking changes by causing the emergence of quantum effects in the fundamental properties of a material. We investigated the structural and electronic properties of CsPb_2Br_5 crystals, and how these properties are affected by dimensional crossover. It was revealed

that CsPb_2Br_5 crystal is an indirect band gap semiconductor with a band gap of 2.41 eV within LDA+SOC. It was found that Cs atoms have no effect on the electronic structure, but their presence is essential for the formation of stable CsPb_2Br_5 crystals. The calculated vibrational spectra of the crystal revealed that there are two dynamically stable phases of single-layer CsPb_2Br_5 . Both of the single-layer structures show indirect semiconducting character with a band gap of ~ 2.54 eV within LDA+SOC. Moreover, the modification of the electronic properties of single-layer CsPb_2Br_5 upon formation of vacancy defects was also investigated. In another study, the layer-dependent structural and electronic properties of 1T phase of PtSe_2 were examined in detail. Electronic structure calculations showed that the band gap rapidly decreased from 1.17 eV to 0.19 eV when the material thickness increased from one layer to two layers. It was also found that PtSe_2 crystals having a thickness larger than two layers all exhibit metallic character. Moreover, we revealed that electronic structure of 1T- PtSe_2 monolayer change negligibly even at high biaxial strains revealing the robust semiconductor character of the material.

Since the dimensional reduction increases the sensitivity of ultra-thin materials against environmental effects, external strain can cause significant changes in the fundamental properties of these materials. In this context, we first investigated the electronic and magnetic properties of monolayer $\alpha\text{-RuCl}_3$ under in-plane strain. While the magnetic ordering of the ground state is ZZ-AFM, FM phase has a few meV per conventional cell higher energy than the ground state. Both ZZ-AFM and FM phases are indirect gap semiconductors. It was found that the magnetic ground state of the material experiences a phase transition from ZZ-AFM to FM upon certain applied strains. Although the valence and conduction band edges of ZZ-AFM and FM phases show various modifications, the electronic band gaps remain almost unchanged under external strains. Secondly, we investigated variation of the electronic properties of single-layer CdTe crystal under out-of-plane and in-plane strains. It was shown that single-layer CdTe has a direct band gap of 1.42 eV (GGA) at the Γ point and both electrons and holes in the material possess anisotropic in-plane masses and mobilities. The band gap value of the material exhibits strain-dependent anisotropic variation, but shows a rapid increase under perpendicular compression. However, the direct band gap semiconducting behavior of the single-layer CdTe remains unchanged under all types of applied strain.

In the Chapter 4 we mainly focused on the functionalization of the optical properties of ultra-thin materials. First, we investigated thickness-dependence of the electronic and optical properties orthorhombic CsPbI_3 perovskite crystals. Our calculations revealed that only bilayers and monolayers of CsPbI_3 crystal with Cs-I terminated surfaces may

form stable thin structures. It was found that regardless of the thickness, the material shows a direct band gap semiconducting character. However, as the thickness of the perovskite decreases the energy band gap increases significantly. Our calculations on the optical response of the structures showed that reduction in the thickness also leads to the blue shift of the absorption edge of the optical spectra. Moreover, it was calculated that the reflectivity and transmissivity of the material can be drastically modified by tuning the thickness. Lastly, we examined the electronic and optical properties of ultra-thin blue phosphorene. Since the screening and excitonic effects dominate the optical spectrum of this material, the electronic and optical properties were calculated by employing first principles calculations based on DFT and MBPT. The Bethe-Salpeter equation was solved on top of the G_0W_0 to calculate the binding energies, spectral positions, and band decomposition of excitons of monolayer and bilayer configurations. It was found that the lowest-energy exciton of the monolayer material is bright and has a very high exciton binding energy. As expected, when the thickness of the material was increased from monolayer to bilayer, a significant reduction in exciton binding energies was found. Moreover, mixed interlayer and mostly-intralayer excitons with quite high binding energies were obtained in the bilayer blue phosphorene.

REFERENCES

- Alfè, D. (2009). Phon: A program to calculate phonons using the small displacement method. *Computer Physics Communications* 180(12), 2622–2633.
- Amirtharaj, P. and F. H. Pollak (1984). Raman scattering study of the properties and removal of excess Te on CdTe surfaces. *Applied Physics Letters* 45(7), 789–791.
- Ataca, C., H. Sahin, and S. Ciraci (2012). Stable, single-layer MX_2 transition-metal oxides and dichalcogenides in a honeycomb-like structure. *The Journal of Physical Chemistry C* 116(16), 8983–8999.
- Bacaksiz, C. and H. Sahin (2016). Single layer PbI_2 : hydrogenation-driven reconstructions. *RSC advances* 6(92), 89708–89714.
- Bacaksiz, C., R. T. Senger, and H. Sahin (2017). Ultra-thin $ZnSe$: Anisotropic and flexible crystal structure. *Applied Surface Science* 409, 426–430.
- Bertolazzi, S., J. Brivio, and A. Kis (2011). Stretching and breaking of ultrathin MoS_2 . *ACS nano* 5(12), 9703–9709.
- Bissett, M. A., S. Konabe, S. Okada, M. Tsuji, and H. Ago (2013). Enhanced chemical reactivity of graphene induced by mechanical strain. *ACS nano* 7(11), 10335–10343.
- Blöchl, P. E. (1994, Dec). Projector augmented-wave method. *Phys. Rev. B* 50, 17953–17979.
- Bonilla, S. and E. A. Dalchiele (1991). Electrochemical deposition and characterization of CdTe polycrystalline thin films. *Thin solid films* 204(2), 397–403.
- Brattas, L. and A. Kjekshus (1972). On the properties of compounds with the $ZrSe_3$ type structure. *Acta Chem. Scand.* 26(9), 3441–3449.
- Castellanos-Gomez, A., L. Vicarelli, E. Prada, J. O. Island, K. Narasimha-Acharya, S. I. Blanter, D. J. Groenendijk, M. Buscema, G. A. Steele, J. Alvarez, *et al.* (2014). Isolation and characterization of few-layer black phosphorus. *2D Materials* 1(2), 025001.

- Ceperley, D. M. and B. Alder (1980a). Ground state of the electron gas by a stochastic method. *Physical Review Letters* 45(7), 566.
- Ceperley, D. M. and B. J. Alder (1980b, Aug). Ground state of the electron gas by a stochastic method. *Phys. Rev. Lett.* 45, 566–569.
- Chen, P., Y.-H. Chan, X.-Y. Fang, Y. Zhang, M.-Y. Chou, S.-K. Mo, Z. Hussain, A.-V. Fedorov, and T.-C. Chiang (2015). Charge density wave transition in single-layer titanium diselenide. *Nature communications* 6, 8943.
- Chen, Y., P. Cui, X. Ren, C. Zhang, C. Jin, Z. Zhang, and C.-K. Shih (2017). Fabrication of mose 2 nanoribbons via an unusual morphological phase transition. *Nature communications* 8, 15135.
- Chia, X., A. Adriano, P. Lazar, Z. Sofer, J. Luxa, and M. Pumera (2016). Layered platinum dichalcogenides (pts2, ptse2, and ppte2) electrocatalysis: monotonic dependence on the chalcogen size. *Advanced Functional Materials* 26(24), 4306–4318.
- Cho, H., S.-H. Jeong, M.-H. Park, Y.-H. Kim, C. Wolf, C.-L. Lee, J. H. Heo, A. Sadhanala, N. Myoung, S. Yoo, *et al.* (2015). Overcoming the electroluminescence efficiency limitations of perovskite light-emitting diodes. *Science* 350(6265), 1222–1225.
- Choi, J.-H., P. Cui, H. Lan, and Z. Zhang (2015). Linear scaling of the exciton binding energy versus the band gap of two-dimensional materials. *Physical review letters* 115(6), 066403.
- Ciarrocchi, A., A. Avsar, D. Ovchinnikov, and A. Kis (2018). Thickness-modulated metal-to-semiconductor transformation in a transition metal dichalcogenide. *Nature communications* 9(1), 919.
- Coleman, J. N., M. Lotya, A. O'Neill, S. D. Bergin, P. J. King, U. Khan, K. Young, A. Gaucher, S. De, R. J. Smith, *et al.* (2011). Two-dimensional nanosheets produced by liquid exfoliation of layered materials. *Science* 331(6017), 568–571.
- Conley, H. J., B. Wang, J. I. Ziegler, R. F. Haglund Jr, S. T. Pantelides, and K. I. Bolotin (2013). Bandgap engineering of strained monolayer and bilayer mos2. *Nano letters* 13(8), 3626–3630.

- Dai, J. and X. C. Zeng (2014). Bilayer phosphorene: effect of stacking order on bandgap and its potential applications in thin-film solar cells. *The journal of physical chemistry letters* 5(7), 1289–1293.
- Das, S., W. Zhang, M. Demarteau, A. Hoffmann, M. Dubey, and A. Roelofs (2014). Tunable transport gap in phosphorene. *Nano letters* 14(10), 5733–5739.
- Dastidar, S., C. J. Hawley, A. D. Dillon, A. D. Gutierrez-Perez, J. E. Spanier, and A. T. Fafarman (2017). Quantitative phase-change thermodynamics and metastability of perovskite-phase cesium lead iodide. *The journal of physical chemistry letters* 8(6), 1278–1282.
- Deilmann, T. and K. S. Thygesen (2018). Interlayer excitons with large optical amplitudes in layered van der waals materials. *Nano letters* 18(5), 2984–2989.
- Di Salvo, F. J., D. E. Moncton, and J. V. Waszczak (1976, Nov). Electronic properties and superlattice formation in the semimetal tise_2 . *Phys. Rev. B* 14, 4321–4328.
- Diamant, R., L. Ponce, M. Fernández, and E. Jiménez (1998). Plasma dynamics and its relationship with thin film properties of cdte via pulsed laser deposition (pld). *Applied Physics B* 66(5), 639–643.
- Dirac, P. A. (1930). Note on exchange phenomena in the thomas atom. In *Proceedings of the Cambridge Philosophical Society*, Volume 26, pp. 376.
- Dou, L., A. B. Wong, Y. Yu, M. Lai, N. Kornienko, S. W. Eaton, A. Fu, C. G. Bischak, J. Ma, T. Ding, *et al.* (2015). Atomically thin two-dimensional organic-inorganic hybrid perovskites. *Science* 349(6255), 1518–1521.
- Dou, L., Y. M. Yang, J. You, Z. Hong, W.-H. Chang, G. Li, and Y. Yang (2014). Solution-processed hybrid perovskite photodetectors with high detectivity. *Nature communications* 5, 5404.
- Du, J., P. Song, L. Fang, T. Wang, Z. Wei, J. Li, and C. Xia (2018). Elastic, electronic and optical properties of the two-dimensional ptx_2 ($x = \text{s}, \text{se}, \text{and te}$) monolayer. *Applied Surface Science* 435, 476–482.

- Elias, D. C., R. R. Nair, T. Mohiuddin, S. Morozov, P. Blake, M. Halsall, A. C. Ferrari, D. Boukhvalov, M. Katsnelson, A. Geim, *et al.* (2009). Control of graphene's properties by reversible hydrogenation: evidence for graphane. *Science* 323(5914), 610–613.
- Eperon, G. E., G. M. Paterno, R. J. Sutton, A. Zampetti, A. A. Haghghirad, F. Cacialli, and H. J. Snaith (2015). Inorganic caesium lead iodide perovskite solar cells. *Journal of Materials Chemistry A* 3(39), 19688–19695.
- Ergen, O., S. M. Gilbert, T. Pham, S. J. Turner, M. T. Z. Tan, M. A. Worsley, and A. Zettl (2017). Graded bandgap perovskite solar cells. *Nature materials* 16(5), 522.
- Ezawa, M. (2007). Metallic graphene nanodisks: Electronic and magnetic properties. *Physical Review B* 76(24), 245415.
- Fang, X.-Y., H. Hong, P. Chen, and T.-C. Chiang (2017, May). X-ray study of the charge-density-wave transition in single-layer TiSe_2 . *Phys. Rev. B* 95, 201409.
- Ferekides, C., U. Balasubramanian, R. Mamazza, V. Viswanathan, H. Zhao, and D. Morel (2004). Cdte thin film solar cells: device and technology issues. *Solar Energy* 77(6), 823–830.
- Ferrer, I., J. Ares, J. Clamagirand, M. Barawi, and C. Sánchez (2013). Optical properties of titanium trisulphide (tis3) thin films. *Thin Solid Films* 535, 398–401.
- Ferrer, I., M. Maciá, V. Carcelén, J. Ares, and C. Sánchez (2012). On the photoelectrochemical properties of tis3 films. *Energy Procedia* 22, 48–52.
- Feynman, R. P. (1939, Aug). Forces in molecules. *Phys. Rev.* 56, 340–343.
- Finkman, E. and B. Fisher (1984). Electrical transport measurements in tis3. *Solid state communications* 50(1), 25–28.
- Fletcher, J., W. Gardner, A. Fox, and G. Topping (1967). X-ray, infrared, and magnetic studies of α - and β -ruthenium trichloride. *Journal of the Chemical Society A: Inorganic, Physical, Theoretical*, 1038–1045.
- Fock, V. (1930). *Z. physik* 61, 126 (1930); jc slater. *Phys. Rev* 35, 210.

- Fox, M. (2002). Optical properties of solids.
- Fu, Y., H. Zhu, C. C. Stoumpos, Q. Ding, J. Wang, M. G. Kanatzidis, X. Zhu, and S. Jin (2016). Broad wavelength tunable robust lasing from single-crystal nanowires of cesium lead halide perovskites (cspb_x3, x= cl, br, i). *ACS nano* 10(8), 7963–7972.
- Furusest, S., L. Brattas, and A. Kjekshus (1975). On the crystal structures of tis₃, zrs₃, zrse₃, zrte₃, hfs₃, and hfse₃. *Acta Chem. Scand. Ser. A* 29, 623–631.
- Geim, A. K. and K. S. Novoselov (2010). The rise of graphene. In *Nanoscience and Technology: A Collection of Reviews from Nature Journals*, pp. 11–19. World Scientific.
- Ghorbani-Asl, M., A. N. Enyashin, A. Kuc, G. Seifert, and T. Heine (2013). Defect-induced conductivity anisotropy in mos₂ monolayers. *Physical Review B* 88(24), 245440.
- Ghosh, B., S. Nahas, S. Bhowmick, and A. Agarwal (2015). Electric field induced gap modification in ultrathin blue phosphorus. *Physical Review B* 91(11), 115433.
- Giannozzi, P., S. Baroni, N. Bonini, M. Calandra, R. Car, C. Cavazzoni, D. Ceresoli, G. L. Chiarotti, M. Cococcioni, I. Dabo, *et al.* (2009). Quantum espresso: a modular and open-source software project for quantum simulations of materials. *Journal of physics: Condensed matter* 21(39), 395502.
- Gogotsi, Y. (2015). Chemical vapour deposition: transition metal carbides go 2d. *Nature materials* 14(11).
- Golor, M., S. Wessel, and M. J. Schmidt (2014). Quantum nature of edge magnetism in graphene. *Physical review letters* 112(4), 046601.
- Gong, C., H. Zhang, W. Wang, L. Colombo, R. M. Wallace, and K. Cho (2013). Band alignment of two-dimensional transition metal dichalcogenides: Application in tunnel field effect transistors. *Applied Physics Letters* 103(5), 053513.
- Gorlova, I., V. Y. Pokrovskii, S. Zybtssev, A. Titov, and V. Timofeev (2010). Features of the conductivity of the quasi-one-dimensional compound tis₃. *Journal of Experimental and Theoretical Physics* 111(2), 298–303.

- Gorlova, I., S. Zybtssev, V. Y. Pokrovskii, N. Bolotina, I. Verin, and A. Titov (2012). Nonlinear conductivity of quasi-one-dimensional layered compound TiS_3 . *Physica B: Condensed Matter* 407(11), 1707–1710.
- Grancini, G., C. Roldán-Carmona, I. Zimmermann, E. Mosconi, X. Lee, D. Martineau, S. Narbey, F. Oswald, F. De Angelis, M. Graetzel, *et al.* (2017). One-year stable perovskite solar cells by 2d/3d interface engineering. *Nature communications* 8, 15684.
- Grätzel, M. (2014). The light and shade of perovskite solar cells. *Nature materials* 13(9), 838.
- Green, M. A., A. Ho-Baillie, and H. J. Snaith (2014). The emergence of perovskite solar cells. *Nature photonics* 8(7), 506.
- Grimme, S. (2006). Semiempirical gga-type density functional constructed with a long-range dispersion correction. *Journal of computational chemistry* 27(15), 1787–1799.
- Groiss, H., G. Hesser, W. Heiss, F. Schäffler, R. Leitsmann, F. Bechstedt, K. Koike, and M. Yano (2009). Coherent {001} interfaces between rocksalt and zinc-blende crystal structures. *Physical Review B* 79(23), 235331.
- Gui, G., J. Li, and J. Zhong (2008). Band structure engineering of graphene by strain: first-principles calculations. *Physical Review B* 78(7), 075435.
- Guilmeau, E., D. Berthebaud, P. R. Misse, S. Heßbert, O. I. Lebedev, D. Chateigner, C. Martin, and A. Maignan (2014). ZrSe_3 -type variant of TiS_3 : Structure and thermoelectric properties. *Chemistry of Materials* 26(19), 5585–5591.
- Guo, G. and W. Liang (1986). The electronic structures of platinum dichalcogenides: PtS_2 , PtSe_2 and PtTe_2 . *Journal of Physics C: Solid State Physics* 19(7), 995.
- Guo, L., S. Zhang, W. Feng, G. Hu, and W. Li (2013). A first-principles study on the structural, elastic, electronic, optical, lattice dynamical, and thermodynamic properties of zinc-blende CdX ($X = \text{S}, \text{Se}, \text{Te}$). *Journal of Alloys and Compounds* 579, 583–593.
- Gupta, A., V. Parikh, and A. D. Compaan (2006). High efficiency ultra-thin sputtered CdTe solar cells. *Solar Energy Materials and Solar Cells* 90(15), 2263–2271.

- Han, N., N. Gao, and J. Zhao (2017). Initial growth mechanism of blue phosphorene on au (111) surface. *The Journal of Physical Chemistry C* 121(33), 17893–17899.
- Hartree, D. R. (1928). The wave mechanics of an atom with a non-coulomb central field. part i. theory and methods. In *Mathematical Proceedings of the Cambridge Philosophical Society*, Volume 24, pp. 89–110. Cambridge Univ Press.
- He, J., K. Hummer, and C. Franchini (2014). Stacking effects on the electronic and optical properties of bilayer transition metal dichalcogenides mos₂, mose₂, ws₂, and wse₂. *Physical Review B* 89(7), 075409.
- He, K., C. Poole, K. F. Mak, and J. Shan (2013). Experimental demonstration of continuous electronic structure tuning via strain in atomically thin mos₂. *Nano letters* 13(6), 2931–2936.
- He, X., Y. Qiu, and S. Yang (2017). Fully-inorganic trihalide perovskite nanocrystals: A new research frontier of optoelectronic materials. *Advanced Materials* 29(32), 1700775.
- Hedin, L. and S. Lundqvist (1970). Effects of electron-electron and electron-phonon interactions on the one-electron states of solids. In *Solid state physics*, Volume 23, pp. 1–181. Elsevier.
- Hellmann, H. (1937). *Einführung in die quantenchemie: Texte imprimé*. F. Deuticke.
- Henkelman, G., A. Arnaldsson, and H. Jónsson (2006). A fast and robust algorithm for bader decomposition of charge density. *Computational Materials Science* 36(3), 354–360.
- Hohenberg, P. and W. Kohn (1964, Nov). Inhomogeneous electron gas. *Phys. Rev.* 136, B864–B871.
- Horzum, S., H. Sahin, S. Cahangirov, P. Cudazzo, A. Rubio, T. Serin, and F. Peeters (2013). Phonon softening and direct to indirect band gap crossover in strained single-layer mose₂. *Physical Review B* 87(12), 125415.
- Huang, B., G. Clark, E. Navarro-Moratalla, D. R. Klein, R. Cheng, K. L. Seyler, D. Zhong, E. Schmidgall, M. A. McGuire, D. H. Cobden, *et al.* (2017). Layer-dependent ferromagnetism in a van der waals crystal down to the monolayer limit.

Nature 546(7657), 270.

Island, J. O., M. Barawi, R. Biele, A. Almazán, J. M. Clamagirand, J. R. Ares, C. Sánchez, H. S. van der Zant, J. V. Álvarez, R. D'Agosta, *et al.* (2015). Tis3 transistors with tailored morphology and electrical properties. *Advanced Materials* 27(16), 2595–2601.

Island, J. O., M. Buscema, M. Barawi, J. M. Clamagirand, J. R. Ares, C. Sánchez, I. J. Ferrer, G. A. Steele, H. S. van der Zant, and A. Castellanos-Gomez (2014). Ultrahigh photoresponse of few-layer tis3 nanoribbon transistors. *Advanced Optical Materials* 2(7), 641–645.

Ismail-Beigi, S. (2006). Truncation of periodic image interactions for confined systems. *Physical Review B* 73(23), 233103.

Ison, V., A. R. Rao, and V. Dutta (2009). Characterization of spray deposited cdte films grown under different ambient conditions. *Solid State Sciences* 11(11), 2003–2007.

Ithurria, S., M. Tessier, B. Mahler, R. Lobo, B. Dubertret, and A. L. Efros (2011). Colloidal nanoplatelets with two-dimensional electronic structure. *Nature materials* 10(12), 936.

İyikanat, F., B. Akbali, J. Kang, R. T. Senger, Y. Selamet, and H. Sahin (2017). Stable ultra-thin cdte crystal: A robust direct gap semiconductor. *Journal of Physics: Condensed Matter* 29(48), 485302.

Iyikanat, F., H. Sahin, R. Senger, and F. Peeters (2014). Ag and au atoms intercalated in bilayer heterostructures of transition metal dichalcogenides and graphene. *APL materials* 2(9), 092801.

İyikanat, F., E. Sari, and H. Sahin (2017). Thinning cspb 2 br 5 perovskite down to monolayers: Cs-dependent stability. *Physical Review B* 96(15), 155442.

Jeon, N. J., J. H. Noh, W. S. Yang, Y. C. Kim, S. Ryu, J. Seo, and S. I. Seok (2015). Compositional engineering of perovskite materials for high-performance solar cells. *Nature* 517(7535), 476.

Jiang, J.-W. and H. S. Park (2014). Negative poisson's ratio in single-layer black phosphorus. *Nature communications* 5, 4727.

- Jiang, Z., Z. Liu, Y. Li, and W. Duan (2017). Scaling universality between band gap and exciton binding energy of two-dimensional semiconductors. *Physical review letters* 118(26), 266401.
- Johari, P. and V. B. Shenoy (2012). Tuning the electronic properties of semiconducting transition metal dichalcogenides by applying mechanical strains. *ACS nano* 6(6), 5449–5456.
- Jung, J. and A. MacDonald (2009). Carrier density and magnetism in graphene zigzag nanoribbons. *Physical Review B* 79(23), 235433.
- Kandemir, A., F. Iyikanat, and H. Sahin (2019). Monitoring the crystal orientation of black-arsenic via vibrational spectra. *Journal of Materials Chemistry C* 7(5), 1228–1236.
- Kang, J. and L.-W. Wang (2017). High defect tolerance in lead halide perovskite cspbbr₃. *The journal of physical chemistry letters* 8(2), 489–493.
- Khazaei, M., M. Arai, T. Sasaki, M. Estili, and Y. Sakka (2014). Two-dimensional molybdenum carbides: potential thermoelectric materials of the mxene family. *Physical Chemistry Chemical Physics* 16(17), 7841–7849.
- Kim, H.-S., A. Catuneanu, H.-Y. Kee, *et al.* (2015). Kitaev magnetism in honeycomb rucl₃ with intermediate spin-orbit coupling. *Physical Review B* 91(24), 241110.
- Kim, K.-C., H. J. Kim, S.-H. Suh, M. Carmody, S. Sivananthan, and J.-S. Kim (2010). Metalorganic chemical vapor deposition of cdte (133) epilayers on si (211) substrates. *Journal of Electronic Materials* 39(7), 863–867.
- Kim, K. K., A. Hsu, X. Jia, S. M. Kim, Y. Shi, M. Hofmann, D. Nezich, J. F. Rodriguez-Nieva, M. Dresselhaus, T. Palacios, *et al.* (2011). Synthesis of monolayer hexagonal boron nitride on cu foil using chemical vapor deposition. *Nano letters* 12(1), 161–166.
- Kim, Y.-H., H. Cho, J. H. Heo, T.-S. Kim, N. Myoung, C.-L. Lee, S. H. Im, and T.-W. Lee (2015). Multicolored organic/inorganic hybrid perovskite light-emitting diodes. *Advanced materials* 27(7), 1248–1254.

- Kliche, G. (1985). Far-infrared and x-ray investigations of the mixed platinum dichalcogenides PtS_2 - PtSe_2 , PtSe_2 - PtTe_2 , and PtS_2 - PtTe_2 . *Journal of Solid State Chemistry* 56(1), 26–31.
- Kohn, W. (1959, May). Image of the fermi surface in the vibration spectrum of a metal. *Phys. Rev. Lett.* 2, 393–394.
- Kohn, W. and L. J. Sham (1965, Nov). Self-consistent equations including exchange and correlation effects. *Phys. Rev.* 140, A1133–A1138.
- Komsa, H.-P., J. Kotakoski, S. Kurasch, O. Lehtinen, U. Kaiser, and A. V. Krasheninnikov (2012, Jul). Two-dimensional transition metal dichalcogenides under electron irradiation: Defect production and doping. *Phys. Rev. Lett.* 109, 035503.
- Kovalenko, M. V., L. Protesescu, and M. I. Bodnarchuk (2017). Properties and potential optoelectronic applications of lead halide perovskite nanocrystals. *Science* 358(6364), 745–750.
- Krasheninnikov, A., P. Lehtinen, A. S. Foster, P. Pyykkö, and R. M. Nieminen (2009). Embedding transition-metal atoms in graphene: structure, bonding, and magnetism. *Physical review letters* 102(12), 126807.
- Kresse, G. and J. Furthmüller (1996, Oct). Efficient iterative schemes for ab initio total-energy calculations using a plane-wave basis set. *Phys. Rev. B* 54, 11169–11186.
- Kresse, G. and J. Hafner (1993, Jan). Ab initio molecular dynamics for liquid metals. *Phys. Rev. B* 47, 558–561.
- Kresse, G. and D. Joubert (1999, Jan). From ultrasoft pseudopotentials to the projector augmented-wave method. *Phys. Rev. B* 59, 1758–1775.
- Kubota, Y., H. Tanaka, T. Ono, Y. Narumi, and K. Kindo (2015). Successive magnetic phase transitions in α - RuCl_3 : Xy-like frustrated magnet on the honeycomb lattice. *Physical Review B* 91(9), 094422.
- Kulbak, M., D. Cahen, and G. Hodes (2015). How important is the organic part of lead halide perovskite photovoltaic cells? efficient CsPbBr_3 cells. *The journal of physical*

chemistry letters 6(13), 2452–2456.

Lee, C., X. Wei, J. W. Kysar, and J. Hone (2008). Measurement of the elastic properties and intrinsic strength of monolayer graphene. *science* 321(5887), 385–388.

Lee, C., H. Yan, L. E. Brus, T. F. Heinz, J. Hone, and S. Ryu (2010). Anomalous lattice vibrations of single- and few-layer mos₂. *ACS nano* 4(5), 2695–2700.

Lee, J., J. Huang, B. G. Sumpter, and M. Yoon (2017). Strain-engineered optoelectronic properties of 2d transition metal dichalcogenide lateral heterostructures. *2D Materials* 4(2), 021016.

Lee, M. M., J. Teuscher, T. Miyasaka, T. N. Murakami, and H. J. Snaith (2012). Efficient hybrid solar cells based on meso-superstructured organometal halide perovskites. *Science* 338(6107), 643–647.

Levy, N., S. Burke, K. Meaker, M. Panlasigui, A. Zettl, F. Guinea, A. C. Neto, and M. Crommie (2010). Strain-induced pseudo-magnetic fields greater than 300 tesla in graphene nanobubbles. *Science* 329(5991), 544–547.

Li, G., H. Wang, Z. Zhu, Y. Chang, T. Zhang, Z. Song, and Y. Jiang (2016). Shape and phase evolution from cspbbr₃ perovskite nanocubes to tetragonal cspb₂br₅ nanosheets with an indirect bandgap. *Chemical Communications* 52(75), 11296–11299.

Li, L., W. Wang, Y. Chai, H. Li, M. Tian, and T. Zhai (2017). Few-layered pts₂ phototransistor on h-bn with high gain. *Advanced Functional Materials* 27(27), 1701011.

Li, X., F. Cao, D. Yu, J. Chen, Z. Sun, Y. Shen, Y. Zhu, L. Wang, Y. Wei, Y. Wu, *et al.* (2017). All inorganic halide perovskites nanosystem: synthesis, structural features, optical properties and optoelectronic applications. *Small* 13(9), 1603996.

Li, X., Y. Wu, S. Zhang, B. Cai, Y. Gu, J. Song, and H. Zeng (2016). Cspb₃ quantum dots for lighting and displays: room-temperature synthesis, photoluminescence superiorities, underlying origins and white light-emitting diodes. *Advanced Functional Materials* 26(15), 2435–2445.

Liu, H., A. T. Neal, Z. Zhu, Z. Luo, X. Xu, D. Tománek, and P. D. Ye (2014). Phosphorene:

- an unexplored 2d semiconductor with a high hole mobility. *ACS nano* 8(4), 4033–4041.
- Liu, J., Y. Xue, Z. Wang, Z.-Q. Xu, C. Zheng, B. Weber, J. Song, Y. Wang, Y. Lu, Y. Zhang, *et al.* (2016). Two-dimensional $\text{CH}_3\text{NH}_3\text{PbI}_3$ perovskite: Synthesis and optoelectronic application. *ACS nano* 10(3), 3536–3542.
- Liu, L., X. Wu, X. Liu, and P. K. Chu (2015). Strain-induced band structure and mobility modulation in graphitic blue phosphorus. *Applied Surface Science* 356, 626–630.
- Luo, G., X. Qian, H. Liu, R. Qin, J. Zhou, L. Li, Z. Gao, E. Wang, W.-N. Mei, J. Lu, *et al.* (2011). Quasiparticle energies and excitonic effects of the two-dimensional carbon allotrope graphdiyne: Theory and experiment. *Physical Review B* 84(7), 075439.
- Ma, Y., Y. Dai, M. Guo, C. Niu, Y. Zhu, and B. Huang (2012). Evidence of the existence of magnetism in pristine Vx_2 monolayers ($x = \text{s, se}$) and their strain-induced tunable magnetic properties. *ACS nano* 6(2), 1695–1701.
- Mahabaduge, H., W. Rance, J. Burst, M. Reese, D. Meysing, C. Wolden, J. Li, J. Beach, T. Gessert, W. Metzger, *et al.* (2015). High-efficiency, flexible CdTe solar cells on ultra-thin glass substrates. *Applied Physics Letters* 106(13), 133501.
- Majumder, M., M. Schmidt, H. Rosner, A. Tsirlin, H. Yasuoka, and M. Baenitz (2015). Anisotropic Ru^{3+} d^5 magnetism in the α - RuCl_3 honeycomb system: Susceptibility, specific heat, and zero-field nmr. *Physical Review B* 91(18), 180401.
- Mak, K. F., C. Lee, J. Hone, J. Shan, and T. F. Heinz (2010). Atomically thin MoS_2 : a new direct-gap semiconductor. *Physical review letters* 105(13), 136805.
- Marini, A., C. Hogan, M. Grüning, and D. Varsano (2009). Yambo: an ab initio tool for excited state calculations. *Computer Physics Communications* 180(8), 1392–1403.
- Marronnier, A., G. Roma, S. Boyer-Richard, L. Pedesseau, J.-M. Jancu, Y. Bonnassieux, C. Katan, C. C. Stoumpos, M. G. Kanatzidis, and J. Even (2018). Anharmonicity and disorder in the black phases of cesium lead iodide used for stable inorganic perovskite solar cells. *ACS nano* 12(4), 3477–3486.
- Miller, B., A. Steinhoff, B. Pano, J. Klein, F. Jahnke, A. Holleitner, and U. Wurstbauer

- (2017). Long-lived direct and indirect interlayer excitons in van der waals heterostructures. *Nano letters* 17(9), 5229–5237.
- Molina-Sánchez, A. (2018). Excitonic states in semiconducting two-dimensional perovskites. *ACS Applied Energy Materials* 1(11), 6361–6367.
- Molina-Sanchez, A. and L. Wirtz (2011). Phonons in single-layer and few-layer mos 2 and ws 2. *Physical Review B* 84(15), 155413.
- Nair, R. R., W. Ren, R. Jalil, I. Riaz, V. G. Kravets, L. Britnell, P. Blake, F. Schedin, A. S. Mayorov, S. Yuan, *et al.* (2010). Fluorographene: a two-dimensional counterpart of teflon. *small* 6(24), 2877–2884.
- Neek-Amal, M. and F. Peeters (2011). Lattice thermal properties of graphane: thermal contraction, roughness, and heat capacity. *Physical Review B* 83(23), 235437.
- Nielsen, O. H. and R. M. Martin (1985a, Sep). Quantum-mechanical theory of stress and force. *Phys. Rev. B* 32, 3780–3791.
- Nielsen, O. H. and R. M. Martin (1985b, Sep). Stresses in semiconductors: *Ab initio* calculations on si, ge, and gaas. *Phys. Rev. B* 32, 3792–3805.
- Noh, J. H., S. H. Im, J. H. Heo, T. N. Mandal, and S. I. Seok (2013). Chemical management for colorful, efficient, and stable inorganic–organic hybrid nanostructured solar cells. *Nano letters* 13(4), 1764–1769.
- Novoselov, K. S., A. K. Geim, S. V. Morozov, D. Jiang, Y. Zhang, S. V. Dubonos, I. V. Grigorieva, and A. A. Firsov (2004). Electric field effect in atomically thin carbon films. *science* 306(5696), 666–669.
- O’Brien, M., N. McEvoy, C. Motta, J.-Y. Zheng, N. C. Berner, J. Kotakoski, K. Elibol, T. J. Pennycook, J. C. Meyer, C. Yim, M. Abid, T. Hallam, J. F. Donegan, S. Sanvito, and G. S. Duesberg (2016, apr). Raman characterization of platinum diselenide thin films. *2D Materials* 3(2), 021004.
- Onida, G., L. Reining, and A. Rubio (2002). Electronic excitations: density-functional versus many-body greenâs-function approaches. *Reviews of Modern Physics* 74(2), 601.

- Palummo, M., M. Bernardi, and J. C. Grossman (2015). Exciton radiative lifetimes in two-dimensional transition metal dichalcogenides. *Nano letters* 15(5), 2794–2800.
- Palummo, M., O. Pulci, R. Del Sole, A. Marini, P. Hahn, W. Schmidt, and F. Bechstedt (2004). The bethe–salpeter equation: a first-principles approach for calculating surface optical spectra. *Journal of Physics: Condensed Matter* 16(39), S4313.
- Pant, A., E. Torun, B. Chen, S. Bhat, X. Fan, K. Wu, D. P. Wright, F. M. Peeters, E. Soignard, H. Sahin, *et al.* (2016). Strong dichroic emission in the pseudo one dimensional material zrs 3. *Nanoscale* 8(36), 16259–16265.
- Park, H., H. Chung, and W. Kim (2013). Synthesis of ultrathin wurtzite znse nanosheets. *Materials Letters* 99, 172–175.
- Payne, M. C., M. P. Teter, D. C. Allan, T. A. Arias, and J. D. Joannopoulos (1992, Oct). Iterative minimization techniques for *ab initio* total-energy calculations: molecular dynamics and conjugate gradients. *Rev. Mod. Phys.* 64, 1045–1097.
- Peng, J.-P., J.-Q. Guan, H.-M. Zhang, C.-L. Song, L. Wang, K. He, Q.-K. Xue, and X.-C. Ma (2015, Mar). Molecular beam epitaxy growth and scanning tunneling microscopy study of tise₂ ultrathin films. *Phys. Rev. B* 91, 121113.
- Perdew, J. P., K. Burke, and M. Ernzerhof (1996, Oct). Generalized gradient approximation made simple. *Phys. Rev. Lett.* 77, 3865–3868.
- Plumb, K., J. Clancy, L. Sandilands, V. V. Shankar, Y. Hu, K. Burch, H.-Y. Kee, and Y.-J. Kim (2014). α -rucl 3: A spin-orbit assisted mott insulator on a honeycomb lattice. *Physical Review B* 90(4), 041112.
- Pollini, I. (1994). Photoemission study of the electronic structure of crcl 3 and rucl 3 compounds. *Physical Review B* 50(4), 2095.
- Pollini, I. (1996). Electronic properties of the narrow-band material α -rucl 3. *Physical Review B* 53(19), 12769.
- Pontes, R. B., R. H. Miwa, A. J. da Silva, A. Fazzio, and J. E. Padilha (2018). Layer-dependent band alignment of few layers of blue phosphorus and their van der

- waals heterostructures with graphene. *Physical Review B* 97(23), 235419.
- Protesescu, L., S. Yakunin, M. I. Bodnarchuk, F. Krieg, R. Caputo, C. H. Hendon, R. X. Yang, A. Walsh, and M. V. Kovalenko (2015). Nanocrystals of cesium lead halide perovskites (CsPbX_3 , $X = \text{Cl, Br, I}$): novel optoelectronic materials showing bright emission with wide color gamut. *Nano letters* 15(6), 3692–3696.
- Radisavljevic, B., A. Radenovic, J. Brivio, V. Giacometti, and A. Kis (2011). Single-layer MoS_2 transistors. *Nature nanotechnology* 6(3), 147.
- Raja, S. N., Y. Bekenstein, M. A. Koc, S. Fischer, D. Zhang, L. Lin, R. O. Ritchie, P. Yang, and A. P. Alivisatos (2016). Encapsulation of perovskite nanocrystals into macroscale polymer matrices: enhanced stability and polarization. *ACS applied materials & interfaces* 8(51), 35523–35533.
- Refaely-Abramson, S., D. Y. Qiu, S. G. Louie, and J. B. Neaton (2018). Defect-induced modification of low-lying excitons and valley selectivity in monolayer transition metal dichalcogenides. *Physical review letters* 121(16), 167402.
- Ritschel, T., J. Trinckauf, K. Koepf, B. Büchner, M. v. Zimmermann, H. Berger, Y. Joe, P. Abbamonte, and J. Geck (2015). Orbital textures and charge density waves in transition metal dichalcogenides. *Nature physics* 11(4), 328.
- Rivera, P., J. R. Schaibley, A. M. Jones, J. S. Ross, S. Wu, G. Aivazian, P. Klement, K. Seyler, G. Clark, N. J. Ghimire, *et al.* (2015). Observation of long-lived interlayer excitons in monolayer MoS_2 - WSe_2 heterostructures. *Nature communications* 6, 6242.
- Robinson, J. T., J. S. Burgess, C. E. Junkermeier, S. C. Badescu, T. L. Reinecke, F. K. Perkins, M. K. Zalalutdinov, J. W. Baldwin, J. C. Culbertson, P. E. Sheehan, *et al.* (2010). Properties of fluorinated graphene films. *Nano letters* 10(8), 3001–3005.
- Rodin, A., A. Carvalho, and A. C. Neto (2014). Strain-induced gap modification in black phosphorus. *Physical review letters* 112(17), 176801.
- Rogalski, A. (2005). HgCdTe infrared detector material: history, status and outlook. *Reports on Progress in Physics* 68(10), 2267.

- Rohlfing, M. and S. G. Louie (2000). Electron-hole excitations and optical spectra from first principles. *Physical Review B* 62(8), 4927.
- Roy, K., M. Padmanabhan, S. Goswami, T. P. Sai, G. Ramalingam, S. Raghavan, and A. Ghosh (2013). Graphene–mos 2 hybrid structures for multifunctional photoresponsive memory devices. *Nature nanotechnology* 8(11), 826.
- Şahin, H., S. Cahangirov, M. Topsakal, E. Bekaroglu, E. Akturk, R. T. Senger, and S. Ciraci (2009). Monolayer honeycomb structures of group-iv elements and iii-v binary compounds: First-principles calculations. *Physical Review B* 80(15), 155453.
- Sahin, H. and S. Ciraci (2012). Chlorine adsorption on graphene: Chlorographene. *The Journal of Physical Chemistry C* 116(45), 24075–24083.
- Şahin, H., R. T. Senger, and S. Ciraci (2010). Spintronic properties of zigzag-edged triangular graphene flakes. *Journal of Applied Physics* 108(7), 074301.
- Sahin, H., S. Tongay, S. Horzum, W. Fan, J. Zhou, J. Li, J. Wu, and F. Peeters (2013). Anomalous raman spectra and thickness-dependent electronic properties of wse 2. *Physical Review B* 87(16), 165409.
- Saidaminov, M. I., V. Adinolfi, R. Comin, A. L. Abdelhady, W. Peng, I. Dursun, M. Yuan, S. Hoogland, E. H. Sargent, and O. M. Bakr (2015). Planar-integrated single-crystalline perovskite photodetectors. *Nature communications* 6, 8724.
- Sajjad, M., E. Montes, N. Singh, and U. Schwingenschlögl (2017). Superior gas sensing properties of monolayer ptse2. *Advanced Materials Interfaces* 4(5), 1600911.
- Saliba, M., T. Matsui, K. Domanski, J.-Y. Seo, A. Ummadisingu, S. M. Zakeeruddin, J.-P. Correa-Baena, W. R. Tress, A. Abate, A. Hagfeldt, *et al.* (2016). Incorporation of rubidium cations into perovskite solar cells improves photovoltaic performance. *Science* 354(6309), 206–209.
- Saliba, M., T. Matsui, J.-Y. Seo, K. Domanski, J.-P. Correa-Baena, M. K. Nazeeruddin, S. M. Zakeeruddin, W. Tress, A. Abate, A. Hagfeldt, *et al.* (2016). Cesium-containing triple cation perovskite solar cells: improved stability, reproducibility and high efficiency. *Energy & environmental science* 9(6), 1989–1997.

- Samnakay, R., D. Wickramaratne, T. Pope, R. Lake, T. Salguero, and A. Balandin (2015). Zone-folded phonons and the commensurate–incommensurate charge-density-wave transition in 1 t-tase2 thin films. *Nano letters* 15(5), 2965–2973.
- Sears, J., M. Songvilay, K. Plumb, J. Clancy, Y. Qiu, Y. Zhao, D. Parshall, and Y.-J. Kim (2015). Magnetic order in α -rucl 3: A honeycomb-lattice quantum magnet with strong spin-orbit coupling. *Physical Review B* 91(14), 144420.
- Sell, D. (1972). Resolved free-exciton transitions in the optical-absorption spectrum of gaas. *Physical Review B* 6(10), 3750.
- Shan, W., B. Little, A. Fischer, J. Song, B. Goldenberg, W. Perry, M. Bremser, and R. Davis (1996). Binding energy for the intrinsic excitons in wurtzite gan. *Physical Review B* 54(23), 16369.
- Sichert, J. A., Y. Tong, N. Mutz, M. Vollmer, S. Fischer, K. Z. Milowska, R. García Cortadella, B. Nickel, C. Cardenas-Daw, J. K. Stolarczyk, *et al.* (2015). Quantum size effect in organometal halide perovskite nanoplatelets. *Nano letters* 15(10), 6521–6527.
- Slater, J. C. (1929, Nov). The theory of complex spectra. *Phys. Rev.* 34, 1293–1322.
- Son, J. S., X.-D. Wen, J. Joo, J. Chae, S.-i. Baek, K. Park, J. H. Kim, K. An, J. H. Yu, S. G. Kwon, *et al.* (2009). Large-scale soft colloidal template synthesis of 1.4 nm thick cdse nanosheets. *Angewandte Chemie International Edition* 48(37), 6861–6864.
- Song, J., J. Li, X. Li, L. Xu, Y. Dong, and H. Zeng (2015). Nanocrystals: Quantum dot light-emitting diodes based on inorganic perovskite cesium lead halides (cspb_x3)(adv. mater. 44/2015). *Advanced Materials* 27(44), 7161–7161.
- Song, S., D. H. Keum, S. Cho, D. Perello, Y. Kim, and Y. H. Lee (2015). Room temperature semiconductor–metal transition of mote2 thin films engineered by strain. *Nano letters* 16(1), 188–193.
- Splendiani, A., L. Sun, Y. Zhang, T. Li, J. Kim, C.-Y. Chim, G. Galli, and F. Wang (2010). Emerging photoluminescence in monolayer mos2. *Nano letters* 10(4), 1271–1275.

- Su, G., V. G. Hadjiev, P. E. Loya, J. Zhang, S. Lei, S. Maharjan, P. Dong, P. M. Ajayan, J. Lou, and H. Peng (2014). Chemical vapor deposition of thin crystals of layered semiconductor SnS_2 for fast photodetection application. *Nano letters* 15(1), 506–513.
- Sugawara, K., Y. Nakata, R. Shimizu, P. Han, T. Hitosugi, T. Sato, and T. Takahashi (2015). Unconventional charge-density-wave transition in monolayer $1\text{T}'\text{-SnS}_2$. *ACS nano* 10(1), 1341–1345.
- Sun, Y., Z. Sun, S. Gao, H. Cheng, Q. Liu, J. Piao, T. Yao, C. Wu, S. Hu, S. Wei, *et al.* (2012). Fabrication of flexible and freestanding zinc chalcogenide single layers. *Nature communications* 3, 1057.
- Sutton, R. J., G. E. Eperon, L. Miranda, E. S. Parrott, B. A. Kamino, J. B. Patel, M. T. Hörantner, M. B. Johnston, A. A. Haghighirad, D. T. Moore, *et al.* (2016). Bandgap-tunable cesium lead halide perovskites with high thermal stability for efficient solar cells. *Advanced Energy Materials* 6(8), 1502458.
- Sutton, R. J., M. R. Filip, A. A. Haghighirad, N. Sakai, B. Wenger, F. Giustino, and H. J. Snaith (2018). Cubic or orthorhombic? revealing the crystal structure of metastable black-phase CsPbI_3 by theory and experiment. *ACS Energy Letters* 3(8), 1787–1794.
- Swarnkar, A., R. Chulliyil, V. K. Ravi, M. Irfanullah, A. Chowdhury, and A. Nag (2015). Colloidal CsPbBr_3 perovskite nanocrystals: luminescence beyond traditional quantum dots. *Angewandte Chemie International Edition* 54(51), 15424–15428.
- Szeles, C. (2004). CdZnTe and CdTe materials for x-ray and gamma ray radiation detector applications. *physica status solidi (b)* 241(3), 783–790.
- Tan, C. and H. Zhang (2015). Wet-chemical synthesis and applications of non-layer structured two-dimensional nanomaterials. *Nature communications* 6, 7873.
- Tan, Z.-K., R. S. Moghaddam, M. L. Lai, P. Docampo, R. Higler, F. Deschler, M. Price, A. Sadhanala, L. M. Pazos, D. Credgington, *et al.* (2014). Bright light-emitting diodes based on organometal halide perovskite. *Nature nanotechnology* 9(9), 687.
- Tao, P., H. Guo, T. Yang, and Z. Zhang (2014). Strain-induced magnetism in MoS_2 monolayer with defects. *Journal of Applied Physics* 115(5), 054305.

- Togo, A. and I. Tanaka (2015, Nov). First principles phonon calculations in materials science. *Scr. Mater.* 108, 1–5.
- Tonndorf, P., R. Schmidt, P. Böttger, X. Zhang, J. Börner, A. Liebig, M. Albrecht, C. Kloc, O. Gordan, D. R. Zahn, *et al.* (2013). Photoluminescence emission and raman response of monolayer mos₂, mose₂, and wse₂. *Optics express* 21(4), 4908–4916.
- Torun, E., H. P. Miranda, A. Molina-Sánchez, and L. Wirtz (2018). Interlayer and intralayer excitons in mos₂/ws₂ and mose₂/wse₂ heterobilayers. *Physical Review B* 97(24), 245427.
- Tran, K., G. Moody, F. Wu, X. Lu, J. Choi, K. Kim, A. Rai, D. A. Sanchez, J. Quan, A. Singh, *et al.* (2019). Evidence for moiré excitons in van der waals heterostructures. *Nature*, 1.
- Tu, C.-C. and L. Y. Lin (2008). High efficiency photodetectors fabricated by electrostatic layer-by-layer self-assembly of cdte quantum dots. *Applied Physics Letters* 93(16), 163107.
- Ugeda, M. M., A. J. Bradley, S.-F. Shi, H. Felipe, Y. Zhang, D. Y. Qiu, W. Ruan, S.-K. Mo, Z. Hussain, Z.-X. Shen, *et al.* (2014). Giant bandgap renormalization and excitonic effects in a monolayer transition metal dichalcogenide semiconductor. *Nature materials* 13(12), 1091.
- Ugeda, M. M., I. Brihuega, F. Guinea, and J. M. Gómez-Rodríguez (2010). Missing atom as a source of carbon magnetism. *Physical Review Letters* 104(9), 096804.
- Ullah, K., S. Ye, S.-B. Jo, L. Zhu, K.-Y. Cho, and W.-C. Oh (2014). Optical and photocatalytic properties of novel heterogeneous ptse₂–graphene/tio₂ nanocomposites synthesized via ultrasonic assisted techniques. *Ultrasonics sonochemistry* 21(5), 1849–1857.
- Van Setten, M., M. Giantomassi, E. Bousquet, M. J. Verstraete, D. R. Hamann, X. Gonze, and G.-M. Rignanese (2018). The pseudodojo: Training and grading a 85 element optimized norm-conserving pseudopotential table. *Computer Physics Communications* 226, 39–54.

- Villegas, C. E., A. Rodin, A. Carvalho, and A. Rocha (2016). Two-dimensional exciton properties in monolayer semiconducting phosphorus allotropes. *Physical Chemistry Chemical Physics* 18(40), 27829–27836.
- Vinogradov, N. A., K. Schulte, M. L. Ng, A. Mikkelsen, E. Lundgren, N. Martensson, and A. Preobrajenski (2011). Impact of atomic oxygen on the structure of graphene formed on ir (111) and pt (111). *The Journal of Physical Chemistry C* 115(19), 9568–9577.
- Vogt, P., P. De Padova, C. Quaresima, J. Avila, E. Frantzeskakis, M. C. Asensio, A. Resta, B. Ealet, and G. Le Lay (2012). Silicene: compelling experimental evidence for graphenelike two-dimensional silicon. *Physical review letters* 108(15), 155501.
- Wang, G., R. Pandey, and S. P. Karna (2015). Phosphorene oxide: stability and electronic properties of a novel two-dimensional material. *Nanoscale* 7(2), 524–531.
- Wang, J., J. Meng, Q. Li, and J. Yang (2016). Single-layer cadmium chalcogenides: promising visible-light driven photocatalysts for water splitting. *Physical Chemistry Chemical Physics* 18(25), 17029–17036.
- Wang, J., N. Wang, Y. Jin, J. Si, Z.-K. Tan, H. Du, L. Cheng, X. Dai, S. Bai, H. He, *et al.* (2015). Interfacial control toward efficient and low-voltage perovskite light-emitting diodes. *Advanced Materials* 27(14), 2311–2316.
- Wang, K.-H., L. Wu, L. Li, H.-B. Yao, H.-S. Qian, and S.-H. Yu (2016). Large-scale synthesis of highly luminescent perovskite-related CsPb_2Br_5 nanoplatelets and their fast anion exchange. *Angewandte Chemie International Edition* 55(29), 8328–8332.
- Wang, Q., M. Lyu, M. Zhang, J.-H. Yun, H. Chen, and L. Wang (2015). Transition from the tetragonal to cubic phase of organohalide perovskite: The role of chlorine in crystal formation of $\text{CH}_3\text{NH}_3\text{PbI}_3$ on TiO_2 substrates. *The journal of physical chemistry letters* 6(21), 4379–4384.
- Wang, Y., L. Li, W. Yao, S. Song, J. Sun, J. Pan, X. Ren, C. Li, E. Okunishi, Y.-Q. Wang, *et al.* (2015). Monolayer PtSe_2 , a new semiconducting transition-metal-dichalcogenide, epitaxially grown by direct selenization of pt. *Nano letters* 15(6), 4013–4018.
- Wang, Y., X. Li, J. Song, L. Xiao, H. Zeng, and H. Sun (2015). All-inorganic colloidal

- perovskite quantum dots: a new class of lasing materials with favorable characteristics. *Advanced materials* 27(44), 7101–7108.
- Wang, Z., Q. Ou, Y. Zhang, Q. Zhang, H. Y. Hoh, and Q. Bao (2018). Degradation of two-dimensional $\text{CH}_3\text{NH}_3\text{PbI}_3$ perovskite and $\text{CH}_3\text{NH}_3\text{PbI}_3/\text{graphene}$ heterostructure. *ACS applied materials & interfaces* 10(28), 24258–24265.
- Wassmann, T., A. P. Seitsonen, A. M. Saitta, M. Lazzeri, and F. Mauri (2008). Structure, stability, edge states, and aromaticity of graphene ribbons. *Physical review letters* 101(9), 096402.
- Weber, D., L. M. Schoop, V. Duppel, J. M. Lippmann, J. Nuss, and B. V. Lotsch (2016). Magnetic properties of restacked 2d spin 1/2 honeycomb RuCl_3 nanosheets. *Nano letters* 16(6), 3578–3584.
- Wei, Q. and X. Peng (2014). Superior mechanical flexibility of phosphorene and few-layer black phosphorus. *Applied Physics Letters* 104(25), 251915.
- Wong, J.-H., B.-R. Wu, and M.-F. Lin (2012). Strain effect on the electronic properties of single layer and bilayer graphene. *The Journal of Physical Chemistry C* 116(14), 8271–8277.
- Woomer, A. H., T. W. Farnsworth, J. Hu, R. A. Wells, C. L. Donley, and S. C. Warren (2015). Phosphorene: synthesis, scale-up, and quantitative optical spectroscopy. *ACS nano* 9(9), 8869–8884.
- Wu, F., T. Lovorn, and A. H. MacDonald (2017). Topological exciton bands in moiré heterojunctions. *Physical review letters* 118(14), 147401.
- Xi, X., L. Zhao, Z. Wang, H. Berger, L. Forró, J. Shan, and K. F. Mak (2015). Strongly enhanced charge-density-wave order in monolayer NbSe_2 . *Nature nanotechnology* 10(9), 765.
- Xing, J., F. Yan, Y. Zhao, S. Chen, H. Yu, Q. Zhang, R. Zeng, H. V. Demir, X. Sun, A. Huan, et al. (2016). High-efficiency light-emitting diodes of organometal halide perovskite amorphous nanoparticles. *ACS nano* 10(7), 6623–6630.

- Yagmurcukardes, M., F. M. Peeters, R. T. Senger, and H. Sahin (2016). Nanoribbons: From fundamentals to state-of-the-art applications. *Applied Physics Reviews* 3(4), 041302.
- Yamamoto, M., T. L. Einstein, M. S. Fuhrer, and W. G. Cullen (2013). Anisotropic etching of atomically thin mos₂. *The Journal of Physical Chemistry C* 117(48), 25643–25649.
- Yang, S., C. Wang, H. Sahin, H. Chen, Y. Li, S.-S. Li, A. Suslu, F. M. Peeters, Q. Liu, J. Li, *et al.* (2015). Tuning the optical, magnetic, and electrical properties of reSe₂ by nanoscale strain engineering. *Nano letters* 15(3), 1660–1666.
- Yang, W. S., J. H. Noh, N. J. Jeon, Y. C. Kim, S. Ryu, J. Seo, and S. I. Seok (2015). High-performance photovoltaic perovskite layers fabricated through intramolecular exchange. *Science* 348(6240), 1234–1237.
- Yao, W., E. Wang, H. Huang, K. Deng, M. Yan, K. Zhang, K. Miyamoto, T. Okuda, L. Li, Y. Wang, *et al.* (2017). Direct observation of spin-layer locking by local Rashba effect in monolayer semiconducting PtSe₂ film. *Nature communications* 8, 14216.
- Yazyev, O. V. and L. Helm (2007). Defect-induced magnetism in graphene. *Physical Review B* 75(12), 125408.
- Ye, S. and W.-C. Oh (2016). Demonstration of enhanced photocatalytic effect with PtSe₂ and TiO₂ treated large area graphene obtained by CVD method. *Materials Science in Semiconductor Processing* 48, 106–114.
- Ye, Z., T. Cao, K. O'Brien, H. Zhu, X. Yin, Y. Wang, S. G. Louie, and X. Zhang (2014). Probing excitonic dark states in single-layer tungsten disulfide. *Nature* 513(7517), 214.
- Yeo, J. S., J. J. Vittal, W. Henderson, and T. A. Hor (2002). Exploring the Lewis basicity of the metalloligand [Pt(μ-Se)₂(PPh₃)₄] on metal substrates by electrospray mass spectrometry. synthesis, characterization and structural studies of new platinum selenido phosphine complexes containing the {Pt₂Se₂} core. *Journal of the Chemical Society, Dalton Transactions* (3), 328–336.
- Yettapu, G. R., D. Talukdar, S. Sarkar, A. Swarnkar, A. Nag, P. Ghosh, and P. Mandal (2016). Terahertz conductivity within colloidal CsPbBr₃ perovskite nanocrystals: remarkably high carrier mobilities and large diffusion lengths. *Nano letters* 16(8), 4838–4848.

- Yu, H., G.-B. Liu, J. Tang, X. Xu, and W. Yao (2017). Moiré excitons: From programmable quantum emitter arrays to spin-orbit-coupled artificial lattices. *Science advances* 3(11), e1701696.
- Yu, L., Q. Yan, and A. Ruzsinszky (2017). Negative poisson's ratio in 1t-type crystalline two-dimensional transition metal dichalcogenides. *Nature communications* 8, 15224.
- Yu, Y., S. Hu, L. Su, L. Huang, Y. Liu, Z. Jin, A. A. Purezky, D. B. Geohegan, K. W. Kim, Y. Zhang, *et al.* (2014). Equally efficient interlayer exciton relaxation and improved absorption in epitaxial and nonepitaxial mos₂/ws₂ heterostructures. *Nano letters* 15(1), 486–491.
- Zeng, J., P. Cui, and Z. Zhang (2017). Half layer by half layer growth of a blue phosphorene monolayer on a gan (001) substrate. *Physical review letters* 118(4), 046101.
- Zeng, L.-H., S.-H. Lin, Z.-J. Li, Z.-X. Zhang, T.-F. Zhang, C. Xie, C.-H. Mak, Y. Chai, S. P. Lau, L.-B. Luo, *et al.* (2018). Fast, self-driven, air-stable, and broadband photodetector based on vertically aligned ptse₂/gaas heterojunction. *Advanced Functional Materials* 28(16), 1705970.
- Zhang, G., A. Chaves, S. Huang, F. Wang, Q. Xing, T. Low, and H. Yan (2018). Determination of layer-dependent exciton binding energies in few-layer black phosphorus. *Science advances* 4(3), eaap9977.
- Zhang, J., J. M. Soon, K. P. Loh, J. Yin, J. Ding, M. B. Sullivan, and P. Wu (2007). Magnetic molybdenum disulfide nanosheet films. *Nano letters* 7(8), 2370–2376.
- Zhang, J. L., S. Zhao, C. Han, Z. Wang, S. Zhong, S. Sun, R. Guo, X. Zhou, C. D. Gu, K. D. Yuan, *et al.* (2016). Epitaxial growth of single layer blue phosphorus: a new phase of two-dimensional phosphorus. *Nano letters* 16(8), 4903–4908.
- Zhang, S., Z. Yan, Y. Li, Z. Chen, and H. Zeng (2015). Atomically thin arsenene and antimonene: semimetal–semiconductor and indirect–direct band-gap transitions. *Angewandte Chemie International Edition* 54(10), 3112–3115.
- Zhang, W., H. Enriquez, Y. Tong, A. Bendounan, A. Kara, A. P. Seitsonen, A. J. Mayne, G. Dujardin, and H. Oughaddou (2018). Epitaxial synthesis of blue phosphorene.

Small 14(51), 1804066.

Zhang, W., L. Peng, J. Liu, A. Tang, J.-S. Hu, J. Yao, and Y. S. Zhao (2016). Controlling the cavity structures of two-photon-pumped perovskite microlasers. *Advanced Materials* 28(21), 4040–4046.

Zhang, X., X. Ren, B. Liu, R. Munir, X. Zhu, D. Yang, J. Li, Y. Liu, D.-M. Smilgies, R. Li, *et al.* (2017). Stable high efficiency two-dimensional perovskite solar cells via cesium doping. *Energy & Environmental Science* 10(10), 2095–2102.

Zhang, X., B. Xu, J. Zhang, Y. Gao, Y. Zheng, K. Wang, and X. W. Sun (2016). All-inorganic perovskite nanocrystals for high-efficiency light emitting diodes: Dual-phase cspbbr₃-cspb₂br₅ composites. *Advanced Functional Materials* 26(25), 4595–4600.

Zhang, Y., Y.-W. Tan, H. L. Stormer, and P. Kim (2005). Experimental observation of the quantum hall effect and berry's phase in graphene. *nature* 438(7065), 201.

Zhang, Z., X. Zou, V. H. Crespi, and B. I. Yakobson (2013). Intrinsic magnetism of grain boundaries in two-dimensional metal dichalcogenides. *ACS nano* 7(12), 10475–10481.

Zhang, Z.-X., L.-H. Zeng, X.-W. Tong, Y. Gao, C. Xie, Y. H. Tsang, L.-B. Luo, and Y.-C. Wu (2018). Ultrafast, self-driven, and air-stable photodetectors based on multilayer ptse₂/perovskite heterojunctions. *The journal of physical chemistry letters* 9(6), 1185–1194.

Zhao, Y., J. Qiao, P. Yu, Z. Hu, Z. Lin, S. P. Lau, Z. Liu, W. Ji, and Y. Chai (2016). Extraordinarily strong interlayer interaction in 2d layered pts₂. *Advanced Materials* 28(12), 2399–2407.

Zhao, Y., J. Qiao, Z. Yu, P. Yu, K. Xu, S. P. Lau, W. Zhou, Z. Liu, X. Wang, W. Ji, *et al.* (2017). High-electron-mobility and air-stable 2d layered ptse₂ fets. *Advanced Materials* 29(5), 1604230.

Zheng, H., X.-B. Li, N.-K. Chen, S.-Y. Xie, W. Q. Tian, Y. Chen, H. Xia, S. Zhang, and H.-B. Sun (2015). Monolayer ii-vi semiconductors: A first-principles prediction. *Physical Review B* 92(11), 115307.

- Zheng, H., B. Yang, D. Wang, R. Han, X. Du, and Y. Yan (2014). Tuning magnetism of monolayer mos₂ by doping vacancy and applying strain. *Applied Physics Letters* 104(13), 132403.
- Zhou, W., M. D. Kapetanakis, M. P. Prange, S. T. Pantelides, S. J. Pennycook, and J.-C. Idrobo (2012). Direct determination of the chemical bonding of individual impurities in graphene. *Physical review letters* 109(20), 206803.
- Zhou, W., X. Zou, S. Najmaei, Z. Liu, Y. Shi, J. Kong, J. Lou, P. M. Ajayan, B. I. Yakobson, and J.-C. Idrobo (2013). Intrinsic structural defects in monolayer molybdenum disulfide. *Nano letters* 13(6), 2615–2622.
- Zhou, Y., Z. Wang, P. Yang, X. Zu, L. Yang, X. Sun, and F. Gao (2012). Tensile strain switched ferromagnetism in layered nbs₂ and nbse₂. *Acs Nano* 6(11), 9727–9736.
- Zhu, H., Y. Fu, F. Meng, X. Wu, Z. Gong, Q. Ding, M. V. Gustafsson, M. T. Trinh, S. Jin, and X. Zhu (2015). Lead halide perovskite nanowire lasers with low lasing thresholds and high quality factors. *Nature materials* 14(6), 636.
- Zhu, J., J. Wu, Y. Sun, J. Huang, Y. Xia, H. Wang, H. Wang, Y. Wang, Q. Yi, and G. Zou (2016). Thickness-dependent bandgap tunable molybdenum disulfide films for optoelectronics. *RSC Advances* 6(112), 110604–110609.
- Zhu, Z. and D. Tománek (2014). Semiconducting layered blue phosphorus: a computational study. *Physical review letters* 112(17), 176802.
- Zitter, R. (1971). Raman detection of tellurium layers on surfaces of cdte. *Surface Science* 28, 335–338.

VITA

Date and Place of Birth: 11.08.1987, İzmir-TURKEY

EDUCATION

2013 - 2019 Doctor of Philosophy in Department of Physics

Graduate School of Engineering and Sciences, İzmir Institute of Technology,
İzmir -Turkey

Thesis Title: Optical and Electronic Properties of Atomically Thin Layered Materials:
First Principles Calculations

Supervisor: Prof. Dr. R. Tuğrul SENGER

2010 - 2013 Master of Science in Physics

Graduate School of Engineering and Sciences, İzmir Institute of Technology
İzmir -Turkey

Thesis Title: Calculations of Electric and Magnetic Properties of Triangular Graphene
Fragments Using Density Functional Theory: Effects of Edge Functionalization and
Electric Field

Supervisor: Prof. Dr. R. Tuğrul SENGER

2005 - 2010 Bachelor of Physics

Department of Physics, Faculty of Science, Dokuz Eylül University
İzmir - Turkey

SELECTED PUBLICATIONS

Iyikanat, F., Sahin, H., Senger, R. T., and Peeters, F. M. (2015).

“Vacancy Formation and Oxidation Characteristics of Single Layer TiS_3 ”.
J. Phys. Chem. C, 119, 10709.

Iyikanat, F., Sari, E., and Sahin, H. (2017).

“Thinning CsPb_2Br_5 perovskite down to monolayers: Cs-dependent stability”.
Phys. Rev. B, 96, 155442.

Iyikanat, F., Yagmurcukardes, M., Senger, R. T., and Sahin, H. (2018).

“Tuning electronic and magnetic properties of monolayer $\alpha\text{-RuCl}_3$ by in-plane strain”.
J. Mater. Chem. C, 6, 2019.